Erkka J. Kannisto

Fabrication and characterization of $Al_2O_3 - Ni$ nanocomposites
Master of Science thesis

$Al_2O_3 - Ni$ nanokomposiittien valmistus ja karakterisointi
Diplomityö

Abstract

This master's thesis is divided into two sections: A literature survey and an experimental part. The literature survey broadly reviews ceramic nanocomposites and gives the reader a basic understanding concerning their mechanical properties and the state-of-the-art research made in this area. The survey also reviews colloidal processing and manufacturing technology of ceramic nanomaterials. Based on the survey the reader will be able to analyse the results presented in the experimental part of this study, although it requires also basic understanding about materials science and ceramic materials.

In the experimental part, $Al_2O_3 - Ni$ nanocomposite powder was synthesized using thermolysis and green compacts were slip casted from the powders. Sintering of the green compacts was done using pulsed electric current sintering (PECS) method, which helps to retain the nanostructure better than normal sintering. The nanocomposites were compared with pure alumina reference samples that were produced with the same methods. Compared to reference, nanocomposite hardness rose by 2 % and fracture toughness by 13 %. According to results and literature the hardening effect was found to relate to nickel nanoparticles under a critical size (<60 nm). Toughening was analysed to be a cause of large difference in thermal expansion between the matrix and second phase particles, which induce a residual stress state in the material after sintering. Additionally novel geometrical model was introduced which can be used to predict nanoparticle coarsening during sintering. New properties can arise from the size effect alone and therefore controlling the size during sintering becomes a necessity.

Work was financed by TEKES and coordinated by Finnish Metals and Engineering Competence Cluster Ltd. as a part of the Demanding Applications (DEMAPP) research program. Work was done in close collaboration with Aalto University's Materials and engineering department and Metso Paper Ltd.

Tiivistelmä (Abstract in finnish)

Tampereen Teknillinen Yliopisto (TTY)
Materiaalitekniikan diplomi-insinöörin tutkinto
KANNISTO, ERKKA: $Al_2O_3 - Ni$ nanokomposiittien valmistus ja karakterisointi
Diplomityö, 64 sivua, 16 liitesivua
Työ valmistunut 12/2012
Pääaine: Keraamimateriaalit ja pinnoitustekniikka
Työn tarkastaja: Professori Erkki Levänen (TkT)
Avainsanat: Al_2O_3, Alumiinioksidi, Ni, Nikkeli, Termolyysi, Aineen hajottaminen lämmön avulla, Keraami, Nanokomposiitti, Lietevalu, Kolloidinen prosessointi, Nanopartikkeli, Partikkelikoko, Kovuus, Murtositkeys, Sintraus, Sähköpulssisintraus, PECS, Kipinäplasmasintraus, SPS, Mallintaminen

Tämä diplomityö jakautuu kahteen osaan: Kirjallisuusosioon ja kokeelliseen osuuteen. Työn kirjallisuusosuus käsittelee keraamisia nanokomposiitteja laajasti ja antaa lukijalle peruskäsityksen niiden mekaanisista ominaisuuksista ja tutkimuksen nykytasosta. Lisäksi kirjallisuusosuus käsittelee laajasti keraamijauheiden kolloidista prosessointia ja valmistustekniikkaa nanomateriaalien näkökulmasta. Kirjallisuusosan avulla lukija kykenee ymmärtämään kokeellisen osan tulokset, joskin tulkitseminen vaatii myös materiaalitekniikan ja keraamimateriaalien pohjatietämystä.

Kokeellisessa osuudessa syntetisoitiin $Al_2O_3 - Ni$ nanokomposiittijauhetta termolyysin avulla ja jauheesta valmistettiin lietevalamalla vihreän tilan kappaleita. Vihreän tilan kappaleiden sintraus tehtiin käyttämällä kipinäplasmasintrausmenetelmää (PECS), joka auttaa säilyttämään nanorakenteen paremmin kuin normaali sintraus. Vertaamalla nanokomposiittia puhtaaseen Al_2O_3 referenssiin, joka valmistettiin samoilla menetelmillä, nousi kovuus 2 % ja murtositkeys 13 %. Tulosten ja kirjallisuuden perusteella kovuuden kasvun todettiin olevan yhteydessä nikkelipartikkeleihin, jotka ovat alle kriittisen raekoon (<60 nm). Murtositkeyden analysoitiin johtuvan materiaalien suuresta lämpölaajenemiserosta, joka aiheuttaa jäännösjännitystilan kappaleeseen sintrauksen jälkeen. Lisäksi työssä esitellään uutta geometrista mallia, jonka avulla voidaan ennustaa nanopartikkelien rakeen kasvua sintrauksessa. Joidenkin materiaaliominaisuuksien on havaittu olevan suoraan yhteydessä partikkelien raekokoon, joten rakeenkasvun hallitseminen on tärkeää koko prosessoin ajan.

Työn on rahoittanut teknologian kehittämiseskeskus (TEKES) ja koordinoinut FIMECC Oy, joka on Suomen metalli- ja koneteollisuuden strateginen huippuosaamisen keskittymä. Työ on osa Demanding Applications (DEMAPP) tutkimusohjelmaa. Tutkimuksessa on tehty läheistä yhteistyötä Aalto Yliopiston materiaalitekniikan laitoksen ja Metso Paper Oy:n kanssa.

Forewords

It is in great awe that I watch the progress of materials science and I, as a materials scientist, have been granted the best seats in the house. Still it is no wonder that material discipline has been set as one of the most important research areas of early 20th century. Many questions still need answering, energy deficiency of oil consuming countries to be named only as the tip of the ice berg.

Ceramic materials are one of the major materials group inside materials science discipline. In this category we have the strongest, most heat resistant, most inert, most lustrous, most expensive and most difficult materials to produce, characterized by their ionic and/or covalent bonding. Yet their characteristics also include brittle fracture on impact and limited bending strength. Improving the fracture toughness of ceramic materials has been a goal from the very beginning of ceramic materials research. Possibilities are limitless for materials that are stronger, lighter and can resist catastrophic deformation like metals. At the moment the research focus in technical ceramics is in reduction of grain size to nanoscale which has led to new discovery in materials we once thought familiar. It is very hard and expensive to produce and study nanomaterial in large scale; therefore future studies will concentrate on solving problems and limitations concerning manufacturing and characterization. We also need to find real applications for nanomaterials to increase the effort of bringing production costs down.

At the moment the great turning point might be at hand when we are stepping away from only improving fracture toughness of ceramics and moving towards creating ceramics that can deform semiplastically or even plastically. It is all a cause of active nanomaterials research which has revealed totally new mechanical phenomena in polycrystal ceramic materials.

Tampere, Finland, 31.10.2012

Erkka J. Kannisto

Table of contents

Symbols and abbreviations

SI-units

Pa   Pascal
m   Meter
K   Kelvin

Abbreviations

Al_2O_3 Aluminium oxide, alumina
ZrO_2 Zirconium oxide, zirconia
SiC Silicon carbide
BN Boron nitride
$c-BN$ Cubic boron nitride
TiN Titanium nitride
WC Tungsten carbide

BET   Theory by Brunauer, Emmett and Teller
DLVO   Theory by Derjaguin and Landau, Verwey and Overbeek
FPZ   Frontal process zone
Internagranular
fracture   Fracture propagating through the grain boundaries
PECS   Pulsed electric current sintering (synonym for SPS)
PN   Peierls-Nabarro
SSA   Specific surface area
SEM   Scanning electron microscope
SPS   Spark plasma sintering
Transgranular
fracture   Fracture propagating through the grains
TEM   Transmission electron microscope

Greek symbols

α Coefficient of thermal expansion
α_m Specific hydraulic resistance of the mould
α_c Specific hydraulic resistance of the cast layer
β_{gr} Growth rate of cast layer
γ Critical exponent
ε_c Volume fraction of pores in the cast layer
ε_m Volume fraction of pores in the mold
μ Coefficient of friction
ρ_{cl} Density of the cast layer (ratio between pores and solids)
σ Stress
σ_f Flexural strength, bending strength
σ_Y Yield stress (Hall-Petch)
σ_{Y0} Normal yield stress
τ Shear stress
φ $1 - f/f_c$
ϕ Constant (Equation 14 - Fracture toughness)
λ Thermal conductivity

η	Viscosity of the slip
υ	Poisson's ratio

Alphabetic

a	Diagonal half-length of an indentation
c	Flaw size or median crack length
c_s	Volume fraction of solids in the slip
d	Grain diameter or mean of two diagonal lengths of an indentation
D	Thickness of the layer coating a single nanoparticle
E	Elastic modulus
f	Concentration
f_c	Percolation threshold
G	Shear modulus
h	Hall-Petch dependence
H	Hardness
H_v	Hardness in Vickers scale
H_{cer}	Original hardness of the ceramic matrix
H_{met}	Hardness of the bulk metal
H_{met0}	Hardness of single phase composed by nanoparticle and matrix coating
k	Material constant (Hall-Petch)
K_{IC}	Fracture toughness
M	Metal ion or salt forming cation ($Ni^{+2}, Fe^{+2} etc.$)
n	Mass balance factor equal to $(1 - c_s - \varepsilon_c)/c_s$
N, F_n, P_n	Normal load
r_0	Radius of a single nanoparticle
r_p	radius of a nanoparticle created by thermal decomposition process
r_m	radius of a matrix particle in the thermal decomposition process
R_s	Thermal shock resistance
s	Salt forming anion ($CH_3COO^-, Cl^-, NO_3^- etc.$)
S	Specific surface area of a powder
v	Velocity
V_{total}	Sum of potential energies between particles in a colloid
V_{vdW}	van der Waals potential energy
V_{elect}	Electrostatic repulsive potential energy
V_{steric}	Repulsive potential energy resulting from of adsorbed polymeric species
$V_{structural}$	Potential energy of nonadsorbed species
x	Multiplier
Y	Stress intensity factor

1. Introduction

Manufacturing ceramic nanocomposites has been under development since early 1990's when the concept was originally introduced [1]. This study was conducted to continue the literature survey made by author in 4/2011 on enhanced mechanical and wear properties of Al_2O_3 nanocomposites (see ref. [2]). In this thesis we concentrate on fabricating Al_2O_3 nanocomposites by investigating the process of dispersing second phase Ni particles into the Al_2O_3 matrix. Nanocomposite powder synthesis by thermolysis was experimented and slip casting method was selected to form green bodies. As a production method slip casting is close to other conventional forming methods and therefore gives valuable general information on fabrication of nanocomposite solids.

Nanocomposite design in conventional structural ceramics has been reported to give exceptional rise in wear resistance [3, 4] by introducing radical changes in wear mechanism [5]. Studies also indicate small or moderate increase in fracture toughness [3, 4, 5, 6] and hardness [3, 4] and additionally significant matrix grain refinement during sintering caused by second phase particles located in grain boundaries [3, 4, 5, 6]. To obtain useful mechanical properties, maximum sintered density and full dispersion of the second phase particles must be achieved. It requires careful controlling of the wet colloidal process where powders are mixed in liquid medium and dispersed using traditional milling process, ultrasonic agitation or high shear mixers. Ceramic powders have a tendency to agglomerate after mixing due to weak electrical dipole forces. These forces must be overcome by steric or electrosteric stabilization methods, which are optimized for the given starting materials.

Although under extensive research, the underlying principles which determine the mechanical properties of ceramic nanostructured composites are still under debate. In 1997 Martin Sternitzke [7] wrote in his broad review on structural ceramic nanocomposites: "It is still unclear, however, whether those improvements (mechanical) can directly be related to an intrinsic 'nanocomposite effect' or to other factors." Ten years later the same questions were still present. In 2007 José Moya et al. [8] wrote in their review on ceramic micro- and nanocomposites: "However, the dependence of the microstructure and therefore, the properties of cermets on metal concentration, are not well understood yet."

The first aim of this study is not to suggest a conclusion for this underlying problem but to merely point out that the same questions still linger due to difficult characterization of nanomaterials. Reviews that I quoted are as good information sources as they were during their release and should be noted as so. The new information available today offers a little relief for the researcher on what to pursue within this field. With limited research facilities these questions are out of my reach and this thesis attempts to summarize the state-of-the-art of basic research made in this area.

The second aim is to demonstrate fabrication and processing of nanocomposites. During this thesis, propositions for processing improvements were constantly looked upon. A route to synthesize and manufacture ceramic nanocomposites by thermolysis is presented with a critical overview on the challenges that manufacturing exhibits.

The mechanical tests in this study concentrated on hardness and fracture toughness properties of $Al_2O_3 - Ni$ nanocomposites. There are both ceramic and metallic second phase components that have been reported to enhance mechanical properties of Al_2O_3. Nickel (Ni) was chosen as the second phase material to test and confirm these reported improvements and to demonstrate manufacturing process of ceramic nanocomposites. Slip casted samples were sintered to near full densities (>99.5% T.D.) using pulsed electric current sintering (PECS) method.

2. Ceramic nanocomposites: Introduction

Because the present ceramic processing routes offer only limited ability to control the dispersion of nanoparticles inside a matrix, an optimal bulk nanocomposite system is hard to produce and subsequently test. This relates to the underlying inability to process nanoparticles so, that the nanoscale microstructure in bulk material is fully maintained. At the moment the best route to understand nanocomposite properties is to study the interfacial properties of small scale bulk systems, such as thin films, and then adapt and scale up to bulk nanocomposites.

Some intrinsic properties (e.g. hardness) of the nanoparticles seem to be related to certain size range [9]. It is very difficult to obtain dense material where there is only this narrow size distribution present. Therefore analysing the cause of enhancement is at the moment more of a statistical problem than a definite problem. This is at least very familiar concept in mechanical properties of ceramic materials.

In this chapter we attempt to classify ceramic nanocomposites in comprehensive way and search through the state-of-the-art research studies to find out the principles which determine the mechanical properties of ceramic nanocomposites.

2.1   Classification of ceramic nanocomposites

A ceramic nanocomposite can be defined as a material with microstructured or nanostructured ceramic matrix with second phase nanoparticle inclusions embedded into the matrix. Nanoparticle itself is defined as having at least one dimension in size range of 1-100 nm. On the structural point of view the nanocomposite often refers to a material consisting of three parameters:

1) Engineering ceramic matrix
   - Aluminium oxide, Zirconium oxide, Silicon carbide, Silicon nitride etc.

2) Metal/ceramic particle dispersion
   - Silicon carbide, Zirconium oxide, Nickel, Iron, Silver etc.
   - Round or irregular shape
   - Other shapes also possible such as whiskers, nanotubes, nanoflakes etc.

3) Particle size of the second phase dispersion is in range of 100 nm

The most important factor in determining the effect of second phase nanostructure to a material is based on the foundation of particle dispersion. To be able to predict and measure what changes a nanodipersion will induce, we have to be certain of homogenous dispersion and that no agglomerates survive the processing phase. It is a basic principle in ceramic processing that the dispersive state of a green compact is the final one and no further modifications prior to sintering can be made. Niihara's classification of nanocomposites [1] (figure 2.1a) is logical and still valid although introduced already in the early 1990's. On a mindset basis it is necessary to consider also different forms of nanoparticles such as fibres, platelets, nanotubes etc. but they do not change the basic principles regarding the dispersion type.
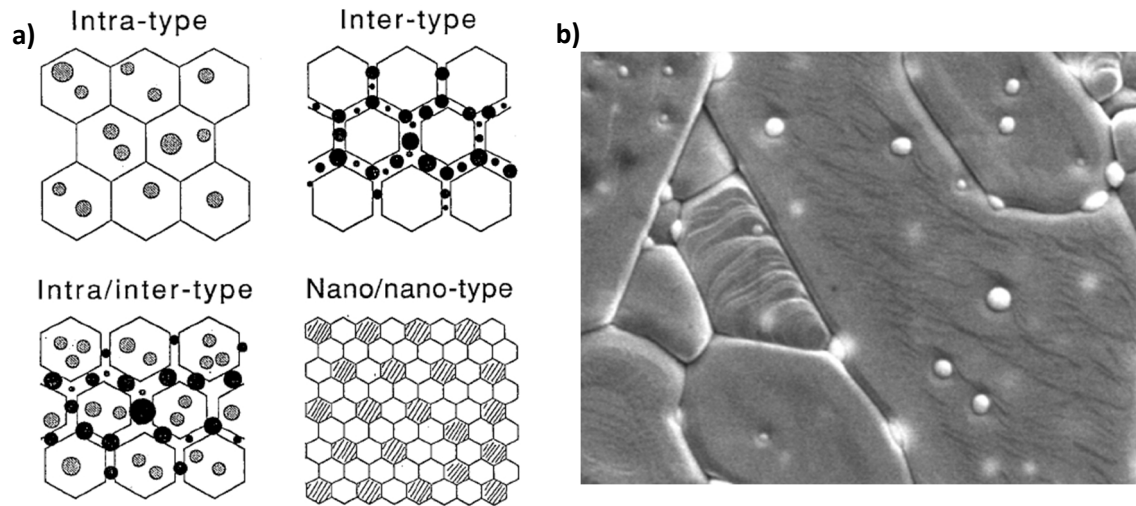
Figure 2.1: Sintered microstructures of nanocomposites: **a)** Niihara's classification of nanocomposites [1] and **b)** a SEM -image of a $Al_2O_3 - ZrO_2$ nanocomposite microstructure (where brighter phase is ZrO_2) [10]

It is important to understand that size is the key characteristic of a nanoparticle and all the new properties are due to this characteristic. Size matters in this case, but only in the opposite direction to common belief. This claim is justified in the next chapter, where we discuss about mechanical properties of ceramic nanocomposites and take a look upon the state-of-the-art of theory trying to explain the observed changes in these properties.

2.2   Mechanical properties of ceramic nanocomposites

The progeny of ceramic nanocomposites is indeed promising and in this chapter we discuss the mechanical properties of nanocomposites and link them in the state-the-art information published. It is somewhat clear that the interface between matrix and nanoparticles play the key role, causing the enhanced mechanical properties. These interfaces are still less studied within bulk ceramic nanocomposites and the principle of these interfacial properties is adapted from research made with thin coatings, such as the work of Veprek et al. [11]. The most unexpected results in mechanical properties presented in the next chapters, could be explained by the interfacial properties and large interfacial surface area between matrix and nanoparticles and other known phenomena discussed next.

2.2.1   Hardening of ceramic nanocomposite structures: Principles

Pecharromán et al. [9] found that to a certain small concentration limit of metallic nanoparticles, proposed to be the "percolation threshold", hardness of ceramic/metal composite rises steeply above the normal composite rule-of-mixture as shown in figure 2.2. It is also evident that this hardening behaviour is characteristic only to nanocomposites, as "normal" microcomposites seem to follow the rule of mixture near a critical concentration or 'percolation threshold'. Because the thermal expansion mismatch between ZrO_2 ($\alpha_{3YTZP} = 10.6 \times 10^{-6}$) and Ni ($\alpha_{Ni} = 13.3 \times 10^{-6}$) cannot explain this hardening effect, other mechanisms than residual stress induced hardening has been considered.
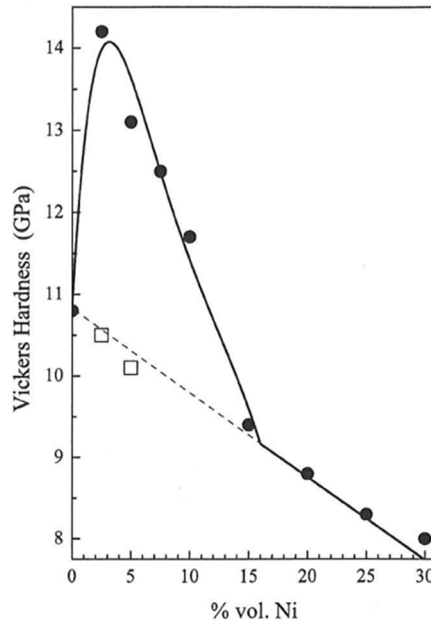
Figure 2.2: *Vickers hardness (H_v) of $ZrO_2 - Ni$ (-inter type) nanocomposites (•) and microcomposites (□) as a function of nickel concentration by volume. Dashed line represents the calculated hardness using the normal rule-of-mixture for composites. [9]*

Next two known hardening phenomena related to nanoparticles are introduced and later in chapter 2.2.2, a hardening model is presented for $ZrO_2 - Ni$ nanocomposite explaining the concentration limit or 'percolation threshold' for nickel nanoparticles. [8, 9]

2.2.1.1 The Hall-Petch relation

Mechanical properties of metallic polycrystalline materials at low temperatures, is mainly determined by movement of dislocations inside the grains. With decreasing grain size, the movement of dislocation pile-ups is hindered leading to increased hardness and rigidity of the matrix. Below a critical grain size, movement of dislocations slow down, plastic deformation is hindered and critical yield stress σ_Y, under which material starts to deform, increases according behaviour known as the Hall-Petch effect

$$\sigma_Y = \sigma_{Y0} + \frac{k}{\sqrt{d}},$$
(1)

where σ_{Y0} is the original yield stress of the bulk (Pa), k is a material constant and d is grain diameter (m). This equation states that critical stress needed to cause plastic deformation, and therefore hardness, increases with smaller grain sizes. For example copper with nano-sized grains can have up to 10 times higher hardness than with coarse grains (figure 2.3). Similarly covalent hard coatings (TiN, SiC etc.) with nano-sized grains are reported to have 3-5 times higher hardness than the same material with conventional grain size [8].
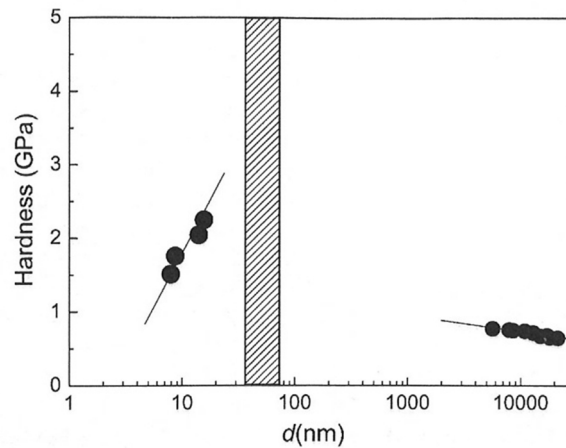
Figure 2.3: Hardness as a function of copper grain size. [8]

Hardness increase by Hall-Petch relation seems to have a definite grain size optimum for different materials, after which achieved strength is gradually lost or remains constant. This is commonly called the 'inverse' Hall-Petch effect. A model proposed by Mohammadabadi et al. [12] show grain size optimum of 11 nm for copper grains. Figure 2.4 represents the relation of the proposed model and the classic Hall-Petch.
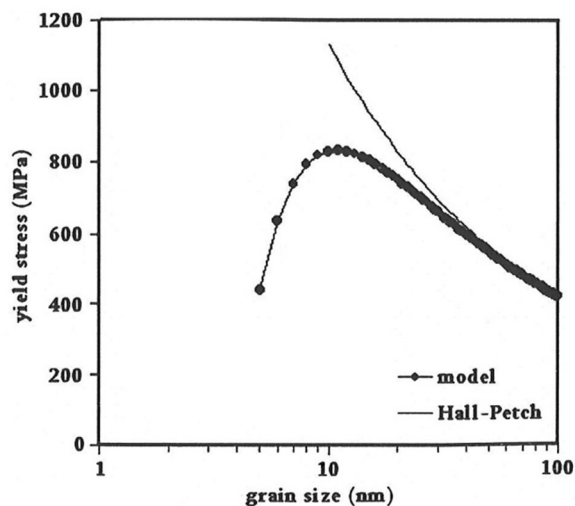
Figure 2.4: Predicted yield stress of Copper (Cu) as a function of grain size. [12]

Inverse Hall-Petch effect is not yet fully understood [12], but a general proposal is that the particles below critical size are not able to hold grain boundaries together, therefore enabling sliding of boundaries in respect to one another leading to softening of the material. Grain sliding phenomena relates to superplastic materials, which deform by grain sliding process in moderate temperatures. There is evidence that also ceramic nanocomposites can have superplastic behaviour in moderate temparatures [13].

2.2.1.2 Supermodulus effect

Another factor influencing hardness of nanocomposites is the enhancement of elastic modulus called the "supermodulus". Effect first discovered in multilayer metal thin films, has also been found in nanocrystalline materials. Model explaining this phenomenon assumes a rigid

crystalline nucleus surrounded by several layers of matrix atoms. These atoms are very poorly coordinated with the core and that causes compression to the core therefore increasing its elastic properties. [8, 9]

Influence of this phenomenon to hardness of nanocrystalline material is based on the nearly linear relationship of shear modulus and hardness in brittle materials. This relationship states that hardest materials (diamond, WC, $c - BN$) are most likely the stiffest as well. If this relation is true also for nanocrystalline materials, then an increase of elastic modulus will also increase the hardness. For metallic materials, the relationship between shear modulus and hardness is somewhat more random. Figure 2.5 shows hardness/shear modulus relationship of some non-metallic and metallic bulk materials. [8]
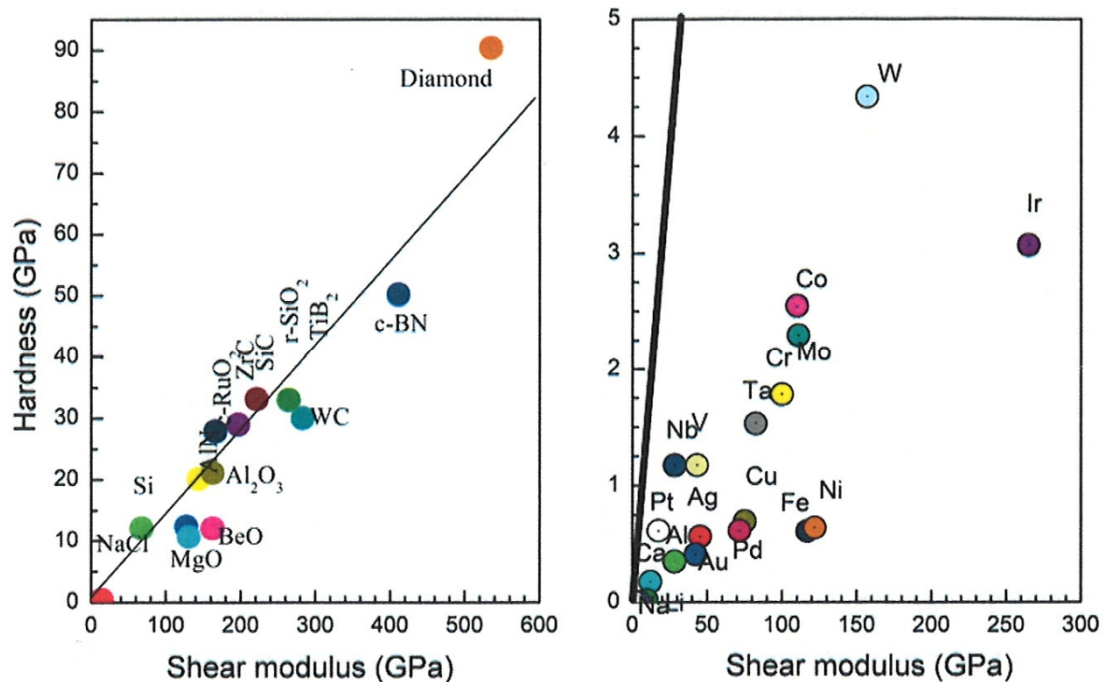
Figure 2.5: *Relationship between hardness and stiffness of some ceramic (left) and metallic (right) bulk materials. [8]*

2.2.2   Theoretical model for hardening of ceramic nanocomposites

Based on above phenomena, Pecharroman et al. [9] proposed in their study that the hardness increase in $ZrO_2 - Ni$ (-inter type) nanocomposite originates from two different mechanisms:

1) Intrinsic properties of the nanoparticles   (Hall-Petch effect)
2) Hard, thin shells of matrix coating the nanoparticles   (Supermodulus effect)

In this model there are two main aspects setting the limit for hardness growth. First the transition to 'inverse Hall-Petch' effect at a certain grain size optimum (≈ 10 nm) and second a limit given by the percolation theory which states that during synthesis, above certain concentration level, nickel particles will form networks which coalescence into larger particles during sintering therefore losing their original size related properties. This concentration limit is called the 'percolation threshold' and an example of this limit is shown in figure 2.6. Pecharroman et al. assumed that nickel particles in the size range of 10 − 40 nm dominate the mechanical properties of the composite, giving it the high observed hardness. Therefore when

the composite reaches the percolation threshold nickel concentration, 10 − 40 nm nickel particles disappear forming larger aggregates and losing their hardness. [9]
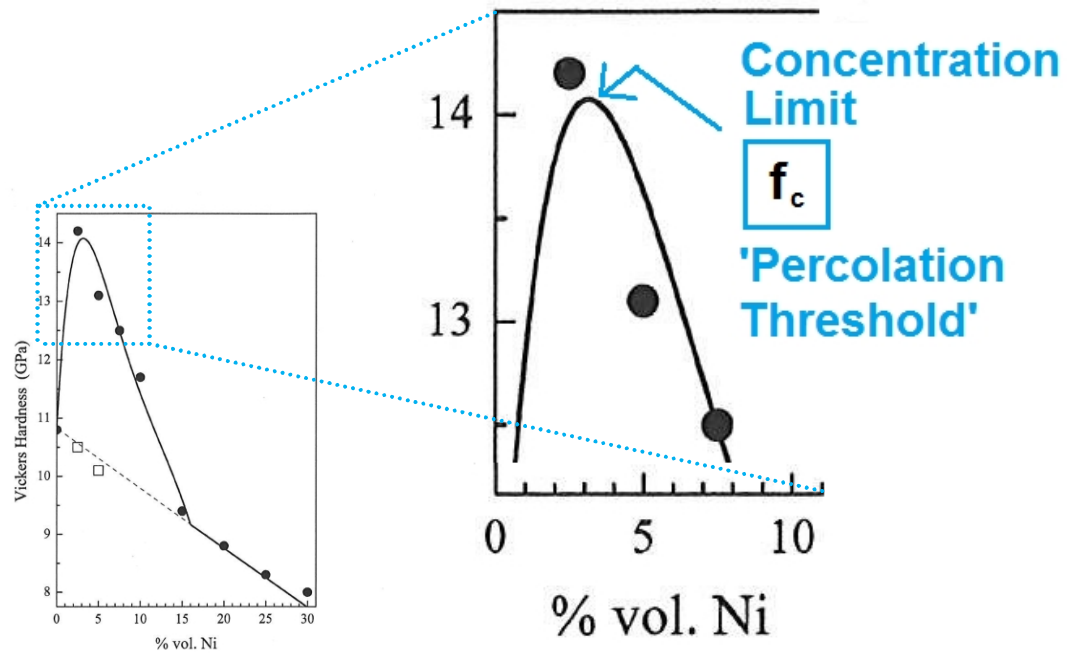
Figure 2.6: Concentration limit f_c or '*percolation threshold*' in $ZrO_2 - Ni$ nanocomposite [9]

TEM analysis indicates that nickel nanocrystals appeared to be coated with an amorphous or poorly crystallized layer of matrix atoms, which is thought to be the cause of 'supermodulus effect' hardening the core particle, which is nickel in this case [9]. TEM cross-section in figure 2.7 show the interface between zirconia and nickel, where zirconia is in the left and nickel in the right side.
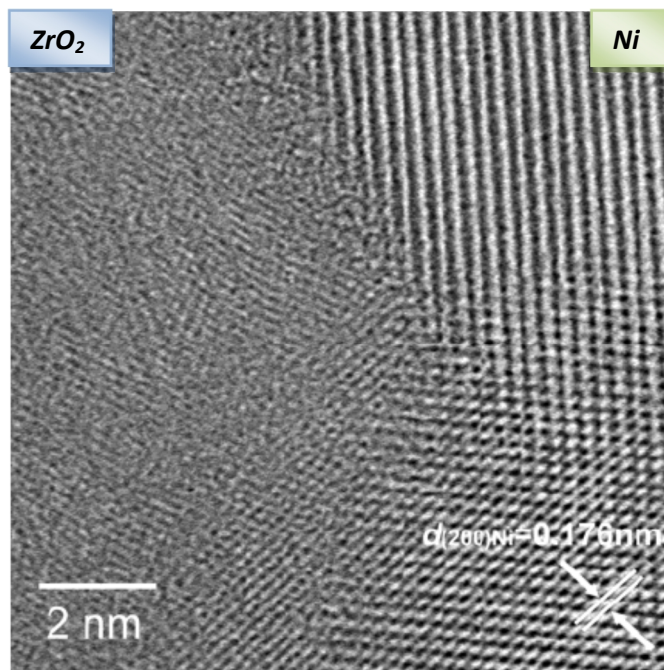
Figure 2.7: *TEM cross-section image showing the $ZrO_2 - Ni$ interface. [9]*

In a review of superhard nanocomposite thin coatings by Veprek et al. [11] summarise theoretical and experimental evidence that the 1 mono layer configuration of interfacial Si_3N_4 gives the extremely high hardness for $nc - TiN/a - Si_3N_4$ and $nc - TiN/a - Si_3N_4/TiSi_2$.

Pecharroman et al. stated that two main hardening effects of nickel nanoparticles on zirconia matrix are: **1)** pinning the dislocations at the interface of $ZrO_2 - Ni$, and **2)** blocking the zirconia grain sliding by hard nickel particles, therefore increasing hardness of the bulk material. Based on these assumptions and basic phenomena (Hall-Petch and supermodulus) they proposed a model, which attempts to predict the hardness dependence of nanoparticle concentration observed in nanocomposite structures (figure 2.6). Model deals nanoparticle and its matrix coating as a single hard phase. The remaining matrix will have original properties. Therefore nanocomposite hardness is a summand of rule-of-mixture and the effect of coated nanoparticles as

$$H_{composite} = \overbrace{H_{cer}(1-f) + fH_{met}}^{\text{Rule of mixture}}$$

$$+ f\varphi^\gamma \left[H_{met0}\varphi^h + \frac{D}{r_0}\left[3 + 3\frac{D}{r_0}\varphi^\gamma + \frac{D^2}{r_0^2}\varphi^{2\gamma} \right] (H_{met0}\varphi^h - H_{cer} + H_p) \right] , \qquad (2)$$

where the first two expressions correspond to the rule of mixture and the last one is the effect of the nanostructure [9]. H_{cer} is the original hardness of the ceramic matrix, f is volume concentration of second phase particles, H_{met} is the hardness of the bulk metal (in this case nickel), H_{met0} is the hardness of single phase composed by nanoparticle and matrix coating, f_c corresponds to percolation treshold, $\varphi = 1 - f/f_c$, γ is a critical exponent, $h = $ ½ for a classic Hall-Petch dependance, r_0 is the radius of single nanoparticle coated with a thin layer of thickness D. Closer examination of the equation is presented elsewhere. [8, 9]

Model fits also to data collected from $Al_2O_3 - Ni$ (-inter type) nanocomposites later tested by Moya et al. [3] In figure 2.8, composite hardness as a function of nickel nanoparticle concentration is presented, where dashed line represents the predicted values and solid line represents the composite rule-of-mixture.
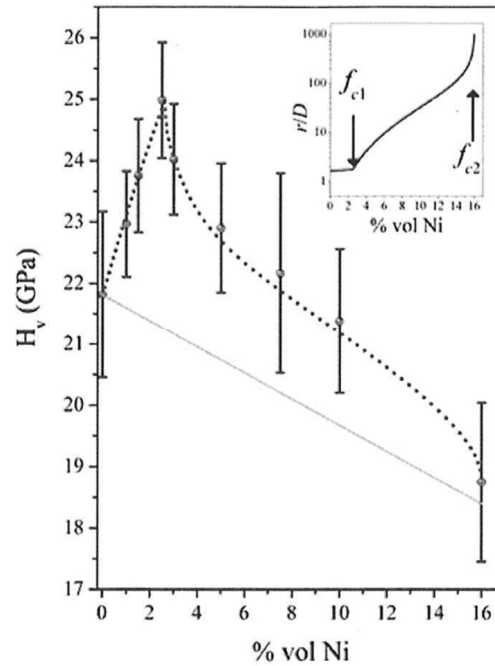
Figure 2.8: *$Al_2O_3 - Ni$ nanocomposite hardness as a function of nickel concentration by volume. Dashed line (···) represents hardness predicted by the hardening model and solid line (−) the normal composite rule-of-mixture. Black dots (●) represent measured hardness of alumina/nickel nanocomposite samples. Insert in the upper corner show the dependence of ratio between nickel particle radius and coat layer thickness (r/D) as a function of nickel content. [3]*

2.2.3 Toughening of ceramic nanocomposite structures: Principles

Engineering ceramics excel in many properties such as thermal resistance or mechanical strength but have inherently low fracture toughness. This is in many cases a limiting design factor when considering replacing e.g. machine part material with engineering ceramics. To overcome this deficiency, plenty of research has been made to enhance the fracture toughness of ceramic materials. The focus has been in deflecting or redistributing stress at the crack tip, including methods like crack surface bridging, particle dispersion of different phases in the matrix, fibre reinforcement and phase transformation induced toughening by zirconia. [7, 8]

Toughening mechanisms behind these methods are related to second phase micron size metal- and ceramic particles (including whiskers etc.) or second phase nano-sized metallic and ceramic particles [7, 14, 15]. Reducing size of the particles may have an effect on fracture toughness even in absence of bridging mechanism behind the crack front, or any other known mechanism [8]. As we discuss in chapter 2.2.4 nanoparticles ability to toughen the matrix may relate to a quite different kind of phenomena, such as dislocation movement in matrix particles during sintering caused by high residual stresses.

Early experimental results of toughening in ceramic nanocomposites were promising [1] and still extensive research is done in this field related to ceramic nanocomposites. Problem is that the recent studies have not able to repeat the Niihara's original findings therefore making them obsolete. Next we discuss the state-of-the-art in mechanism of toughening related to ceramic nanocomposites.

2.2.3.1 Toughening mechanisms for ceramic nanocomposites

Typical consequences observed with $Al_2O_3 - SiC$ (-intra/inter type) nanocomposites are

1) Reduced crack length in microintendation measurements   [16]
2) A partial change in fracture mode from intergranular to transgranular   [5]

As a direct consequence, higher fracture toughness and increased wear resistance values are measured [5, 16]. Many propositions have been made to explain the toughening mechanisms observed in the matrix. Grain boundary strengthening (or weakening) is the most notable difference between nanocomposite and the pure material. Nanocomposites have been observed to exhibit significantly less matrix grain pull outs during abrasive wear and polishing, which is linked to the observed transgranular fracture mode [5, 17]. The peculiar aspect of nanocomposites is, that largest increase in physical properties comes with a very small fraction of added nanoparticles (1-6 vol% mostly reported [3, 4, 5, 16, 17]). This can be related to percolation threshold limiting the most usable size fraction discussed in earlier chapters.

Addition of second phase nanoparticles in a ceramic matrix can in principle induce three basic types of strengthening mechanisms. Fracture strength will increase by [7]:

1.) Reducing flaw size (C-mechanism)   ⎫
2.) Increasing fracture toughness K_{IC} (K-mechanism)   ⎬— *Griffith equation*
3.) Strengthening of grain boundaries by internal stresses   (GBS-mechanism)

First two follow the Griffith equation for brittle materials which states that fracture strength (σ) is related to fracture toughness (K_{IC}) and flaw size (c) by:

$$\sigma = \frac{K_{IC}}{Y\sqrt{c}} \,, \tag{3}$$

where σ is the fracture strength [MPa], K_{IC} is the fracture toughness [$MPa\, m^{1/2}$], Y is the stress intensity factor of the crack tip governed by its shape (for example $2/\sqrt{\pi}$ in a half circle flaw) and c is the flaw size [m].

C-mechanism is related to another advantage observed with ceramic nanocomposites. The matrix grain size growth is inhibited by second phase particles pinning the grain boundaries. Smaller grain size leads to smaller critical flaw size (pores etc.) and possibly higher strength of the nanoparticles following the Hall-Petch relationship. Also because in most cases fracture begin and traverse along grain boundary, in optimal flawless structure, the grain boundaries determine the smallest flaw size. [5, 7]

K-mechanism is attributed to materials ability to deflect or redistribute stress of the crack tip or to bridge the wedge behind the crack front. This is commonly related to so called R-curve behaviour (relationship between fracture toughness and crack length) of brittle materials. A distinction between mechanisms in front and behind the crack tip needs to be pointed out when discussing ceramic nanocomposites. It is unlikely that any bridging elements are present in the wedge behind the crack front shown in the figure 2.9. In microstructural studies of $Al_2O_3 - Ni$ Kannisto et al. [18] found no evidence of plasticity in nickel particles. This is further supported by observed change of fracture mode to intra-granular in ceramic nanocomposites. Fiber reinforcement is the most used method that improves fracture toughness by bridging effect. Pure alumina can exhibit bridging toughening with growing grain size and modified grain shape such as $\beta - Si_3N_4$ where a needle shaped structure enhances fracture toughness by crack bridging.
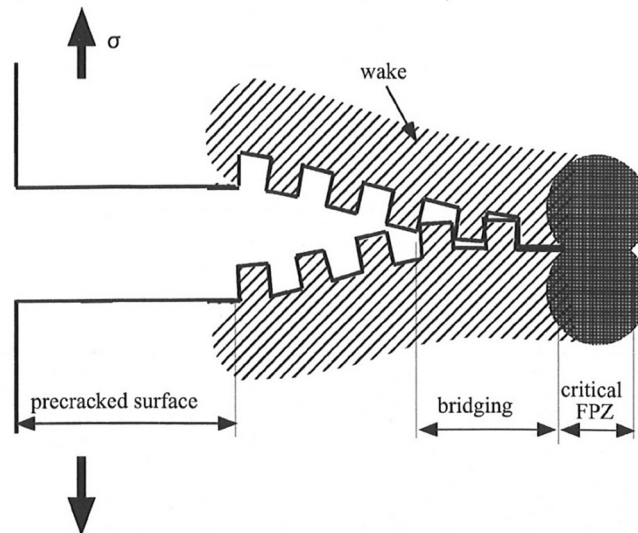
Figure 2.9: *Schematic model presenting frontal process zone and bridging effect in polycrystalline ceramics with R-curve behaviour. [19]*

Because of the lack of evidence of bridging effect in nanocomposites, only mechanisms acting in the frontal process zone (FPZ) needs to be considered. One proposed K-mechanism which suppresses the crack tip is, increasing the size of the FPZ and therefore redistributing stress at the tip to a larger area. This dislocation model for intra type nanocomposites proposed by Choi et al. [19] is discussed in the next chapter.

GBS-mechanism can be related to a well known phenomenon of phase transformation toughening by partly stabilized zirconia particles inside a ceramic matrix [20]. Kannisto et al. [18] concluded in their study of inter-type Al_2O_3 nanocomposites that most probably the cause of toughening is related to large mismatch in thermal expansion rates between matrix and second phase particles, which leads to a high residual stress state in the nanocomposite after sintering. The mechanism could be based on GBS-mechanism if the interfacial bonding is strong between the matrix and second phase particles. There is an analogy with the phase transformation toughening and thermal expansion mismatch toughening if the residual stress is compression after sintering. [7, 21]

An absence of unity in the field is evident when discussing the strengthening and toughening mechanisms of ceramic nanocomposites. The identification of toughening mechanism remains unclear because obtained levels of improvement are relatively small. Therefore there is no single persuasive mechanism that could explain all the characteristics of ceramic nanocomposites. The observed changes in fracture mode and improved fracture toughness provide a basis for the assumption of grain boundary strengthening (GBS-mechanisms). Phenomena has been tried to explain by compressive radial stresses present in composite grain boundaries, when matrix has a larger thermal expansion than the particle pinned in the grain boundary (for example $Al_2O_3 - SiC$). This model still fails to explain opposite situations where the nanoparticle has larger coefficient of thermal expansion and still improvement in strength and fracture toughness are observed (for example $Si_3N_4 - SiC$ or $Al_2O_3 - Ni$). In table 2.1 the summary of proposed strengthening and toughening mechanisms reviewed by Sternitzke in 1996, clearly indicated the absence of consensus in this area. Later reviews of ceramic nanocomposites by Choi et al. [21] and Moya et al. [8] still dwell on the same questions and acknowledge the need for better understanding of ceramic nanocomposites mechanical properties. [7, 19]

Table 2.1: Summary of proposed strengthening and toughening mechanisms for ceramic nanocomposites. [7]

Mechanism	Comment
Zener grain boundary pinning (c-mechanism)	Matrix grain sizes are drastically reduced (typical for nanocomposites)
Dislocation networks (c-mechanism)	Refinement of microstructure is observed (no effect for strength increase)
Reduction in processing flaw size (c-mechanism)	Strength increase can be fully explained by observed change in processing flaw type (careful processing is very important)
Crack healing (c-mechanism)	Can explain strength increase after annealing (mechanisms are still unclear)
R-curve effects (K-mechanism)	steep rising R-curve behaviour is proposed (no experimental evidence)
Crack deflection (K-mechanism)	Cracks seem to be reflected at SiC particles (importance for toughening is unclear)
Crack bowing (K-mechanism)	Experimentally difficult to verify (importance for toughening is unclear)
Thermal expansion mismatch (grain boundary strengthening)	Fracture mode is changed to transcrystalline if $\alpha_{particle} < \alpha_{matrix}$ (e.g. for Al$_2$O$_3$/SiC)
Average internal stresses (grain boundary strengthening)	Average tensile stresses in matrix if $\alpha_{particle} < \alpha_{matrix}$ (toughness is reduced)
Local stress distribution (grain boundary strengthening)	Local compressive stresses can strengthen grain boundaries if $\alpha_{particle} < \alpha_{matrix}$ (can explain change in fracture mode)

Advances in determining the mechanical behaviour is expected only when the characterization methods are available to study the matrix and second phase particle interface. Next a fresh view of dislocation based ceramic toughening and strengthening is discussed, which attempts to unify the test results.

2.2.4 Dislocation induced toughening model for ceramic nanocomposites

Most recent model to describe toughening process in $Al_2O_3 - SiC$ (-intra type) nanocomposites was proposed by Awaji et al. in 2002 [19] and later described by Choi et al. [21] in 2005 as the "dislocation model" discussed in chapter 2.2.4.2. It was proposed mainly on the basis of $Al_2O_3 - SiC$ nanocomposite characteristics. As the main source of toughness and strength enhancements they proposed the intra-type inclusions of nanoparticles in the alumina matrix grains as shown in the figure 2.10.
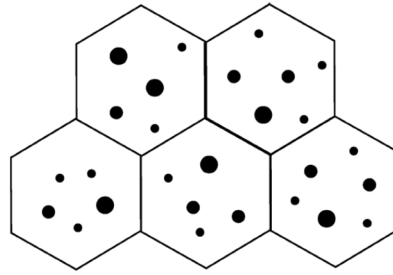
Figure 2.10: *Intra-type nanocomposite structure. [21]*

Niihara proposed already in 1991 that nanocomposites having most of the inclusions located within the alumina grains show best improvements in properties [1]. This has been backed at least by studies of Nishimura [22]. The proposed model is essentially based on K-mechanism where the increased size of the FPZ will redistribute stress at the crack tip. As an introduction to dislocation model, dislocations in ceramic materials are next discussed briefly.

2.2.4.1   Dislocation movement in ceramic matrices

Dislocations in ceramics are often immobile in room temperature, therefore leading to crack propagation when a critical stress level is reached. Still dislocation movement is possible and furthermore at sintering or annealing temperatures, highly probable. Amount of energy needed to induce dislocation movement in crystalline material is called the Peierls-Nabarro (PN) stress denoted by τ_{PN} and defined as: "The shear stress τ in the slip plane in the slip direction which is required to bring a dislocation into motion at a temperature of 0 K in a crystal without defects." A slip is a basic plastic deformation process, which propagates gradually through dislocation gliding rather than moving the whole slip plane at once (would require an enormous amount of shear). At higher temperatures shear stress needed to induce this dislocations gliding will be smaller due to thermal activation or vibrational energy. Also any existing dislocations will further increase the energy needed. [23]

For covalent crystals such as Si, Si_3N_4 and SiC directional covalent bonds must be alternately broken and formed to enable dislocation movement. Because of high bonding energies, this will result in high PN barrier or core energy which needs to be overcome with every covalent bond created and destroyed to allow dislocation movement. This leads to a large τ_{PN}. Because cracks are able to propagate stresses below τ_{PN} they will dominate deformation and lead to brittle fracture. In more complex ionic crystals, such as Al_2O_3 or spinel $Al_2O_3 \cdot MgO$ the situation is quite similar. Complex regrouping of the ions after dislocation, together with a large burgers vector (direction and size of a single dislocation step) corresponds to a high τ_{PN} in magnitude of covalent crystals. The calculated value is in order of approximately $10^{-2} \times$ shear modulus G or $\approx$10000 MPa. Also in complex ionic crystals the energy needed for dislocation movement is significantly decreased in elevated temperatures. Thus in principle, covalent and ionic crystals are capable of deforming plastically, although at higher temperatures and higher stresses than metallic crystals. Plastic behaviour is closely related to the size of particles in question. [23]

Recent real time TEM experimental results indicate that transition $\gamma - Al_2O_3$ is able to undergo full plastic deformation under compression when the size of particles is 40 nm. However 125 nm particles did undergo brittle fracture which indicates that there is a size limit for plastic deformation of $\gamma - Al_2O_3$. [24]

In practice this means, for example, that experimental methods relying on plastic deformation are possible also for ceramics, mainly concerning the hardness measurements by indentation. Ceramics inherence towards cracking in stress can be exploited when evaluating

fracture toughness of the material. When considering the laborious four-point bending tests, the indentation method has been widely accepted as evaluation method for fracture toughness.

2.2.4.2   Dislocation model

Basis of the model is in the thermal expansion (CTE) miss-match between alumina and silicon carbide embedded inside alumina grains, which will induce residual stresses in the surrounding matrix grain after sintering. The thermal expansion has a ratio of approximately 2/1 between Al_2O_3 and SiC. Residual stresses induced by CTE-mismatch was earlier analysed by Awaji et al. [19]. They proposed a simplified model which consisted of a spherical particle within a concentric matrix sphere surrounding the particle. Model is presented schematically in figure 2.11.
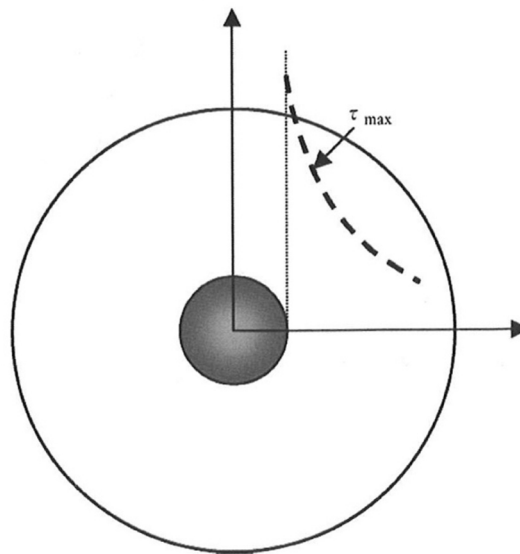
Figure 2.11: *Shear evaluation model presenting particle inside a matrix and residual shear stress as a function of distance from particle/matrix interface. [21]*

As presented in the figure, residual shear stress decreases rapidly as a function of distance from the particle/matrix interface and shows a considerable shear close to the interface. Values for residual stresses in $Al_2O_3 - SiC$ nanocomposites were calculated assuming that temperature difference was 1570 °C and the ratio between particle/matrix radius was 1/5. Calculated values are shown in table 2.2 with suffix 'p' indicating particle properties and suffix 'm' indicating matrix properties. [19, 21]

Table 2.2: *Calculated residual stresses along the particle/matrix boundary in nanocomposites fabricated by Niihara (1991) with ΔT =1570 °C and particle/matrix radii ratio 1/5. [19]*

| System	$\alpha_m/\alpha_p \times 10^{-6}$ (K^{-1})	E_m/E_p (GPa)	ν_m/ν_p	τ_{max} (GPa)
Al_2O_3/SiC	8.8/4.7	380/490	0.21/0.19	1.71
Si_3N_4/SiC	2.6/4.7	280/490	0.26/0.19	0.70

Based on the work of Lagerlöf et al. [25], temperature dependence of the critical shear stress needed to produce a basal slip and prism plane slip in α-alumina single crystal, can be denoted with a simple logarithmic scaling law

$$\tau_{cb} = \ln \tau_{0b} - 0,0052\, T \tag{4}$$

and

$$\tau_{cp} = \ln \tau_{0p} - 0,0026\, T \tag{5}$$

where τ_{cb} is the critical stress for basal slip and τ_{cp} the critical stress and prism plane slip, T is the temperature in Kelvins [K] and $\tau_{0b} = 109\, Gpa$ for basal slip and $\tau_{0p} = 9\, Gpa$ for prism plane slip. In figure 2.12, residual stress of $Al_2O_3 - SiC$ nanocomposite and critical shear for basal and prism plane slip movement are plotted as function of temperature to show the effect of thermal activation. Residual stress caused by thermal expansion mismatch is assumed to behave linearly with temperature. [21]
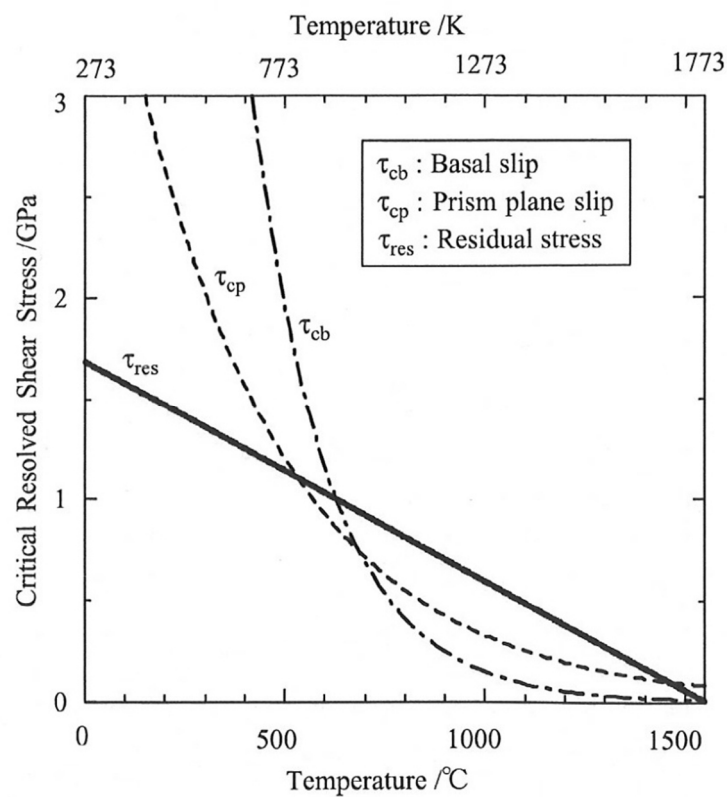
Figure 2.12: *Thermal activation of basal slip and prism plane slip in α-alumina single crystal, and their relation to residual stress caused by CTE-mismatch in $Al_2O_3 - SiC$ nanocomposite. [21]*

The figure effectively shows that based on calculations of Lagerlöf et al. and Choi et al., dislocation movement near the interface of particle (SiC) and matrix (Al_2O_3) could be possible due to residual stresses at temperatures of approximately $600 - 1400$ °C. [21, 25]

Because the residual stress reduces quickly as the distance from the interface increases (figure 2.11), only small defects such as dislocations, are possible to create in the vicinity of the nanoparticles. Dislocations created below sintering temperatures are considered to become nuclei for nano-sized cracks at room temperature, because the critical stresses of basal and prism slips are at room temperatures 23.1 GPa and 4.2 GPa according to equation (4) and (5), while theoretical strength of α-alumina is only 2.6 GPa. This model stresses the importance of post sinter annealing. Due to fast decreasing residual stress gradient at the

particle/matrix interface, the dislocation are pinned next to the nanoparticles during sintering (figure 2.13 a). When annealing the dislocation are able to disperse in the matrix grain (figure 2.13 b). This will enhance the ability to increase the FPZ size.

A Creation of dislocations   **B** Dispersion of dislocations
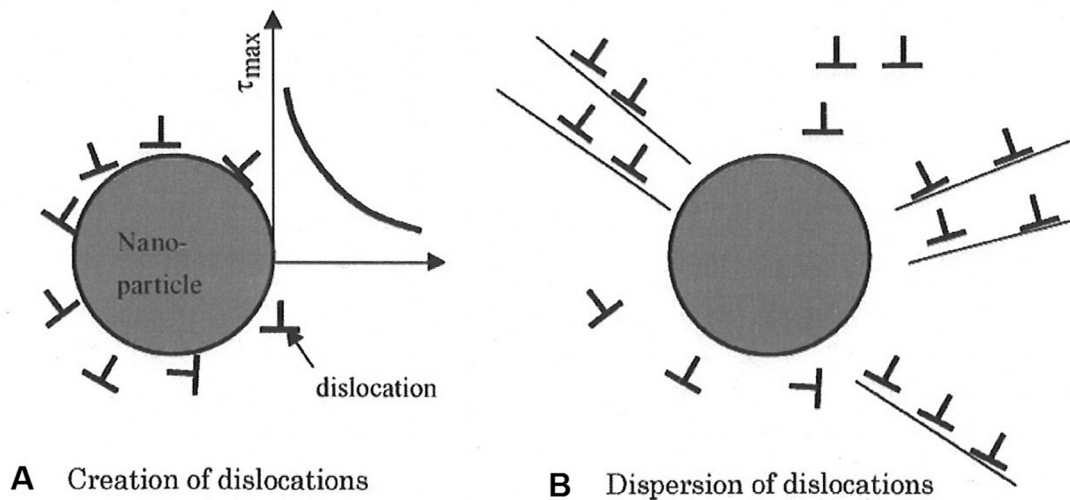
Figure 2.13: a) Dislocations in vicinity of the nanoparticle after sintering and b) after annealing at medium temperature. [21]

These dispersed dislocations can be assumed to form sub-grain boundaries or dislocation networks around the SiC particles (figure 2.14 a), which operate as nanocrack nuclei in the highly stressed FPZ in front of the crack tip (figure 2.14 b). Crack tip energy is released by the nanocracking and expands the size of the FPZ resulting in improved fracture toughness. [19, 21]
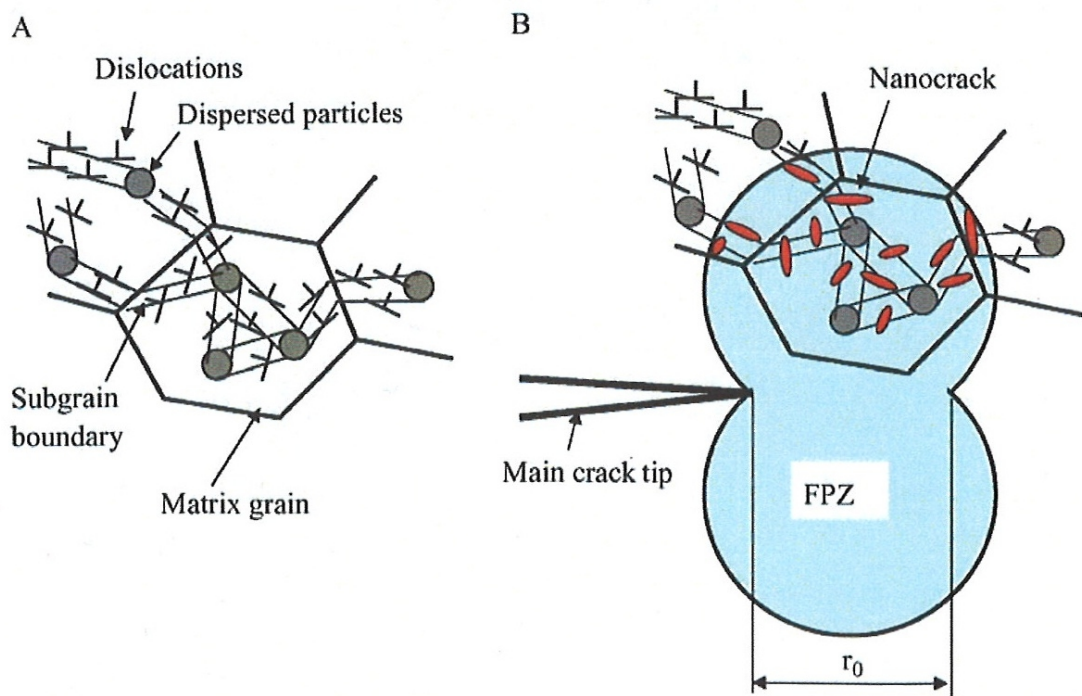
Figure 2.14: a) Intra-type nanocomposite structure after annealing and b) FPZ influenced by nanocracking leading to enhanced fracture toughness. [21]

2.2.4.3 Experimental results concerning dislocation model

The relation between frontal process zone size and fracture toughness has been observed with $Al_2O_3 - Ni$ and $Al_2O_3 - Ag$ nanocomposites. Results listed in table 2.3 show increases in both fracture toughness and FPZ size when samples were annealed after sintering in 800 °C for 5 minutes. [26]

Table 2.3: Property summary of monolithic alumina and as-sintered and annealed $Al_2O_3 - Ni$ and $Al_2O_3 - Ag$ nanocomposites. [26]

	Monolithic alumina		As-sintered alumina-Ni nanocomposites	Annealed alumina-Ni nanocomposites
	original	modified*		
Strength σ_B/MPa	521	781	877	888
Fracture toughness K_{IC}/MPam$^{1/2}$	3.78	3.78	5.49	7.59
FPZ size r_0/μm	4.86	1.76	3.36	7.31
Critical local stress σ_c/MPa	684	1140	1190	1120
$\sigma_B \cdot r_0^{1/2}$/MPam$^{1/2}$	1.14	1.04	1.61	2.4
Plastic zone size r_y^*/μm	12	4.3	8.4	18

*The strength declined by the residual stresses was assumed to be 260 MPa.

	As-sintered alumina-Ag nanocomposites	Annealed alumina-Ag nanocomposites
Strength σ_B/MPa	780	810
Fracture toughness K_{IC}/MPam$^{1/2}$	3.6	4.21
FPZ size r_0/μm	1.56	2.11
Critical local stress σ_c/MPa	1150	1157
$\sigma_B \cdot r_0^{1/2}$/MPam$^{1/2}$	0.97	1.18
Plastic zone size r_y^*/μm	3.9	5.2

Ways to calculate the size of the FPZ have been developed, but are discussed elsewhere [see refs. 21, 26]. The dislocation model has also been proposed to explain the observed strengthening and fracture mode change in nanocomposites [21]. It has been also observed that critical FPZ size of the nanocomposites r_0 is not always larger than that of bulk alumina although there is an increase in fracture toughness, as shown in table 2.4 between pure alumina and $Al_2O_3 - SiC$ nanocomposite [21]. Therefore other proposed comparison is the product of flexural strength and square root of FPZ size denoted as $\sigma_B \times r_0^{1/2}$ in the table 2.4. This proposal is based on the increased strength by dislocation dispersion. Some evidence for this proposal has been collected in table 2.4.

Table 2.4: Experimental results for mechanical properties and FPZ size of Al_2O_3 and Al_2O_3 matrix nanocomposites. [21]

Specimens	Fracture strength σ_B (Mpa)	Fracture toughness K_{IC} (MPa m$^{1/2}$)	Critical FPZ size r_0^* (r_0) (μm)	$\sigma_B r_0^{1/2}$ (MPa m$^{1/2}$)
Al_2O_3	462	3.72	10.3 (6.9)	1.21
Al_2O_3/ 5 wt%Ni	462	4.00	11.9 (9.0)	1.39
Al_2O_3/ 3 vol%SiC	760	5.06	7.1 (5.3)	1.75

Based on presented information the toughening in nanocomposites is reasonably well explained by dislocation model, but it still lacks explanation for the connection of fracture strength and FPZ size. Awaji et al. have shown later more results implicating that when aiming to increase fracture toughness, both fracture strength and FPZ size must be taken into account [26].

The most interesting finding is that shown results of $Al_2O_3 - Ni$ nanocomposites can be compared to previously discussed study of Moya et al. [3] regarding hardness and wear resistance of $Al_2O_3 - Ni$ nanocomposites. Moya et al. approach the issue from another point of view, explaining mechanisms leading to enhanced hardness, smaller matrix grain size and thus better wear resistance of the nanocomposite. When we evaluate wear resistance it would be beneficial to improve both hardness and fracture toughness simultaneously. Although the results presented above are consistent, the most significant lack of dislocation model is that it is solely proposed to intra type nanocomposites structures and fail to account for improvements observed in nanocomposites where particles are located at grain boundaries, such that is the case in the experimental part of this study and many other studies [3, 4, 9].

3. Processing of ceramic nanocomposites

The basic processing steps used in manufacturing ceramic solids are presented in figure 3.1. Instead of only revising these steps, the point of view for this thesis has been taken from aspects unique to processing of nanoparticles and nanocomposite structures. Plenty of good books on ceramic processing exist and I see no meaning in only reviewing these works. The excellent work of Mohamed N. Rahaman [27] and James S. Reed [28] were used as a basis when planning the ceramic processing presented in this thesis.
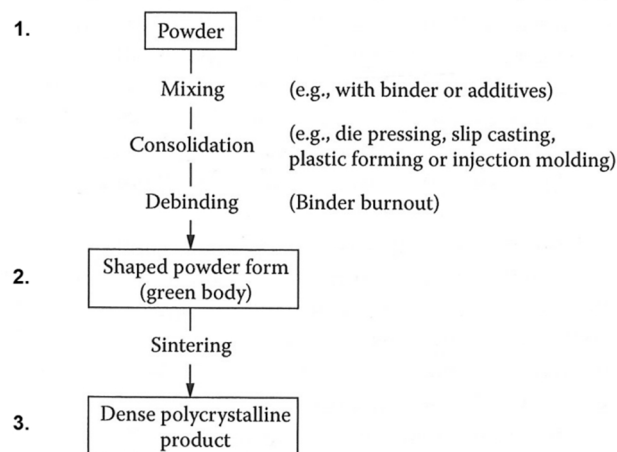
*Figure 3.1: Typical processing steps to make ceramic polycrystalline solids, **1.)** start with a powder, **2.)** formed into a green compact and **3.)** sintered into a solid. [27]*

With size come certain advantages and disadvantages. Small size and therefore large surface area/surface energy allows densification to happen in much lower temperature. Disadvantage is that the colloidal processing is much harder to control. For example in slip casting, large surface area enables only moderate solid versus liquid percentage and the small particle size greatly inhibits the filtration speed.

Flaws occurring in any phase of the processing remain unaffected through the rest of the processing. Preventing these accumulating flaws is the main aspect in industrial manufacturing of ceramics as they are the main cause of high neglect rates [27, 28]. Nanopowders are difficult to process dry [18], so wet methods are introduced in the coming chapters and they are used throughout the experimental part of this thesis.

3.1 Classification of ceramic powders

Before discussing in detail about the processing of raw materials, it is necessary to classify the different forms of particles that exist in raw powder. Figure 3.2 shows a schematic presentation of different types of particles and SEM image of Al_2O_3 powder in figure 5.6 illustrates the real situation.
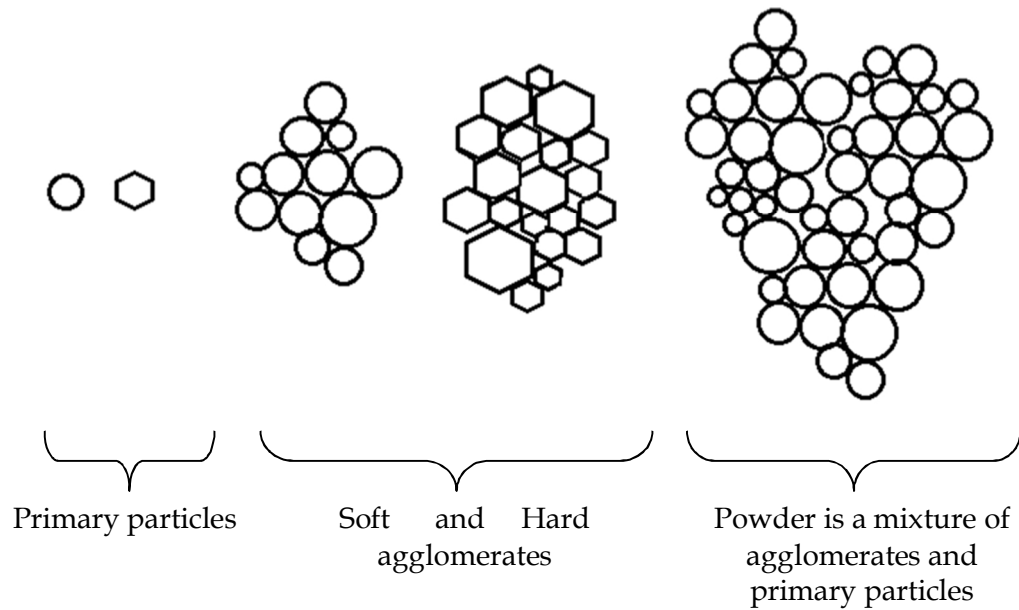
Figure 3.2: Classification of ceramic particles and powders

'*Primary particles*' are dense single or polycrystalline units which can be divided only with high mechanical energy, hard milling etc. In dry and wet conditions primary particles tend to form larger clusters which are called agglomerates. Two types of agglomerates can form, soft and hard. Soft agglomerates are held to together by weak surface forces and are easily broken by milling or ultrasonic agitation. Hard agglomerates form strong chemical bonds and are harder to break down with milling and even harder with ultrasonification. The word '*particle*' can represent primary particles, agglomerates or a combination of both. Other terms used for clusters are '*granules*' and '*aggregates*'. Clusters that form in liquid are called '*flocs*'. Size range of different particles is presented in table 3.1. [27]

Table 3.1: Approximate size range and definitions of different types of particles and clusters by Rahaman [27]

Colloidal Particle	1 nm – 1 µm
Coarse Particle	1 µm – 100 µm
Granule	100 µm – 1 mm
Aggregate	> 1 mm

Even theoretically with mono sized powder, it consists of both primary particles and agglomerates and therefore when average particle size of a powder is measured; test gives a certain size distribution, rather than a specific value. [27]

3.2   Colloidal processing of ceramic nanopowders

Understanding the wet colloidal processing is essential in the production of ceramics in general. The importance is more pronounced when nanoparticles are involved. Packing of particles in green state (Green density) is directly related to final sintered density of the solid and therefore needs to be considered carefully. In a composite structure controlling the dispersion of both or all constituents is also essential to obtain the best dispersion and finest microstructure.

Word '*colloid*' or '*colloid suspension*' indicates a liquid that is mixed with powder consisting of particles or flocs with a size approximately of 1 nm to 1 µm. Size of the particles indicates that effect of gravity can be neglected and the forces between the particles determine the state in which particles reside in the suspension. The '*stability*' of the suspension represents the colloidal state in which the particles reside. They can be '*flocculated*' aka forming particle clusters or they can be '*fully dispersed*' aka primary particles reside separately in the suspension. If the latter state is present in the suspension, it is said to be fully stable colloid or suspension (Fully stable colloids are rare). To form nearly stable suspension, surface charge forming in the double layer located on top of the particles needs to have sufficient repulsion force to overcome the van der Waals, or the weak attraction force between particles. The overall interparticle potential energy can be expressed as

DLVO theory

$$V_{total} = V_{vdW} + V_{elect} + V_{steric} + V_{structural} \quad , \tag{6}$$

where V_{vdW} is the attractive long-range van der Waals potential energy, V_{elect} is the repulsive potential energy caused by electrostatic interaction between particles with the same sign, V_{steric} is the repulsive potential energy resulting from steric interactions of adsorbed polymeric species and $V_{structural}$ is the potential energy of nonadsorbed species, which can increase or decrease the suspension stability. First two terms of the equation (6) form the basis of DLVO theory, corner stone of modern colloidal science. [29]

Interaction of these forces can be presented in a potential energy diagram shown in figure 3.3, where the bold line represents the sum of forces between particles.
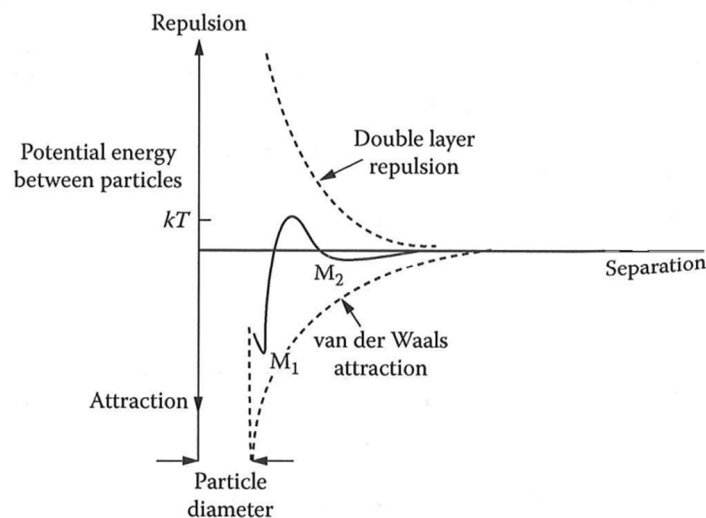
Figure 3.3: *Potential energy diagram between van der Waals attraction and double layer repulsion. M_1 represents a state of highly flocculated suspension and M_2 represents a state of weakly flocculated suspension which is often more desired considering slip casting methods.*
[27]

If hard clusters are formed, with the help of for example capillary forces or external heat, larger mechanical energy is needed to separate primary particles by, for example ball milling before full dispersion can be reached. That is the case in powder formed with granulation methods, such as spray drying.

Step to consider with nanocomposites is also the dispersion of the second phase particles inside the matrix. If we are unable to mix the two separate phases well, we end up

with processing flaws (see figure 3.2) that hamper the quality of the end product. Overall the importance of processing for the quality of the end product needs to be underlined. To be able to control the particle packing we must eliminate floccing of particles or control the floc size and shape so that good packing is achieved. For optimal packing, particles need to fully dispersed or be in a non-aggregated form. In theory, smaller particle size and narrow size distribution as well as uniform, preferably round particle/primary particle morphology is desirable to obtain best possible packing. [27]

Viscosity of the suspension increases with increasing solid content due to decreasing space between particles which leads collisions between particles and can increase flocking. When solid content remains constant but particle size is smaller the distance between particles also becomes smaller. Explanation for this follows: An external layer (Double layer or adlayer of adsorbed polymer) on top of the particles induce the repulsive forces that keep two particles apart. This layer has a certain thickness and it is added to the particle diameter to give the total diameter. If we assume that thickness of the layer is constant, small particles will have relatively thicker double layer compared to large particles. With 250 nm particle size, a 10 nm layer has only minor effect. Instead with a 10 nm particle, 10 nm layer has a major effect on achievable packing density. With approximately 12 vol. % of 10 nm particles with 10 nm layer on top, the liquid is at packing density of 60 vol. %. The situation is illustrated in figure 3.4. [29]
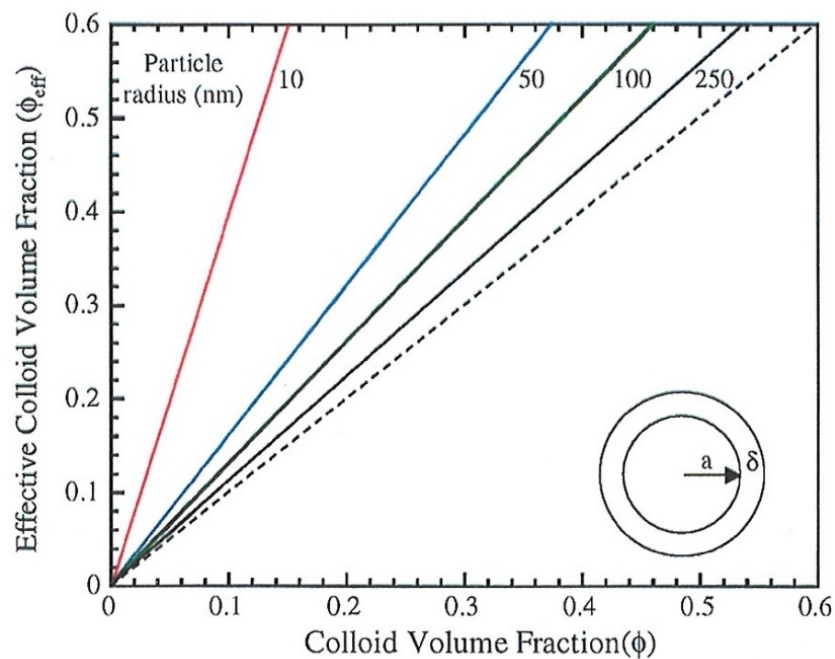

Figure 3.4: *Effective colloid volume fraction as a function of real colloid volume fraction. Lines (–) indicate systems with varying particle radius a [nm] and δ = 10 nm. Dotted line (---) indicates a 250 nm system with δ = 0. [29]*

3.3 Forming of green compacts by slip casting

3.3.1 Slip filtration using a porous mould

Slip casting takes advantage of the capillary forces that liquid/air interface exhibits inside a small pore or a tube also known as capillary. Desired mixture of powder is mixed with liquid to produce a 'slip', of which viscosity needs to be sufficiently low to allow capillary flow of the liquid through the mould. Mould is made out of porous, permeable material onto which the slip is poured. Traditional mould material is gypsum ($CaSO_4 \cdot 2H_2O$). Capillary force caused by micropores draws the liquid out of the slip with an approximate pressure of 0.1 - 0.2 MPa and filtrates the liquid into the pores. Filtration force leaves tightly packed layer of particles onto the wall of the mould, which slow down the filtration further as the layer grows. As the resistance to flow increases, the growing particle layer gives the process a maximum wall thickness with different slurry parameters. The object that is produced is often referred as a 'green' compact, which consists of particles in contact with porosity between them. [27]

The packing of particles defines the green density of the compact and is influenced by stability of the slip and by the particle size, shape and size distribution. For the filtration process of nanocomposites, we need to consider the liquid permeability of the packed layer or 'cake'. The more tightly it is packed, the more it will hinder the filtration leading to slower casting time. Problem that arises with fully stabilized nanopowder slurry is that it makes a very dense layer onto the mould making the filtration a very slow process. Therefore it is advantageous to leave the slurry in semi-flocculated state, which means controlled de-agglomeration process time. In slip larger particles and flocs of same size can be though behaving as the same but slip casting with larger particles will leave more porosity and give a lower green density and weak flocs of the same size will give better green density because the capillary forces can collapse the flocs when the green object is drying. In the case of flocs collapsing, the drying shrinkage is greater. When using nanoparticles the advantage of flocs is that they give much faster filtration rate. Figure 3.5 illustrates the filtration process of slip in a porous mould.
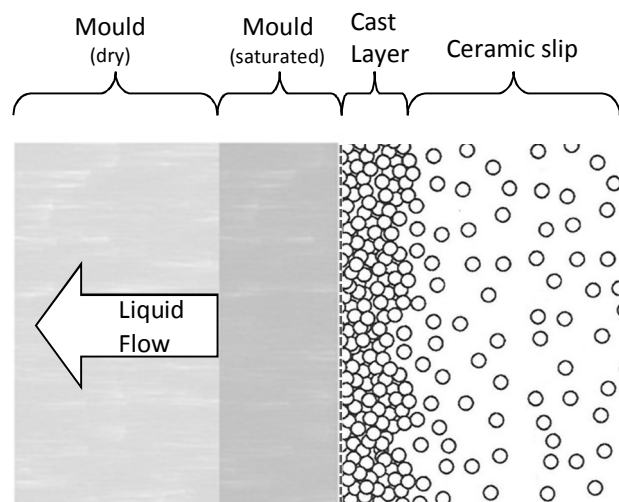
Figure 3.5: Schematic presentation of the filtration process of slip casting with fully dispersed slip).

Growth speed of the cast layer can be estimated by a modified kinetic model (Adcock and McDowall 1957) which assumes negligible gravity sedimentation

$$\beta_{gr}\ (Growth\ rate) =\ \{2Pt\ /[n\eta\varepsilon_m(n\alpha_m + \alpha_c)]\}^{1/2}, \tag{7}$$

where P is pressure (Pa) caused by capillary suction, t is time, η is viscosity of the liquid, n is a mass balance factor equal to $(1 - c_s - \varepsilon_c)/c_s$, where c_s is volume fraction of solids in the slip and ε_c is the volume fraction of pores in the cast layer, ε_m is the volume fraction of pores in the mold, α_m and α_c are the specific hydraulic resistances of the mould and cast layer respectively. Growth rate of the cast layer decreases with time, therefore giving the cast layer a maximum thickness. Model predicts that growth rate of the cast layer increases when the hydraulic resistances α_m and α_c decrease or when $P, c_s, \varepsilon_m\ and\ \varepsilon_c$ are increased. [27, 28, 30]

Specific flow resistance of the cast layer can be estimated by using modified Carman-Kozeny model [30]

$$\alpha_c = (5S^2\rho_{cl}{}^2)/(1 - \rho_{cl})^3, \tag{8}$$

where S is the specific surface area of the powder and ρ_{cl} is the density of the cast layer (ratio between pores and solids). Permeability is highly influenced by the particle size of powder and packing density of the forming cast layer, which evidently slows down the filtration when using nanoparticles. With value of $\rho_{cl} > 0.5$ and sufficiently high surface area of powder, cast layer will have a very low permeability (high α_c) that dominates the flow resistance. Under these conditions α_c greatly exceeds α_m and equation (7) can be simplified by setting $\alpha_m = 0$. In order to reduce [27, 30]

Viscosity is the measure of force needed to put the liquid in motion or in other words the liquids ability to inhibit motion. Higher viscosity means higher force is needed to stir the liquid. Viscosity is influenced by the packing density of particles in the liquid and their ability to form flocs. Often with ceramic colloids or slips, the viscosity is behaves as 'shear thinning', meaning that with increasing shear force the viscosity of the liquid lowers non-linearly because of flocs breaking down. These kinds of fluids are called non-Newtonian. In contrast the viscosity of Newtonian liquid behaves linearly to shear force. In slip casting, low viscosity is a key parameter because it enables the particles to have the best packing capability (in absence of flocs), it helps to fill the mould with slip and it ensures that there is no heterogeneity in different parts of the green compact.

3.3.2   Slip raw materials and processing

The basic slip has 3 components: Solvent (water, alcohol etc.), a powder solid (Al_2O_3, SiC etc.) and dispersing agent (PMMA, NHPA etc.). To enhance the mechanical properties and therefore ease the handling of green casts, binders (Natrium carboxymethylcellulose etc.) and plasticizers (Poly ethylene glycol (PEG) etc.) can be added. Also surface tension modifiers (Agitan™, alcohol etc.) can be used to prevent bubble formation in the slip during mixing. In summary the optimal slip will have narrow or bimodal particle size distribution, low viscosity and high solid content. [27]

Most important additive is the dispersant. The optimal amount of dispersant is empirically tested for different raw materials and for different particle size distributions. Total surface area of the powder ultimately determines the amount of dispersant needed. At the optimal concentration of dispersant, slip has a viscosity minimum and if more dispersant is added viscosity starts to slowly rise again as depletion flocculation takes place [31, 32]. Common dispersing chemicals for high solid loading slips are polyelectrolytes: poly(methyl

methacrylate) or PMMA and ammonium polyacrylate or NHPA, which give the particles electrosteric repulsion. [27, 28]

Table 3.2 lists slip recipes used in preliminary studies of this thesis using two $\alpha - Al_2O_3$ powders with different specific surface areas (SSA).

Table 3.2: *slip recipes of preliminary studies for two $\alpha - Al_2O_3$ powders with different specific surface areas*

Powder type	MR70 (Albemarle) (SSA 6-10 m^2/g)	TM-DAR (Taimei Chemicals) (SSA 14.5 m^2/g)
Raw materials		
H$_2$O [wt. %]	24	30
Powder [wt. %]	76	70
Solid content	≈44 vol. %	≈37 vol. %
Additives		
Dispersant [wt. % Pdw.*]	0.4 (NHPA - Dispex A40)	2.2 [32] (PMMA - Darvan C-N)
Binder [wt. % Pdw.*]	2.0	-
Plasticizer [wt. % Pdw.*]	0.33	-
Surface tension modifier [ml]	-	0.5 – 2 (Agitan™ or ethanol)

*(Pdw = by powder dry weight)

MR70 (Albemarle) has a larger particle size and wide size distribution and TM-DAR (Taimei Chemicals) has smaller size and narrow size distribution. It is clear in the above TM-DAR case; the slip will not be fully stable. Colloidal processing of TM-DAR $\alpha - Al_2O_3$ was studied by Michálková et al. and they found that above 40 % of solid loading the slip remains partly flocculated [32]. In the preliminary studies high solid content of TM-DAR was chosen to reduce the cast filtration time but nevertheless partly flocculated slip will still yield sintered objects with a density of >98 % of theoretical density (T.D.) [18]. 98 % T.D. is the density boundary above which the ceramic is commonly defined as a fully dense ceramic. Typically when using nanopowders such as TM-DAR, there is no need for binder or plasticizer addition because the packing density and therefore green strength is better and handling easier. Sintering of different Al_2O_3 powders is reviewed in chapter 3.5.

Processing or comminution of the slip is done by simple shear blade mixing, mechanical milling or by ultrasonic cavitation (For more information see ref. 27). The raw materials are mixed together in sequence and then the mixture is aged while mixing to remove heterogeneity from the slip. When slip is milled or mixed the goal is not anymore to reduce the particle size but to remove agglomerates and flocs which reduce quality of the green cast. After sufficient stability and viscosity is reached the slip can be poured in to the mould. Bubble formation needs to be prevented during the mixing process to prevent flaws in the green compact.

More practical information on slip casting can be found in various review and experimental papers, such as the Master thesis of Jussi Silvonen [33]. Although a good theory exists, the most part of slip casting is learned by practical work. Often there is a lack of analytical equipment to optimize the slip before you try it by yourself and most often it is also the fastest way. Slip doesn't have to be perfect in order for slip casting to work. But when it goes wrong it is good to know what parameters you can change in order to get it working.

3.4   Drying and debinding of green compacts

There are a number of steps in the ceramic processing that can go wrong, and a failure in any of steps will lead to useless products. One of most critical step is the drying phase, where the just casted green compacts are taken out from the mould to dry out. Instantly as the vapour/liquid interface is created the capillary forces start working to shrink the solid as the liquid is removed. A powerful example of the capillary forces can be seen with aerogel, which is SiO_2 solid that has very low density because of extremely high pore concentration. When exposed to liquid, capillary forces will instantly destroy the aerogel block by compressing and warping it.

Different cases of drying warpage are illustrated in figure 3.6. When capillary force is at work inside the green compact, the main aspect is how uniform is the amount and removal of water from the green body.
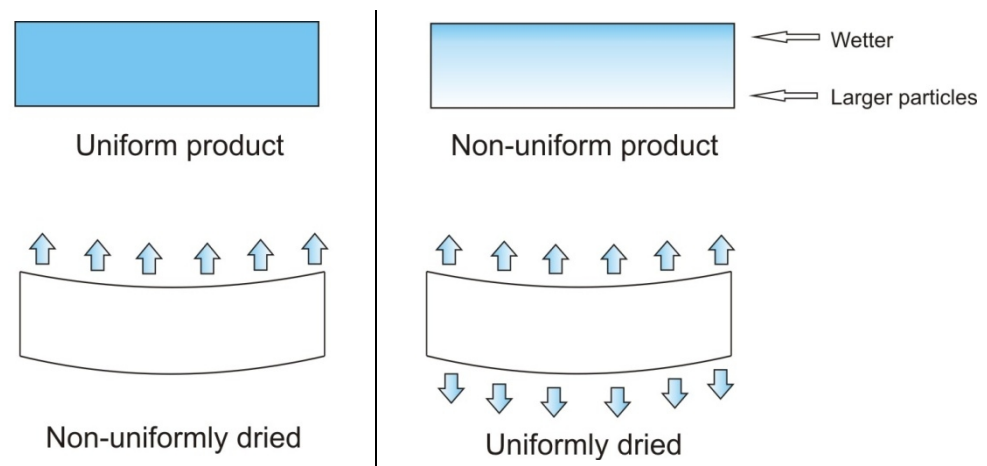
Figure 3.6: *Warping in slip casted green compacts. [27, 28]*

Both internal and external conditions can have a damaging effect. Internal effects include uneven distribution of water inside the compact and uneven distribution of larger and smaller particles caused for example by sedimentation during casting. Non-uniform pressure gradient or non-uniform drying caused by external conditions will also lead to undesirable changes to the object geometry. [28]

Preliminary studies of this thesis indicated that closed moulds should be used to minimize warping caused by non-uniformities in the cast. But if closed moulds are used it should be noted that closed mould can also produce significant porosity to the centre line of the cast, which can reduce bending strength of the solid.

Debinding simply means removal of all organic additives used in the processing of the ceramic powder prior to sintering. Before debinding, the green compact must be fully dry to avoid damaging the compact. Organic additives are removed by burning or vaporizing them using heat, usually 1 hour at 600 ˚C in normal atmosphere removes most organic additives. Heating rate should be kept low to prevent internal gas pressure build up. The debinding can often be simply programmed as a pre-sintering stage in the furnace controller. Inorganic additives are harder to fully remove and thus their use should be considered according to the application of the final product. During sintering, formation of a glassy phase is possible if there is inorganic alkali elements (Na, K) and SiO_2 present in the material.

3.5   Sintering oxide, non-oxide and composite materials

Last step in the process is to sinter the green compact into a dense ceramic product. Word 'sintering' refers to the densification and shrinking of the compact that happens in high temperature specific to certain type of material or powder. Main driving force for densification is the free surface energy of material. The amount of driving force of the material determines the external energy or activation energy (heat) needed for eliminating surface area (porosity) and to produce a dense bulk product. External pressure and glassy grain boundary phases can be used to lower the activation energy needed for sintering. [27]

We can define the free surface energy as the excess energy that is bound to the surface of material compared to the bulk. With smaller particle size (e.g. nanoparticles) this energy can substantially lower the activation energy needed for the sintering process to begin. According to sintering theories, another key parameter for affecting densification is the packing density of particles in the green product. [27]

3.5.1   Sintering kinetics

There are two main processes happening during sintering: Densification (pore volume reduction) and coarsening (grain and pore growth). The existing theory looks these two processes separately and with simplified models because of the high complexity present in the real situation. When aiming to achieve the best mechanical properties for a ceramic, full density and fine grain structure are desirable and therefore understanding the sintering process gives us the opportunity to lessen the work load of trial and error method. At least six mechanisms control the densification and coarsening as shown in figure 3.7a.

a)   b)
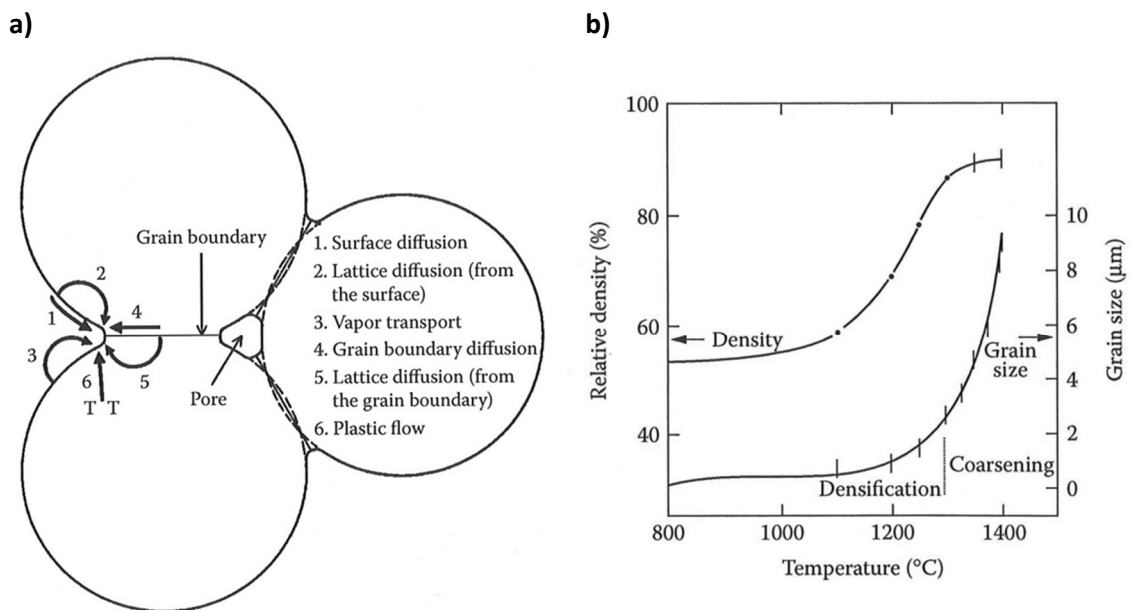
*Figure 3.7: **a**) Three particle system illustrating mechanisms for densification (4, 5 and 6) and grain growth (1, 2 and 3) and **b**) densification and grain growth of a TiO_2 powder compact as a function of sintering temperature. [27]*

Mechanisms 1, 2 and 3 are responsible for the coarsening, which refers to grain growth and pore growth and 4, 5 and 6 for the densification. Figure 3.7b illustrates the a sintering process of TiO_2, where first the densification mechanisms dominate to about 1300 ˚C or to relative

density of 0.86 and after that mechanisms leading to coarsening dominate. Review of Zeng et al. [34] summarize the sintering kinetics of $\alpha - Al_2O_3$ micro and nanopowder. Initial sintering is controlled by grain boundary diffusion and the sintering or densification kinetics in $\alpha - Al_2O_3$ are dominant to a relative density of 0.77, after which the coarsening kinetics dominate. This will in theory give possibility to control grain growth by using fast sintering cycles, where the dwell time in coarsening domain temperatures is short. Also if activation energy of sintering (sintering temperature) can be lowered with for example doping or by external pressure, grain growth could be controlled further. [27, 34]

Effects of particle size and particle packing on the sintering of different ceramic materials are shown in figure 3.8. Figure 3.8a illustrates that for powders with small particle size and therefore a large driving force, the sintering happens in much lower temperatures than for powder with large particle size. Figure 3.8b show that densification rate is also closely related to the initial particle packing density in the green compact

a)   b)
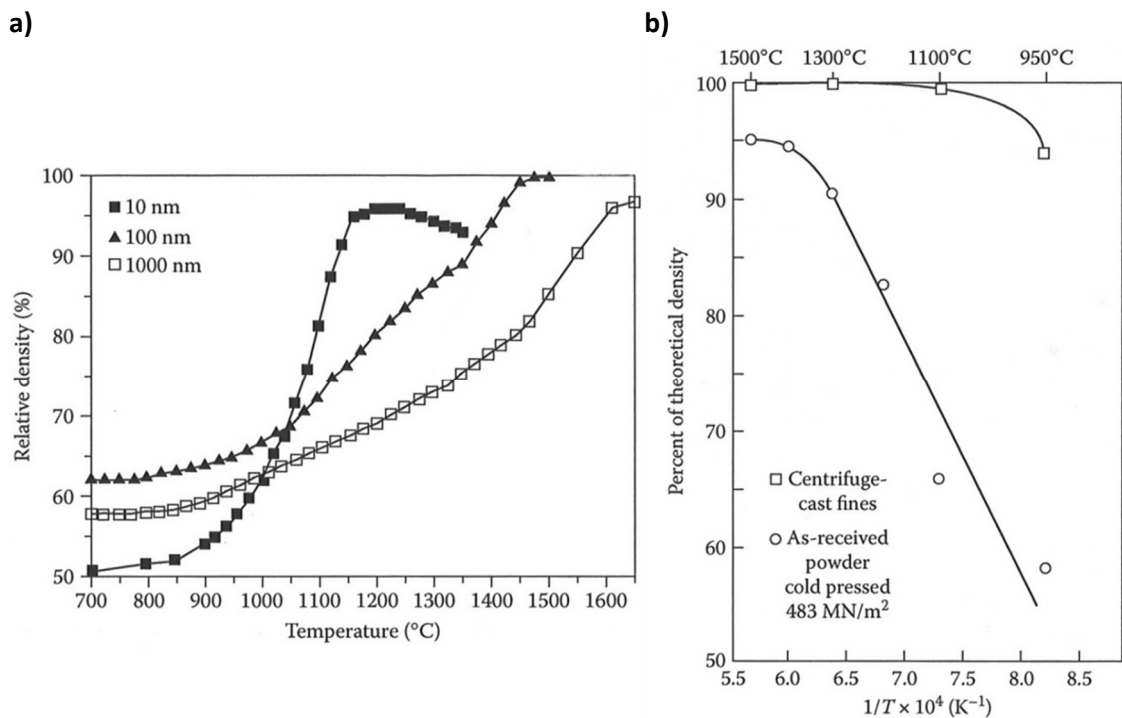
Figure 3.8: a) *Effect of particle size on the sintering of* CeO_2 *powder compacts and* *b)* *the effect of particle packing on the sintering of* Y_2O_3*-stabilized* ZrO_2*powder compacts after 1 h in various temperatures with (□) higher green density and (○) lower green density. [27]*

Zeng et al. [34] show that the Herring scaling law can be used succesfully to estimate the final sintering temperature of different $\alpha - Al_2O_3$ powders. Calculated values in figure 3.9 predict the final sintering temperature of $\alpha - Al_2O_3$ powders with different sub micrometer particle sizes to obtain 95 % theoretical density. Figure 3.9 also shows sintering temperature values calculated for MgO doped $\alpha - Al_2O_3$ which has lower activation energy for sintering. According to Zeng et al. the calculated values agree well with the experimental data collected from different sources. Data in figure 3.9 with previously presented theory clearly indicate that lower particle size will lower the sintering temperature. The calculations also predict that sufficiently small $\alpha - Al_2O_3$ particles could be sintered at temperatures below 1000 °. [34]
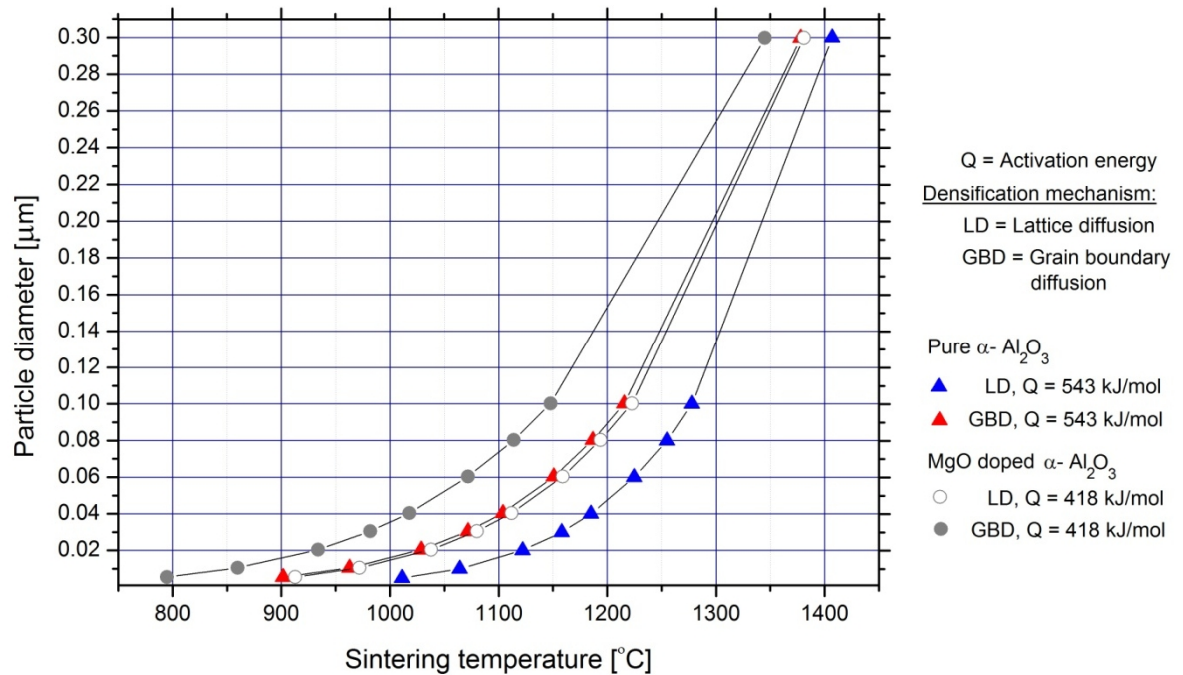
Figure 3.9: *Particle diameter of $\alpha - Al_2O_3$ as a function sintering temperature estimated by Herring's scaling law. Assuming that 0.6 µm diameter Al_2O_3 is sintered to 95% theoretical density at 1500 ˚C and activation energies are 418 and 543 kJ/mol for magnesia doped and pure $\alpha - Al_2O_3$ respectively. [34]*

Sintering of the two $\alpha - Al_2O_3$ powders presented in chapter 3.3.2 underline the theory discussed above. Experimental values for final sintering temperature of slip casted samples are reported by the suppliers to be 1650 ˚C for MR70 (D_{50} = 0.5 - 0.8 µm) and 1300 ˚C for TM-DAR (D_{50} = 0.2 µm), only major difference being the average particle size of the powders.

### 3.5.2   Effect of dopants and inert second phase particles

In ceramic nanocomposites the second phase material determines much of the sintering properties of the composite material. Often the matrix material is selected only after the second phase material and its desired particle size. This is simply because metallic particles have intrinsically low melting points, which determine the upper temperature limit for sintering. This is of course only if liquid state sintering is not desired. Effects of second phase materials are discussed next briefly.

Sinterability of $\alpha - Al_2O_3$ can be enhanced by using dopands. Dopants such as MgO in $\alpha - Al_2O_3$ matrix (Coble [35]), lower sintering temperature and can inhibit grain growth by mechanism of solute drag. Second phase particles that do not react with alumina (Ni, $ZrO_2, SiC\ etc$.) on the other hand can slow down grain growth as first proposed by Zener [27], introducing a 'pinning' effect on the grain boundary. As the grain boundary comes in contact with the inert particle, extra work must be done by the grain boundary to overcome the obstacle and without the extra energy further boundary migration is prevented. The inert particles will also inhibit densification which leads to increased sintering temperature in for example $Al_2O_3 - SiC$ nanocomposites. [5, 27, 35, 36]

3.5.3   Pulsed electric current sintering (PECS)

Advanced ceramic and nanocomposite materials have certain demands for the atmosphere where the sintering is conducted. Metallic particles or non-oxide ceramics (Carbides, Nitrides etc.) tend to corrode, decompose or oxidise in temperatures well below the sintering temperature if oxygen is present. Therefore special sintering methods and conditions are needed, such as vacuum sintering or protective gas sintering.

For this study, pulsed electric current sintering (PECS) or also known as spark plasma sintering (SPS) technique was selected for the densification of samples. Main benefits are high heating rates obtained by introduction of electrical current through the sample and possibility to simultaneously apply pressure on to the specimen powder or green specimen. Figure 3.10 presents schematically the main components of a PECS device. Specimen is placed in a graphite mould and pressed against two graphite punches using a hydraulic piston. Device operates in vacuum or in inert/reducing gas because the graphite mould will burn if oxygen is present. Graphite is used because it is a conductor and withstands very high temperatures in vacuum conditions. [18]
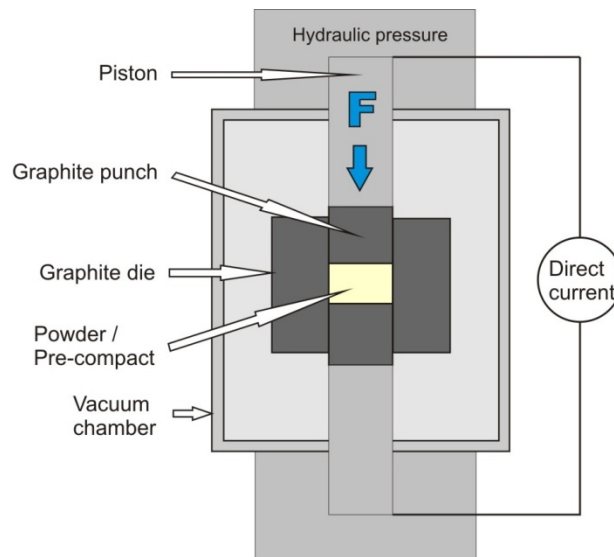

Figure 3.10: *Schematic presentation of pulsed electric current sintering (PECS) device.*

Heating rate can be up to 500 ˚C/min and pressure, depending upon the area of the sample, 50 - 75 MPa [27]. Simultaneous pressure lowers the activation energy of sintering which lowers the sintering temperature and therefore allows good control over grain growth. Preliminary studies of this thesis show that for TM-DAR type of $\alpha - Al_2O_3$ powder the final sintering temperature is approximately 100 ˚C lower than using a conventional pressureless sintering method. Preliminary studies also show clearly that sintering using PECS is fast, sintering a 20 mm $\alpha - Al_2O_3$ (TM-DAR) disk takes approximately 30 min including the cooling stage. Fast procedure further lowers the grain growth by lowering the dwell time in grain growth temperature domain. Downsize of this technique is that the product geometry is often limited to a simple cylinder shape and the maximum diameter is limited (approximately 10 - 100 mm). There is at the moment (in 2012) one PECS device in Finland which is located in the department of materials science and engineering at Aalto University.

3.6   Challenges in processing of ceramic nanocomposites

With nanopowders, processing flaws at the present can only be controlled to a certain limit and it is necessary to ponder whether optimal nanocomposite structures can ever be achieved with dry ceramic processing routes, e.g. dry milling or mechanical mixing. That is why wet colloidal methods are typically used to process submicron powders [27].

A typical nanocomposite microstructure is most likely to be either pure inter-type or intra/inter-type structure. Also mostly intra -type structures are possible with special processing methods [6, 21]. Typical processing flaws are caused by dry processing are illustrated in figure 3.11. Agglomerated nanoparticles have been detected to cause voids/large pores in the microstructure [7]. Voids act as stress concentrators, and it is again the most fundamental to point out, that agglomerated nanoparticles have lost any internal properties they may have had in terms of their original size.

a)   **b)**
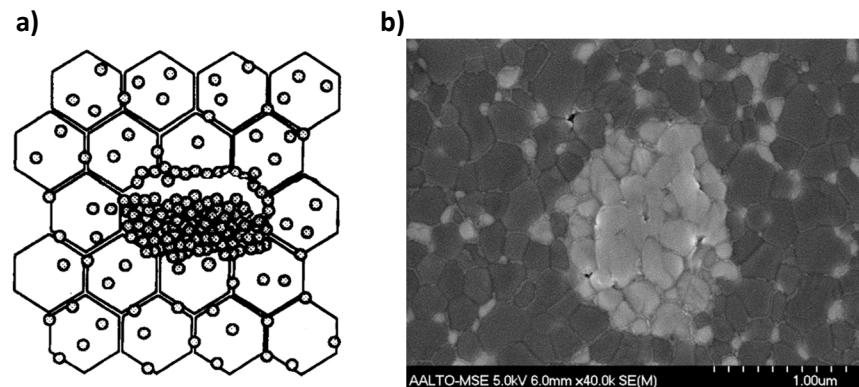
Figure 3.11: **a)** Schematic illustration of a typical processing flaw in mechanically mixed $Al_2O_3 - SiC$ nanocomposite structure [7] and **b)** SEM image of the agglomeration of ZrO_2 nanoparticles caused by dry mechanical mixing in $Al_2O_3 - ZrO_2$ nanocomposite [18].
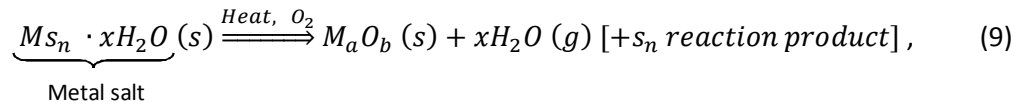
Because breaking ever finer agglomerates requires more processing time or higher milling energy, contamination in both dry and wet methods become a big problem. None of the present deagglomeration processes are contaminant free. As the single contaminant can be, in the nanocomposites case, up 10 or 20 times larger than the average particle size they will have a large impact on dispersion and sinterability. In the next chapter we will explore thermolysis as processing route to synthesize ceramic nanocomposites which.

3.7   Synthesis of ceramic nanocomposite powder

Mixing two separate powders is not always plausible method to produce a composite for reasons discussed in the last chapter. One option is to grow nanoparticles during the process and that way remove unnecessary milling of agglomerates and avoiding related problems. Next we introduce thermolysis as a potent synthesis method for ceramic nanocomposites.

Thermal decomposition or thermolysis is a simple thermochemical procedure where energy is fed into a chemical system which undergoes degradation, or in other words, a chemical decomposes into its element components when heat is applied. Thermolysis can be used to produce ceramic nanocomposites by growing the second phase nanoparticles in the surface of the ceramic matrix particles [3, 37]. In this procedure only the second phase substances undergo decomposition and the matrix is left to original state. Several different metal salts can be used to produce desired substance with desired particle size including nitrates, chlorides, acetates and sulphides [37]. To prevent contamination, the anions should

preferably generate gas during decomposition; also anions should not react while in the solution. Thermal decomposition of metal salt in oxidizing atmosphere can be generally presented as

$$\underbrace{Ms_n \cdot xH_2O}_{\text{Metal salt}} (s) \xrightarrow{Heat,\ O_2} M_aO_b\ (s) + xH_2O\ (g)\ [+s_n\ reaction\ product]\ , \qquad (9)$$

where x is a multiplier, M is a metal ion or salt cation (Ni^{+2}, Fe^{+2} etc.) and s_n is a salt anion (CH_3COO^-, Cl^-, NO_3^- etc.). To obtain metallic particles, the metal oxide particles need to be heat treated again using a reducing gas (such as hydrogen). Reducing phase of the synthesis can be generally presented as

$$M_xO_y\ (s) \xrightarrow{Heat,\ H_2} M\ (s) + xH_2O\ (g)\ . \qquad (10)$$

Also other reducing agents could be used, such as carbon monoxide (CO). End product would then be carbon dioxide (CO_2) instead of water.

Advantage of growing the second phase particles is that excellent dispersion can be achieved only by controlling matrix particle dispersion, since second phase are chemically bonded to the matrix particles after thermolysis [37]. Second advantage is a very small initial particle size of the second phase particles [3, 9, 37]. In the experimental part we use thermolysis to synthesize $Al_2O_3 - Ni$ nanocomposite powder.

4. Fabrication and characterization of Al$_2$O$_3$ - Ni nanocomposites

In the course of experimental part of this thesis, we demonstrate fabrication of $Al_2O_3 - Ni$ nanocomposites. This chapter lists used materials, processing methods for the nanocomposite material and the test methods that were used to characterize of the produced samples.

4.1 Starting materials and powder characterization methods

Aluminium oxide powder of choice was Taimicron TM-DAR (Taimei chemicals CO., Ltd, Japan >99.99 % $\alpha - Al_2O_3$) with d$_{50}$ = 0.2 μm and specific surface area of 14.5 m^2/g. Nano-sized nickel was used as a second phase material. Nickel particles were synthesized from nickel (II) nitrate hexahydrate ($N_2NiO_6 \cdot 6H_2O$) by thermal decomposition to NiO and sequel reduction to metallic Ni. Raw Al_2O_3 was analysed using a scanning electron microscope (SEM) and synthesized $Al_2O_3 - NiO$ powder was analysed using a transmission electron microscope (TEM) and electron dispersive spectroscopy (EDS).

4.2 Powder synthesis and processing

$Al_2O_3 - Ni$ (2.5 vol. %) nanocomposite powder synthesis was done using thermal decomposition of metal salts with accordance to the work done earlier by Moya et al. [3]. First the Al_2O_3 powder was mixed with solution of alcohol and nickel (II) nitrate hexahydrate that was measured to yield 2.5 vol. % of nickel in the final $Al_2O_3 - Ni$ nanocomposite. Mixture was milled in planetary ball mill (Pulverizette 5, Fritsch GmbH.) for 5 h with Al_2O_3 balls with a speed of 140 rpm. Ratio of balls and slip was selected by the recommendation of equipment manufacturer. Milled mixture was then dried in a convection oven at a temperature of $100 - 120$ ˚C for 6 hours. Dried powder was crushed in a mortar and was then heat treated at 400 ˚C in air for 2 hours to thermally decompose the nickel nitrate salt into NiO. $Al_2O_3 - NiO$ mixture was then heat treated at 500 ˚C in Ar/H_2 5% atmosphere for 2 hours to reduce the nickel oxide into metallic nickel.

Following reactions occur in the synthesis of Al_2O_3/Ni powder by thermolysis:

$$2N_2NiO_6 \cdot 12H_2O\ (s) \xrightarrow{Heat,\ O_2} 2NiO\ (s) + 4NO_2(g) + O_2(g) + 12H_2O\ (g) \quad (11)$$
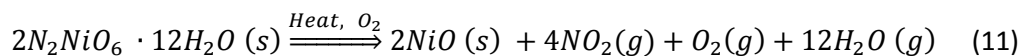
Nickel nitrate (II) hexahydrate decomposes into nickel oxide, gaseous nitrogen dioxide (red-brown fume) and water vapour [38, 39]. If excess water vapour is present, nitric acid could form [38], which endorses the use of other processing solvents such as ethanol. Nitrogen oxides (NO_x) are pollutes found in many industrial processes and for example in the exhaust gas of cars. NiO was further reduced into metallic nickel by following reaction:

$$NiO\ (s) \xrightarrow{Heat,\ H_2} Ni\ (s) + H_2O\ (g) \qquad\qquad (12)$$
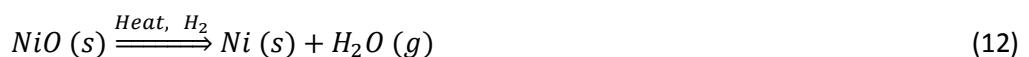
Presence of metallic nickel was verified in XRD studies and the results are presented in next chapter.

4.3   Forming, drying, debinding and sintering of $Al_2O_3 - Ni$ nanocomposite samples

Samples were formed from $Al_2O_3 - Ni$ powder by slip casting. Pure Al_2O_3 samples were prepared as a reference. Slip was filtrated into green compacts in porous gypsum moulds. Slip casting materials and additives are listed in table 4.1.

Table 4.1: *Slip casting materials and additives*

$Al_2O_3 - Ni$ powder	70.0 wt.%
H_2O (ion exchanged)	30.0 wt.%
Darvan C-N (PMMA)	2.2 wt.% (of powder dry weight)
Surface tension modifier (Alcohol, Agitan™ ,etc.)	0,5 ml

To prepare the slip, ion exchanged water and dispersing agent (Darvan C-N [PMMA]) were mixed with a shear blade mixer. Nanocomposite powder was mixed with the solution and then milled with 140 rpm in planetary ball mill (Fritsch pulverisette 5) for 60 min with 15 mm Al_2O_3 balls and with ball/slip ratio recommended by equipment manufacturer. Alcohol was added before milling to remove air bubbles from the slip. After milling the powder is still partly agglomerated and sedimentation was observed in the standing slip. Directly after milling the slip was poured into a cylindrical mould with diameter of 11 cm. After approximately 2 hours of filtration the compacted sample was released from the mould to dry in room temperature for 24 hours. Next the compact was dried in convection oven, first in 60 ˚C for 24 hours and second in 90 ˚C for 24 hours. Cylindrical samples with a diameter of 20 mm and thickness of 5 mm where cut from the precompact. Before sintering the green compacts were debinded at 600 ˚C for 1h in argon atmosphere to remove all additives. Reference samples were slip casted with the same parameters but using pure Al_2O_3 powder.

Sintering was conducted at Aalto University in Helsinki, using a pulsed electric current sintering (PECS) or also known as spark plasma sintering (SPS) device model FCT - HPD25-2 by FCT Systeme GmbH. A photograph of a sintered $Al_2O_3 - Ni$ sample is shown figure 4.1.

Figure 4.1: *Photograph of a $Al_2O_3 - Ni$ sample sintered with PECS.*

In sintering phase, $Al_2O_3 - Ni$ samples were heated from room temperature to 1100 ˚C at a rate of 200 ˚C/min, then to 1200 ˚C at a rate of 100 ˚C/min and finally to 1225 ˚C at a rate of 50 ˚C/min with a pressure of 76 MPa. Pressure was initially 16 MPa at a temperature of 500˚C and was risen ≈ 12 MPa/min until ultimate pressure was reached. The final temperature and pressure where maintained for 5 min. Reference Al_2O_3 samples were sintered using the same parameters, although it is likely that the sintering happened in lower temperature compared to $Al_2O_3 - Ni$ samples. All sintering cycles were conducted in vacuum atmosphere. Sintered samples had a diameter of approximately 20 mm (diameter of precompact grows during pressing in PECS, so it appears that almost no shrinkage has happened) and thickness of 2-3 mm.

4.4 Material characterization methods

4.4.1 Density, composition and microstucture

Densities of the sintered samples were measured with Archimedean method using deionised water as penetrant. Phase composition of Al_2O_3, $Al_2O_3 - NiO$ and $Al_2O_3 - Ni$ powders and sintered Al_2O_3 and $Al_2O_3 - Ni$ samples were studied with X-ray diffraction method (XRD), using a Siemens D-500 X-ray diffractometer.

Transmission electron microscope (Jeol JEM 2010) was used to analyse the morphology of $Al_2O_3 - NiO$ powder and the size of synthesized NiO particles. Scanning electron microscopes (Philips XL-30 and Zeiss ULTRAplus Ultra High Resolution FEG-SEM) were used to analyse raw Al_2O_3 powder and take cross-section images and fractured surface images of sintered $Al_2O_3 - Ni$ and Al_2O_3 reference samples. Cross-section images where polished down to fineness of 1 µm before imaging. Fractured surfaces where produced with a hammer blow fracturing the sample in half. Samples for SEM imaging were coated in carbon evaporator.

Grain sizes were measured from the cross-section and fractured surface SEM images, using an image analysis program (Image Tool). Minimum of 50 grains were measured per sample.

4.4.2 Mechanical testing

Vickers hardness (H$_V$) of the samples was measured according to European standard EN 843-4, with microindentation devices Matsuzawa MMT-X7 and Struers Duramin A300. Measurements were taken from a polished surface (1 µm fineness) with a load of 1.98 N, 9.8 N and 98 N and indentation dwell time of 10 seconds. Hardness was tested with different loadings to study if the possible hardening was a related only to the surface of material. Vickers hardness was from average of 10 test results calculated with the following equation

$$H_v = 1.854\ P/d^2, \tag{13}$$

where H_v is the Vickers hardness, P is the applied load [N] and d is the mean of two diagonal lengths of the indentation [mm]. Fracture toughness was determined using indentation fracture method (IF) according to European standard CEN/TS 14425-1. In this method the fracture toughness is evaluated from the relationship between the length of median crack and the diagonal length of the indentation made into a polished surface. Indentations were made using Struers Duramin A300 microindentation device with a load of 98 N and dwell time of 10

s. Fracture toughness was calculated from average of 10 test results using equation for median crack system provided by Niihara [40]

$$K_{IC} = 0{,}129 \left(\frac{c}{a}\right)^{-3/2} \left(\frac{E\phi}{H}\right)^{2/5} \left(\frac{Ha^{1/2}}{\phi}\right) \text{ for c/a} \geq 2.5, \tag{14}$$

where K_{IC} is the fracture toughness (MPa $m^{1/2}$), c is the median crack length (m), a is the diagonal half-length of the indentation (m), E is the Young's modulus of the tested material (MPa), ϕ is a constant ≈ 3 and H is the hardness of the tested material (MPa). Young's modulus of composite material was evaluated using the rule of mixtures (E was 380 GPa for Al_2O_3 and 200 GPa for Ni). Red indicator paint was applied before measuring the crack lengths. Crack lengths were determined from optical microscope images using image processing software (Image Tool). Figure 4.2 presents schematically the cross sectional geometry of different indentation crack systems.
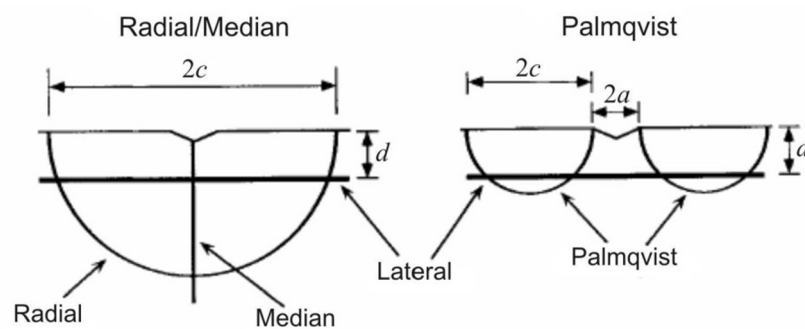

Figure 4.2: *Principal indentation crack system geometries [41]*

5. Analysis of fabrication method and test results

In this section we summarize and discuss the main results and evidence concerning powder synthesis, powder processing and sintering, physical properties, microstructure and mechanical properties of the nanocomposite and reference samples. Also we review a geometrical model predicting metal nanoparticle growth in ceramic/metal nanocomposites during sintering.

## 5.1 Thermolysis of Al_2O_3 – Ni nanocomposite powder

Figure 5.1 shows schematically the steps leading to nanoparticle formation.
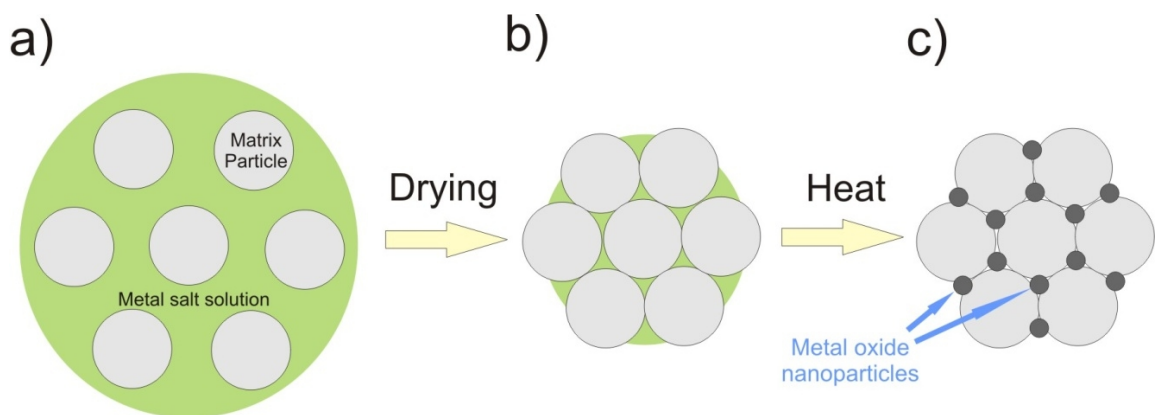
*Figure 5.1: Shcematical illustration of producing nanocomposite powders by thermal decomposition, **a)** deagglomerated powder in metal salt solution, **b)** during drying the matrix particles are pushed together by capillary forces and form an orderly packed clusters and metal salt crystallizes on the contact points of matrix particles. Finally the powder is **c)** heat treated in air to produce metal oxide nanoparticles.*

First the salt is fully dissolved in a liquid which is mixed with the ceramic matrix powder. Mixture is then milled or ultrasonically cavitated to break any powder agglomerates so that the metallic salt solution surrounds all the particles. Deagglomerated powder is then dried in a convection oven where the metal salt crystallizes between particles and the powder is then crushed mechanically. Crushed powder is heat treated to thermally decompose the metallic salt in to metal oxide nanoparticles. Afterwards the nanoparticles can be reduced to metallic using heat and reducing gas ($H_2 \ etc.$). Figure 5.1 gives a very rough illustration on thermolysi0s process. Better illustration shown in figure 5.2 given by Rodriguez-Suarez et al. [42] who proposed a qualitative model concerning the thermolysis process.

Figure 5.1 and 5.2 give a basic idea that thermolysis and sequential sintering induces certain geometrical boundary conditions that in ideal situation can be used to predict the size of the smallest possible metal oxide nanoparticles. In the next chapter a quantitative geometrical model concerning growth of metal nanoparticles proposed by Kannisto et al. [43] is reviewed.
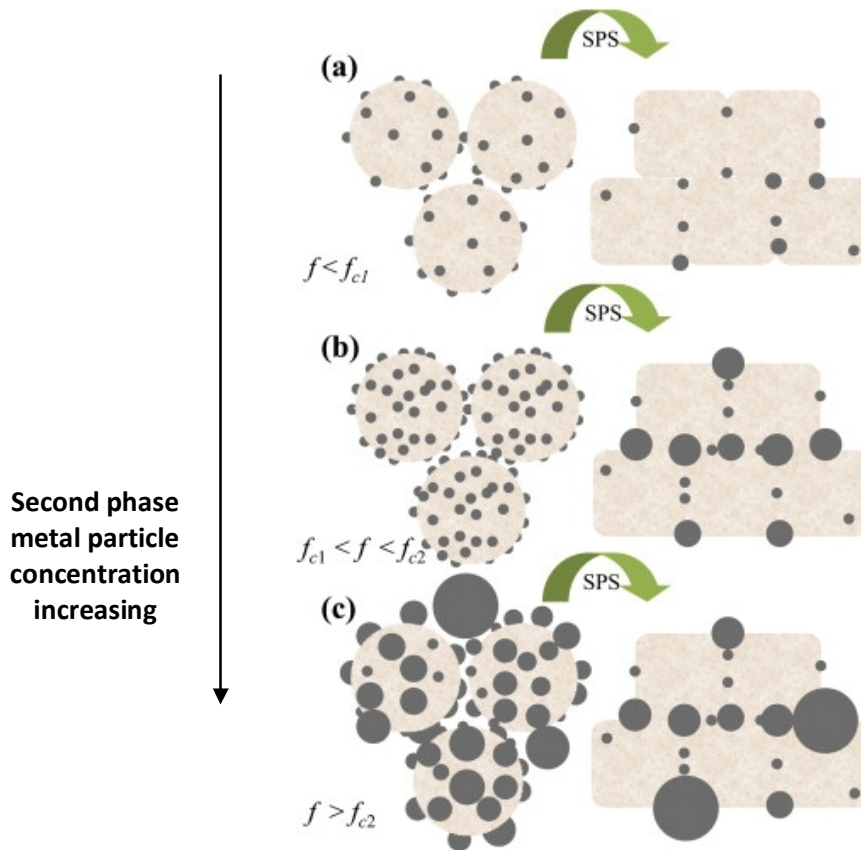
Figure 5.2: *Qualitative geometrical model for synthesis and sequential spark plasma sintering (SPS) of ceramic/metal nanocomposites: **a)** below the aggregation threshold of second phase metal particles, **b)** between the aggregation and percolation threshold and **c)** over the percolation threshold. [42]*

5.2 Geometrical model to predict the metal nanoparticle growth during sintering

Based on microstructural studies of $Al_2O_3 - Ni$ nanocomposites and literature data on $Al_2O_3 - Ni$, Kannisto et al. [43] proposed a geometrical limit for the Ni nanoparticle growth. They proposed that in ceramic/metal nanocomposites near the percolation threshold, matrix particle grain growth during sintering determines also the growth of second phase metal nanoparticles. They adapted basic geometrical models of ceramic crystal structures and found similar geometrical boundary condition in ceramic/metal nanocomposites. Kannisto et al. proposed that metal nanoparticles with coordination numbers 3 and 4 (corresponding to number of ceramic matrix particles surrounding the metal particle) give a set of geometrical boundary conditions which can be used to predict the grain growth of nickel particles. The geometrical boundary conditions of metal nanoparticles with coordination number 3 is schematically presented in figure 5.3
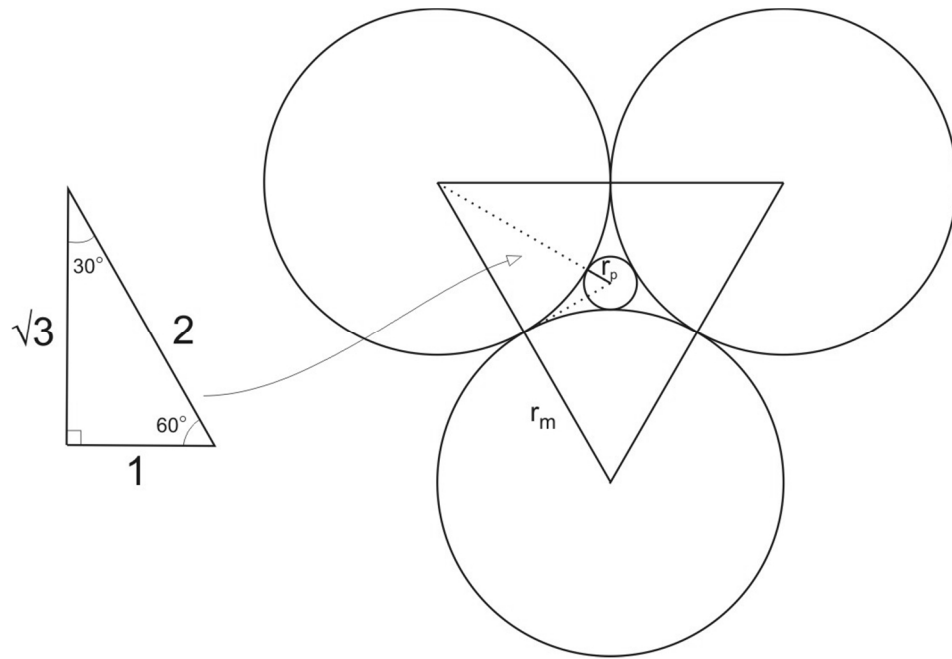
Figure 5.3: *The optimal boundary conditions set by the size of matrix particles (r_m), for the 2-dimensional geometrical size limit of nanoparticles (r_p) during sintering. [43]*

Using these boundary conditions we can write $r_m + r_p = 2$ and that $r_m = \sqrt{3}$. Using these terms we can calculate ratio r_p/r_m, which yields

$$r_p = r_m(2 - \sqrt{3})(1/\sqrt{3}) \ , \tag{15}$$

Presuming that the radius of matrix particle (r_m) is known, radius of the nanoparticle can be calculated with the equation (15), or with an approximation

$$r_p \approx 0.155 \, r_m \quad , \tag{16}$$

where r_p (nm) is the radius of the nanoparticle and r_m (nm) is the radius of the matrix particle. Using the equation (16) for matrix particles with a diameter of 700 nm the size of metal nanoparticles will be approximately 108 nm, which is well in line with the observations (see table 5.3). With coordination number 2, the size of the second particles would theoretically be $< 0{,}155 \, r_m$, although it is very unlikely that these are found in real microstructures, due to interaction forces between particles. [43]

Second phase particles residing in triple junctions (tetrahedral sites) will correlate to geometrical model with coordination number 4 shown in figure 5.4. Geometrical boundary conditions for this coordination number can be schematically presented as
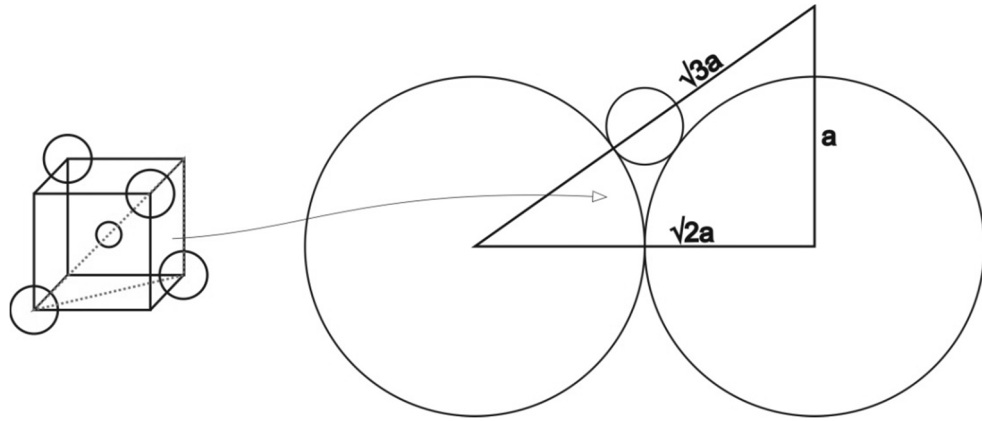
Figure 5.4: *Geometrical boundary conditions for 3-dimensional particle model with nanoparticle coordination number 4. [43]*

Using these boundary conditions (Figure 5.4), we can write $a = 2r_m/\sqrt{2}$, by which the body diagonal $b = \sqrt{3}a = \sqrt{6}r_m$. When we also know that body diagonal $b = 2(r_m + r_p)$, we can make a proportion

$$\sqrt{6}r_m = 2(r_m + r_p)\,, \tag{17}$$

which yields

$$r_p = r_m\left[(\sqrt{6}-2)/2\right], \tag{18}$$

when the matrix particle radius is known, second phase particle size can be calculated using equation (18) or by using an approximation

$$r_p = 0.225\, r_m\,. \tag{19}$$

Coordination numbers 6 and 8 are also possible particle arrangements but again are not found in real microstructures. [43]

Since the geometrical model doesn't take into account the phase changes or removal of gas during thermal decomposition, it can be only used to evaluate the lower size limit of the nanoparticles produced by thermal decomposition. For $Al_2O_3 - Ni$ nanocomposites the percolation threshold concentration has been measured to be approximately 2.5 vol. % of nickel [3]. Calculating optimal packing volumes for these coordination systems it should yield a value in close proximity to the percolation threshold.

In optimal dispersion of matrix and second phase particles, model predicts final metal nanoparticle size after sintering. Table 5.1 reviews particle size measurement results of sintered $Al_2O_3 - Ni$ nanocomposites. Table reveals that measured values correspond well to values predicted by the quantitative geometrical model. But it is still unclear which coordination number gives the best prediction for different matrix grain sizes and why this happens. [43]

Table 5.1: Matrix particle sizes and nickel nanoparticle sizes of sintered $Al_2O_3 - Ni$ 2.5 vol. % nanocomposite samples compared to values predicted by the geometrical model. [43]

Reference	Processing method	Sintering method	Al_2O_3 (measured)	Ni (measured)	Ni (CN 3 – CN 4)
Moya et al. [3]	-	PECS	300 ± 50 nm	< 60 nm	$47 - 67$ nm
Rodrigues-Suarez et al. [4]	Isostatic pressing	CS	800 ± 200 nm	110 ± 36 nm	$123 - 180$ nm
Rodrigues-Suarez et al.[4]	-	PECS	250 ± 100 nm	50 ± 18 nm	$39 - 56$ nm
Kannisto et al. [18]	Slip casting	PECS	660 ± 160 nm	110 ± 37 nm	$102 - 149$ nm

If sintering is happening below metal melting temperature, coalescence is most likely to be the most significant mass transfer phenomena and grain growth will be limited by the matrix geometry. As results also indicate, all the second phase nanoparticles are located in the grain boundaries and most often in triple junctions which is in favour of the geometrical model. Results in Table 5.1 also indicate that the growth is independent of sintering method if sintering temperature is below the melting temperature of metal nanoparticles.

5.3 Phase composition: Powders and sintered samples

X-ray diffraction diagrams of test materials are shown in figure 5.5. Results confirm that only metallic Ni and $\alpha - Al_2O_3$ are present after reduction phase of the powder processing and that no significant oxidation or phase changes of Ni happened during sintering of $Al_2O_3 - Ni$ nanocomposite. There is a possibility, that without careful processing steps, substantial amount of NiO is left in the material after powder processing. In normal atmosphere, the NiO can further react with $\alpha - Al_2O_3$ to produce nickel aluminate ($NiAl_2O_4$) spinel with a distinct blue color.
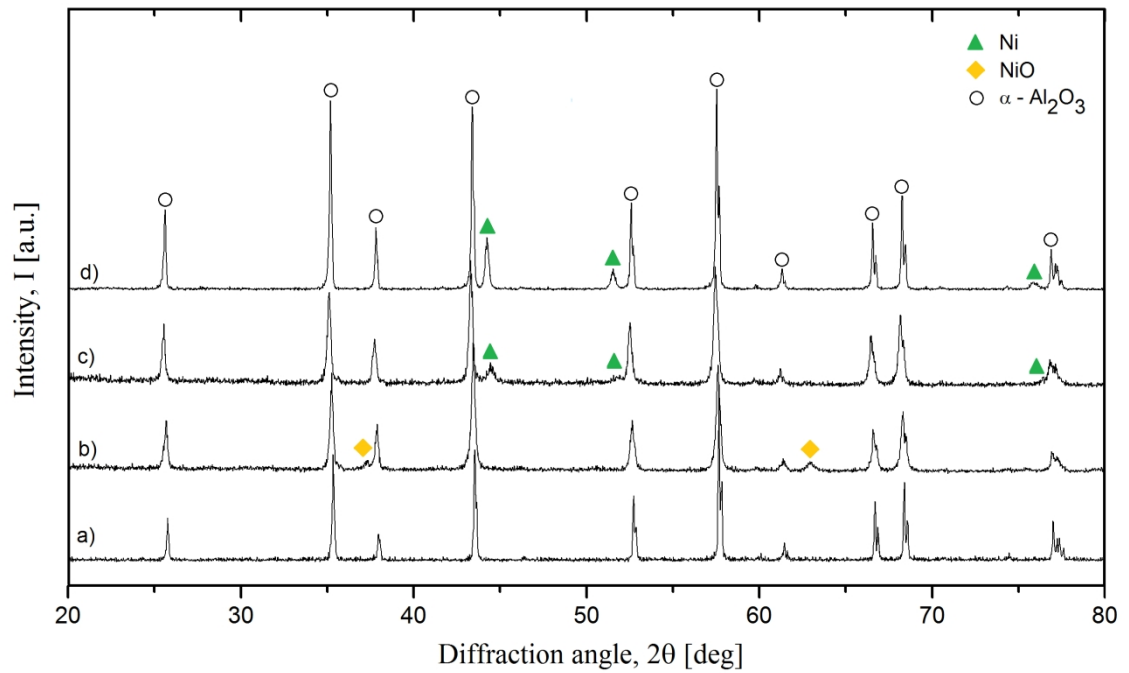

Figure 5.5: *X-ray diffraction diagrams corresponding to **a)** sintered Al_2O_3 reference, **b)** $Al_2O_3 - NiO$ 2.5 vol. % powder, **c)** $Al_2O_3 - Ni$ 2.5 vol. % powder and **(d)** sintered $Al_2O_3 - Ni$ 2.5 vol. % nanocomposite.*

It has been shown that no $NiAl_2O_4$ spinel can be left after sintering if temperature is above 1300 ˚C because the spinel decomposes to Al_2O_3 and Ni. It is unclear however if this transition happens only in reducing atmosphere such as in carbon bed used in previous study. [44]

## 5.4   Properties of as received and synthesized powders

SEM micrographs of the pure $\alpha - Al_2O_3$ (TM-DAR) powder in figure 5.6 show irregular soft agglomerates with near uniformly shaped and sized primary particles with an average particle size of approximately 200 nm.
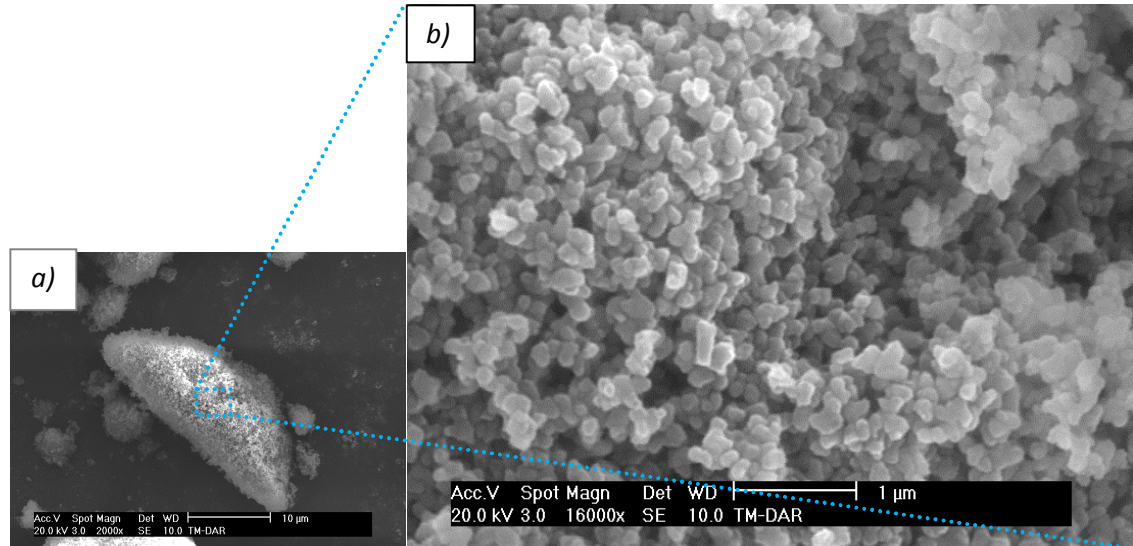
Figure 5.6: *SEM micrographs of **a)** soft agglomerates and **b)** normal particle shapes and sizes on the surface of an agglomerate of as received TM-DAR Al_2O_3.*

Morfology of synthesized $Al_2O_3 - NiO$ powder and size of NiO particles were studied using TEM and EDS (Figure 5.7). Particle size of NiO was found to be approximately 20 - 50 nm. NiO particles were attached to Al_2O_3 particles indicating that a strong chemical bond was established during the oxidation treatment. This will help to obtain good dispersion of Ni in the final pre-compact using different forming methods (slip casting, pressing etc.).

Decomposition generates metal oxide particles with various grain sizes depending on the salt that is used, but that are nevertheless in nanometer scale. Experimental results of Esteban-Betegón et al. [37] show that nitrate solution creates smallest Ni particles that are in range of $20 - 50$ nm. Experimental of this study show very similar results.
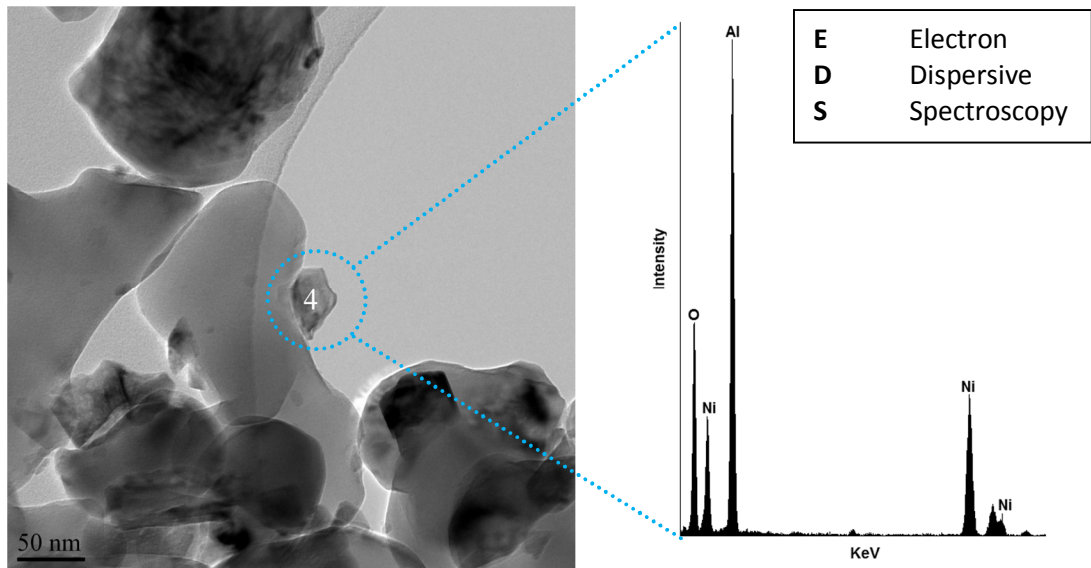
Figure 5.7: a) *TEM-image of $Al_2O_3 - NiO$ 2.5 vol. % powder and **b)** EDS -analysis of the nickel containing particle (4) and its surroundings.*

As the SEM cross-section images (figures 5.11 and 5.12) and grain size measurements of sintered nanocomposite material indicate, the particle size of nickel grows significantly during sintering phase.

5.5   Powder processing and sintering results

First sintered specimen was littered with foreign particles from the planetary ball milling process (Figure 5.8). The milling time before thermolysis for this specimen was high, approximately 24 h. Using EDS analysis, the foreign particles where identified as Al_2O_3 and ZrO_2 (grinding balls where Al_2O_3 and cup ZrO_2). Mainly because of these large impurities, sintered density was <90 % of theoretical density. Due to low density, milling time for next samples was reduced to 5 h and using the same sintering temperature and parameters, density rose to 96.3 % of theoretical density. Used sintering temperature using PECS was also low, 1150 ˚C, which partly explains the low density.

For the final samples, milling time was kept at 5 h and sintering temperature was increased to 1225 ˚C and as a consequence density rose to >99 % of theoretical density. Table 5.2 compares the density of $Al_2O_3 - Ni$ 2.5 vol. % samples obtained with different milling times and sintering temperatures.

Table 5.2: *Comparison of planetary ball milling time during powder synthesis, sintering temperature (PECS) and corresponding sintered density of $Al_2O_3 - Ni$ 2.5 vol. % samples.*

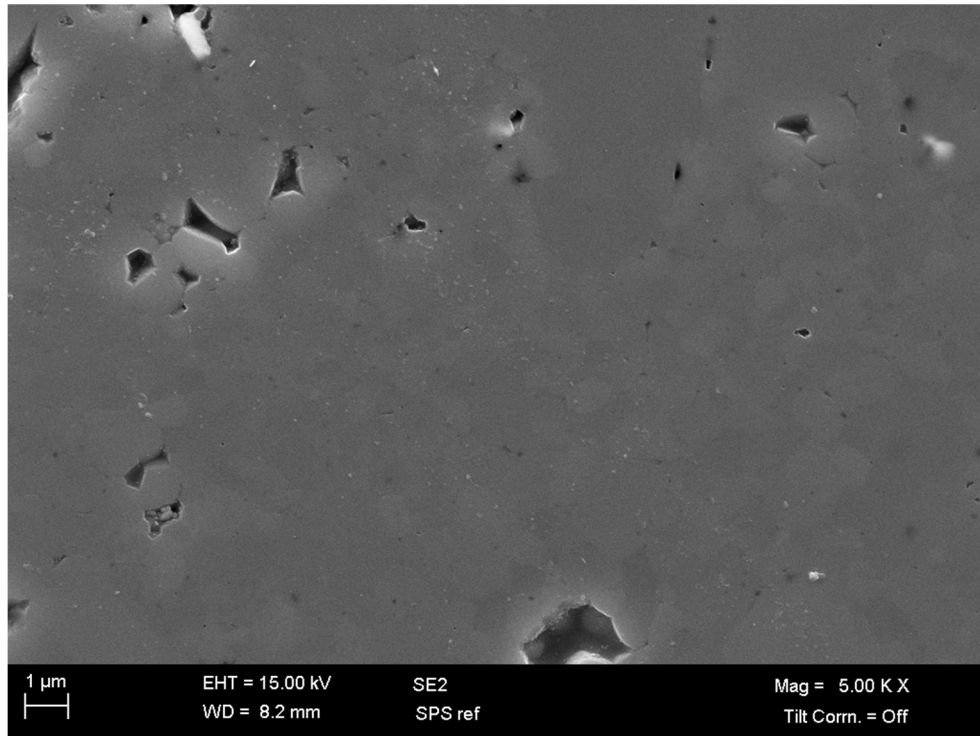| Milling time	Sintering temperature	Sintered density (T.D. %)
24 h	1150 ˚C	<90
5 h	1150 ˚C	96.3
5 h	1225 ˚C	99.5
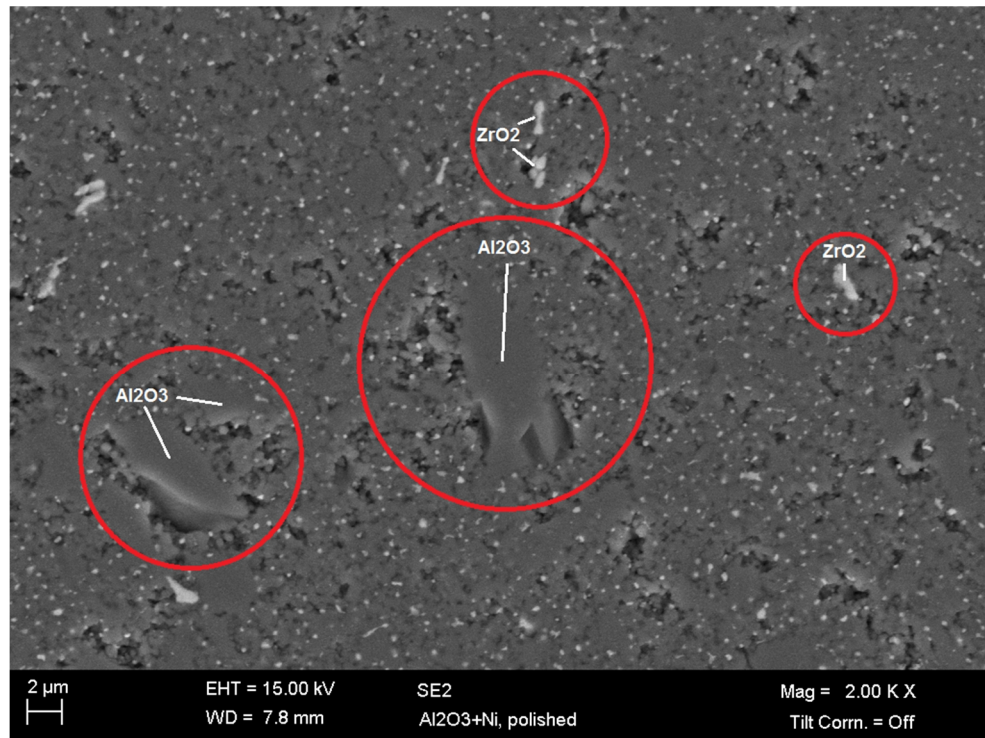
Figure 5.8: Dense Al_2O_3 and ZrO_2 impurities (O) caused by ball milling of the $Al_2O_3 - Ni$ 2.5 vol. % nanocomposite and porosity near the impurities (<90 % of T.D.).
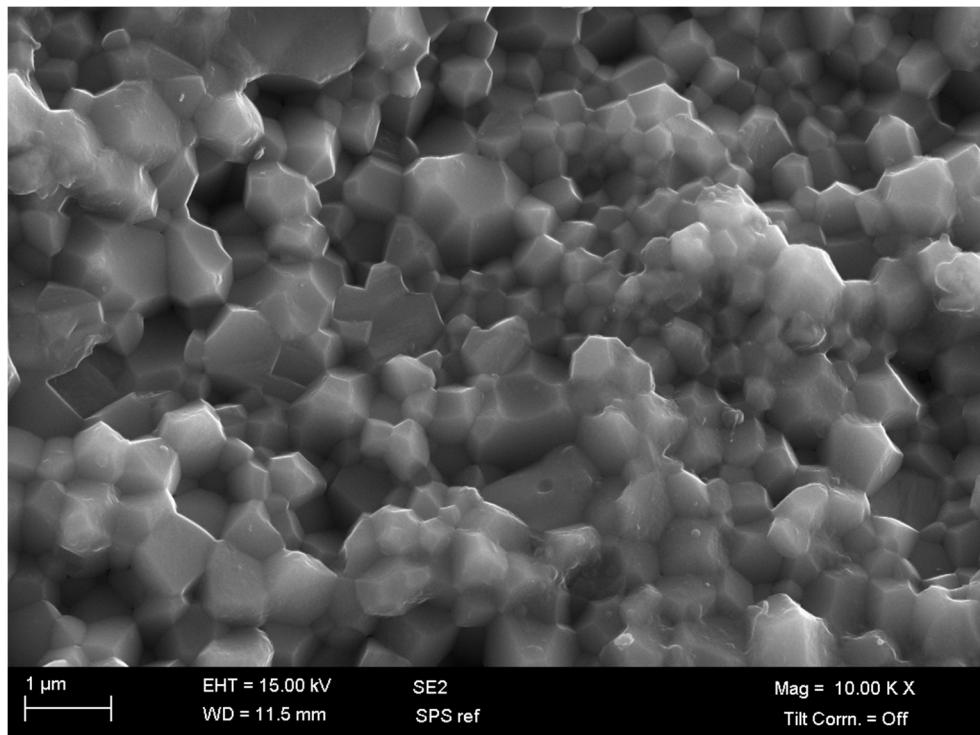
5.6 Microstructures and grain size

SEM cross section and fracture surface of pure Al_2O_3 are shown in figures 5.9 and 5.10 which show localized porosity and typical intergranular fracture mode.
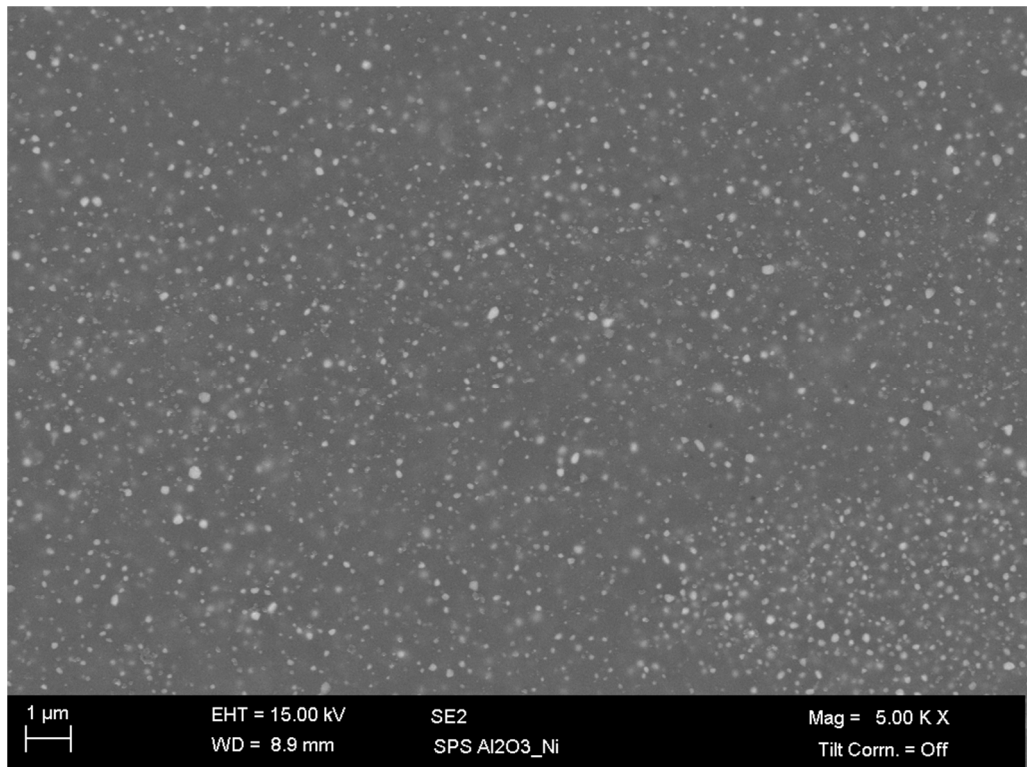
SEM cross section and fractured surface images of the $Al_2O_3 - Ni$ 2.5 vol. % nanocomposite samples are shown figure 5.11 and 5.12. Polished cross section image shows that the structure is dense with only a fraction of inner porosity. There is an indication that ball milling during either the synthesis phase or the slip mixing phase leads to growth of nickel particles in the sintered samples. This is indicated by a small fraction of substantially larger nickel particles (200 - 300 nm) in the microstructure and by local changes in the distribution of nickel particles (brighter phase) in the alumina matrix (darker phase). Fractured surface image of $Al_2O_3 - Ni$ revealed that Ni particles are totally dispersed in the matrix and confirm that thermolysis is a plausible method to produce good quality ceramic nanocomposites. Fractured surface also indicates Ni grain pull out and partial change of fracture mode from intergranular to transgranular. Clear majority of the nickel particles were found to locate at the grain boundaries of Al_2O_3 matrix.

| 1 μm | EHT = 15.00 kV | SE2 | | Mag = 5.00 K X |
| | WD = 8.2 mm | SPS ref | | Tilt Corrn. = Off |

Figure 5.9: *Polished surface (1 μm) of a pure Al_2O_3. (>99 % T.D.)*

| 1 μm | EHT = 15.00 kV | SE2 | | Mag = 10.00 K X |
| | WD = 11.5 mm | SPS ref | | Tilt Corrn. = Off |

Figure 5.10: *Fractured surface of a pure Al_2O_3 (>99 % T.D.). [18]*

55

Figure 5.11: *Polished (1 µm) cross section of $Al_2O_3 - Ni$ 2.5 vol. % sample, where brighter phase is nickel (>99 % T.D.).*
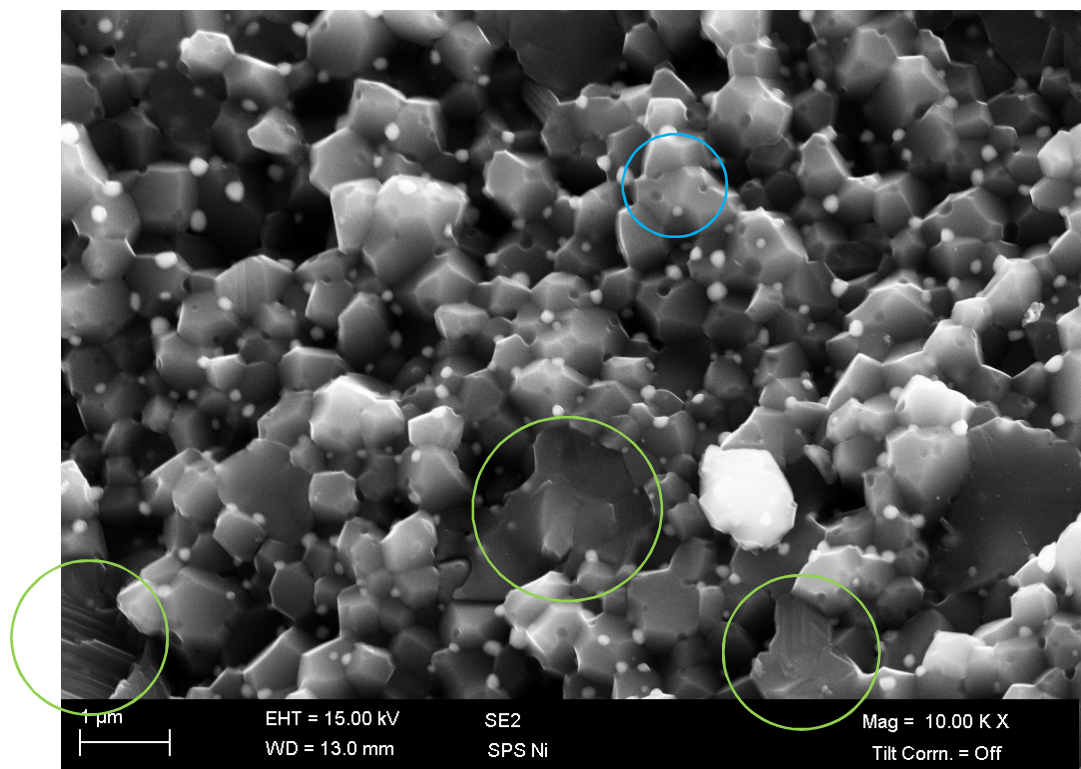
Figure 5.12: *Fracture surface of $Al_2O_3 - Ni$ 2.5 vol. % sample, where brighter phase is nickel. (>99 % T.D.). Image shows pull-out of nickel grains (O) and transgranular fracture mode (O). [18]*

Table 5.3 is showing that the Al_2O_3 grain size of $Al_2O_3 - Ni$ was lower compared to pure Al_2O_3, due to Ni particles pinning grain boundaries and inhibiting grain boundary migration/necking of matrix particles during sintering. Because of the ability to limit matrix grain growth, nanocomposites offer possibly a route to obtain very fine microstructures (≈10 nm). For best effect, the distribution of the grain growth inhibiting particles must be the optimal, which again is obtained during the processing phase.

Table 5.3: *Grain size and densities of samples sintered with PECS. [18]*

Sample Material	$Al_2O_3 - Ni$ (2.5 vol. %)	Pure Al_2O_3
Al_2O_3 grain size [μm]	0.66 ± 0.16	0.72 ± 0.25
Ni grain size [nm]	110 ± 37	-
Sintered density (T.D. %)	99.5	99.7

As I previously discussed, nano-sized nickel can have both hardening and toughening effect on the matrix. Hardness growth of $Al_2O_3 - Ni$ has been attributed to nickel particles under a certain critical size range (<60 nm) [9] and 1.3 % of nickel was found to be in that particular size range by measuring whole particles from the fractured surface image. Table 5.4 shows the cumulative size distribution of nickel in the $Al_2O_3 - Ni$ samples. [18]

**Table 5.4:** *Cumulative size distribution of nickel particles in $Al_2O_3 - Ni$ 2.5 vol. % nanocomposite. [18]*

| Ni grain size	% of Ni grains	Ni grain size	% of Ni grains
< 60 nm	1.3	< 80 nm	19.2
< 70 nm	7.7	> 80 nm	80.8

5.7 Analysis of indentation fracture (IF) method

Measuring fracture toughness of monolithic ceramics is a trade-off between reliability and practicality. The used test methods are flexural test with pre-cracked samples (Single-edge V-notch beam test (SEVNB) etc.) or indentation fracture (IF) method. Pre-cracked flexure methods own better calibration capabilities therefore separate results are easier to compare but are laborious to conduct. Indentation fracture method is still widely used for its convenience and quick implementation but calibration of the test method is difficult and therefore separate results are hard to compare reliably. Often the indentation method is still more useful for the purpose and there have been many attempts to make the method more comparable [40, 45]. Also many experimental studies concentrate on studying the indentation method for ceramic materials [41, 46].

Figure 5.13 and 5.14 represents the test procedure for indentation facture (IF) method for pure Al_2O_3 and $Al_2O_3 - Ni$ nanocomposite. Small grain size of the samples in this study made IF method easier, because the samples are easier to polish and seldom chip during indentation. Red indicator paint was used to ease the observation of the crack length in optical microscope images. An image processing software (Image Tool) was used to measure the indentation and crack lengths from the images.
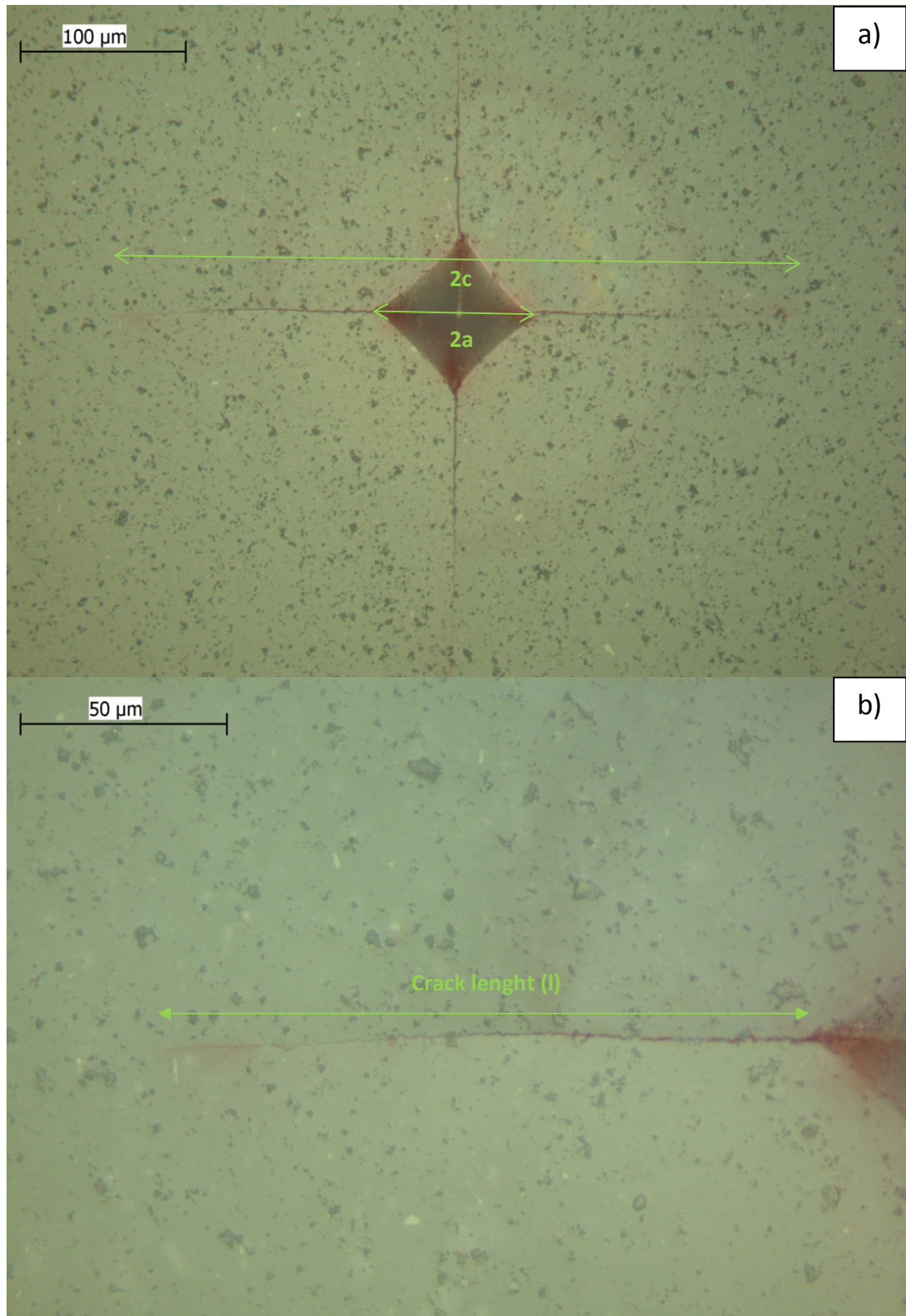
Figure 5.13: *Implementation of indentation fracture (IF) method on pure Al_2O_3 with optical microscopy:* *a)* *showing the Al_2O_3 surface after indentation with 10 kg/98 N and* *b)* *image that was used to measure the median crack length for the indentation.*
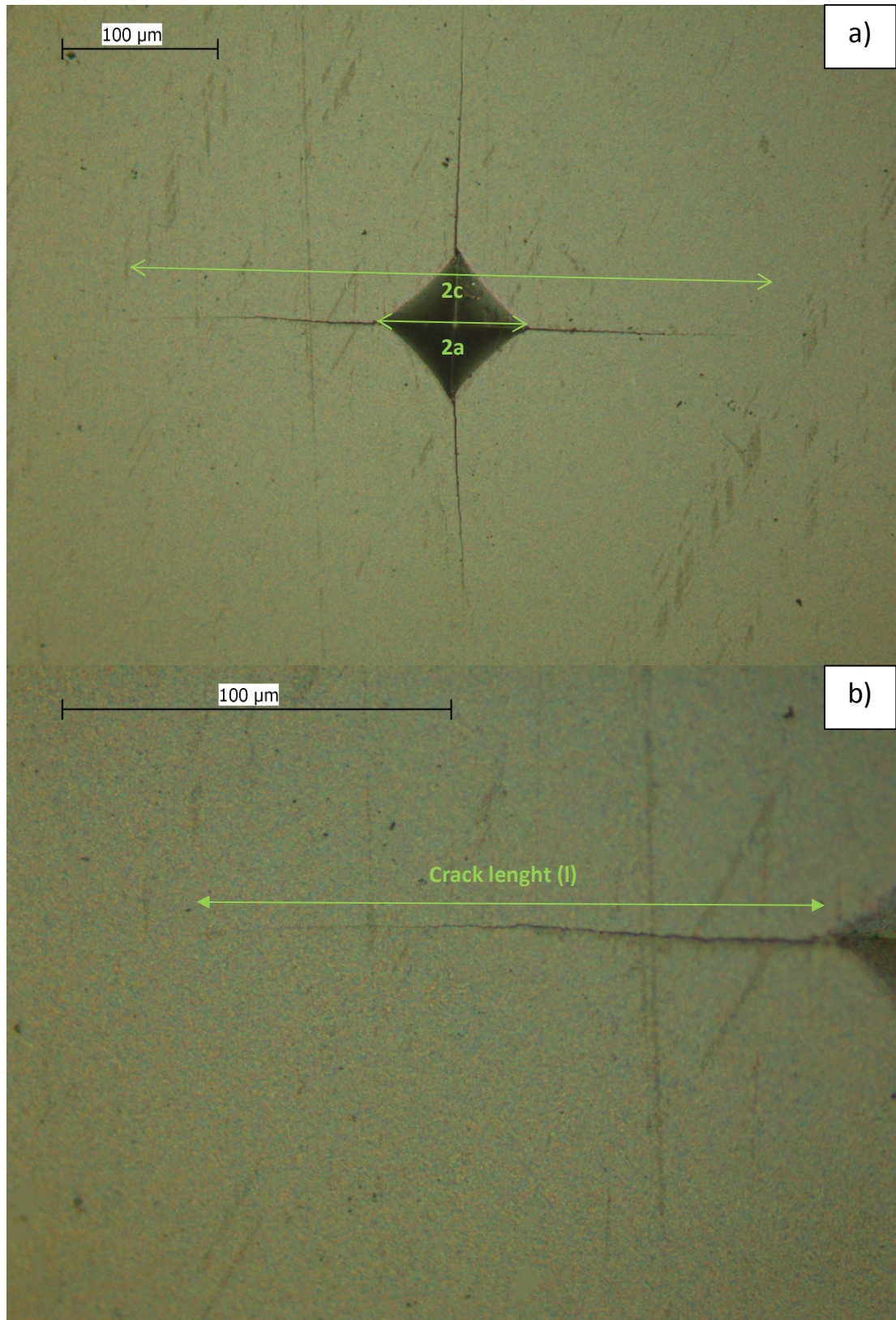
Figure 5.14: *Implementation of indentation fracture (IF) method on $Al_2O_3 - Ni$ 2.5 vol. % nanocomposite with optical microscopy: **a)** showing the $Al_2O_3 - Ni$ surface after indentation with 10 kg/98 N and **b)** image that was used to measure the median crack length for the indentation.*

Results were consistent to literature values using same methods and therefore no further testing was required.

More information on fracture toughness methods in monolithic ceramics can be found in European standard CEN/TS 14425-1 which list the problems related to IF method and for example states that the IF method should be used only for materials with $K_{IC} < 6\ MPa\sqrt{m}$.

5.8   Mechanical properties

Sintered densities, linear thermal expansion values of pure materials and mechanical properties of the samples are summarized in table 5.5. Initially the small obtained grain size gives higher initial hardness for Al_2O_3 compared to a larger grain size Al_2O_3 but at the same time smaller size has adverse effect on fracture toughness.

Hardness of $Al_2O_3 - Ni$ 2.5 vol. % was found to increase slightly compared to pure Al_2O_3. Small increase is consistent with the small fraction (1.3 %) of nickel particles under the critical size (<60 nm) and also consistent with values reported in literature [4]. Due to high scattering of hardness measurements of pure Al_2O_3, the hardness of $Al_2O_3 - Ni$ is inside error margins of pure Al_2O_3. This can make analysing the results difficult, but hardness values predicted by the rule of mixtures are still substantially lower than the measured values, which indicates that hardening has occurred. Previous study by Kannisto et al. [18] confirms that the interfacial properties determine whether hardening is possible or not because for $Al_2O_3 - ZrO_2$ 10 vol. % (with similar particle size) no hardening was observed.

Fracture toughness of $Al_2O_3 - Ni$ 2.5 vol. % was also found to increase compared to pure Al_2O_3. As a previous study of alumina nanocomposites indicates [18], toughening is probably caused by the residual stresses created by mismatch of linear thermal expansion of the different materials. It is important to notice that residual stress caused by the second phase particles (Ni, ZrO_2), will have a significant impact on fracture toughness, but will not cause hardness to increase.

Table 5.5: Physical and mechanical properties of samples sintered with PECS. [18]

Sample material	$Al_2O_3 - Ni$ (2.5 vol. %)	Pure Al_2O_3
Density [% T.D.]	99.5	99.7
α [$10^{-6}(K^{-1})$]*	8.6 / 13.3	8.6
H_v [GPa]		
0.2 kg [1,96 N]	22.4 ± 0.6	21.3 ± 1.2
1.0 kg [9,8 N]	22.5 ± 0.1	22.0 ± 0.6
10 kg [98 N]	21.4 ± 0.6	21.8 ± 0.8
K_{IC} [MPa m$^{1/2}$]	3.5 ± 0.2	3.1 ± 0.1

*Literature values

Based on the results, basic mechanical relationships between matrix and second phase particles still remain unanswered. Future research should concentrate on producing well defined nanocomposite structures and new testing methods to determine the principal properties of ceramic/metal interface in nanostructured ceramics.

6. Conclusion

As the main result of this thesis, fabrication of $Al_2O_3 - Ni$ nanocomposites was successfully demonstrated. Two research articles were published from related subjects before completion of this thesis: First, in collaboration with Aalto University, peer reviewed research article published in Key Engineering Materials journal and secondly a conference article presented in the European Ceramic Society's "2nd international conference for students and young scientist on materials processing science". Related conference presentation "Geometrical model to evaluate the lower boundary of nanoparticle size in ceramic/metal nanocomposites produced by thermolysis" won the 2nd prize for best lecture granted by JECS Trust. Full research papers and diploma are attached in the appendix.

In the literature survey part of this thesis, it was made clear that debate concerning causes of mechanical properties in nanocomposites is still under way and that satisfactory research activity around ceramic nanocomposites is still present. There is a need for comprehensive theory about the size effect of metal nanoparticles in ceramic nanocomposites, but at the moment plenty more basic research is needed to determine even the basic intrinsic properties of metal and ceramic nanoparticles and ceramic/metal interfacial properties. Hardening effect has been already studied broadly and the theoretical hardening model by Pecharromán et al. seems to apply also to the results presented in this thesis. Currently the main difficulty is the lack of good experimental methods to characterize the properties of single interface or single nanoparticle properties and further effort should be made to make characterization possible.

In experimental part, thermolysis of $Al_2O_3 - Ni$ nanocomposites was demonstrated and processing of nanocomposites by slip casting was demonstrated to be a feasible method to obtain dense nanocomposites which retain a desirable dispersion of nickel nanoparticles inside the alumina matrix. Synthesised $Al_2O_3 - NiO$ powders where studied using TEM and EDS and the NiO particle size was found to be $20 - 50$ nm. After slip casting and sintering the average nickel particle size was found to increase to 110 ± 37 nm. Locally significantly larger nickel particles (200 - 300 nm) were found and were characterized to be a cause by the wet milling before slip casting. A geometrical model for predicting grain growth of Ni nanoparticles produced by thermolysis was reviewed and discussed. In XRD studies of sintered samples, no significant oxidation or phase changes were found to happen in nickel particles during sintering of $Al_2O_3 - Ni$ samples.

In SEM cross section and fracture surface images, majority of nickel particles were found to be located at grain boundaries of matrix alumina. A small (1.3 %) fraction of nickel particles were found to be under a critical size (<60 nm), which has been attributed to increase the composite hardness. Hardness measurements conducted to nanocomposite and reference samples which confirmed a small (2 %) increase of hardness in $Al_2O_3 - Ni$ nanocomposite. Larger nickel particles have been reported to increase the fracture toughness of the composite and fracture toughness measurements confirmed a 13 % increase in fracture toughness compared to reference alumina. Increased fracture toughness can be explained by major difference of linear thermal expansion rates between alumina and nickel. Previous studies have found improvement in wear resistance of $Al_2O_3 - Ni$ compared to reference alumina, which can be explained by a change in fracture mode from intergranular to transgranular fracture observed also in SEM fracture surface studies of this thesis.

References

[1]   Niihara Koichi, "New design concept of structural ceramics: Ceramic nanocomposites", Journal of the ceramic society of Japan, Vol. 99, No. 10, 974-892, 1991

[2]   E. J. Kannisto, "Ceramic nanocomposites: Enhanced wear properties of alumina", report of Department of Materials Science, Tampere University of Technology, 2011

[3]   J. S. Moya, T. Rodriques-Suarez, S. Lopez-Esteban, C. Pecharromán, R. Torrecillas, L. A. Días and M. Nygren, "Diamond-like hardening of alumina/Ni nanocomposites", Advanced engineering materials, Vol. 9, No. 10, 898-901, 2007

[4]   T. Rodrigues-Suarez, J.F. Bartolomé, A. Smirnov, S. Lopez-Esteban, R. Torrecillas, J.S. Moya, "Sliding wear behaviour of alumina/nickel nanocomposites processed by a conventional sintering route", Journal of the European Ceramic Society, Vol. 31, p. 1389-1395, 2011

[5]   A. Smirnov, J. F. Bartolomé, J. S. Moya, F. Kern, R. Gadow, "Dry reciprocating sliding wear behavior of alumina-silicon carbide nanocomposite fabricated by ceramic injection moulding", Journal of the European Ceramic Society, Vol. 31, p. 469-474, 2011

[6]   H. Awaji, Y. Nishimura, S-M. Choi, Y. Takahashi, T. Goto and S. Hashimoto, "Toughening mechanism and frontal process zone size of ceramics", Journal of Ceramic Society of Japan Vol. 117, No. 5, 623-629, 2009

[7]   M. Sternitzke, "Structural ceramic nanocomposites", Journal of the European Ceramic Society, Vol. 17, 1061-1082, 1997

[8]   J. S. Moya, S. Lopez-Esteban, C. Pecharromán, "The challenge of ceramic/metal microcomposites and nanocomposites", Progress in materials science, Vol. 52, 1017-1090, 2007

[9]   C. Pecharromán, F. Esteban-Betegon, J. F. Bartolomé, Gunther Richter and J. S. Moya, "Theoretical model of hardening in Zirconia-Nickel Nanoparticle composites", Nano Letters, Vol. 4, No. 4, 747-751, 2004

[10]   J. Chevalier,* S. Deville, and G. Fantozzi , "Nanostructured ceramic oxides with a slow crack growth resistance close to covalent materials" Nano letters, Vol.5, No. 7, 1297-1301, 2005

[11]   S. Veprek, R. F. Zhang, M. G. J. Veprek-Heijman, S. H. Sheng, A. S. Argon, "Super hard nanocomposites: Origin of hardness enhancement, properties and applications", Surface & coatings technology, Vol. 204, 1898-1906, 2010

[12]   A. S. Mohammadabadi, K. Dehghani, "A new model for inverse Hall-Petch relation of nanocrystalline materials", Journal of materials engineering and performance, Vol. 17, No. 5, 662-666, 2008

[13]   W. Guofeng, Z. Kaifeng, J. Hua, L. Boyang, Y. Boping, "Low-temperature superplasticity of Al2O3(p)/Ni-Co nanocomposites" Materials & Desing, Vol. 33, 399–404, 2012

[14]   H. Awaji, S-M. Choi, E. Yagi, "Mechanisms of toughening and strengthening in ceramic-based nanocomposites", Mechanics of materials, Vol. 34, 411-422, 2002

[15]   S-M. Choi, H. Awaji, "Nanocomposites – a new material design concept", Science and technology of advanced materials, Vol. 6, 2-10, 2005

[16]   H. Reveron, O. Zaafrani, G. Fantozzi, "Microstructure development, hardness, toughness and creep behavior of pressureless sintered alumina/SiC micro-nanocomposites obtained by slip-casting" Journal of European ceramic society, Vol. 30, 1351-1357, 2010

[17]   S. Maensiri, S. G. Roberts, "Thermal shock of ground and polished alumina and Al_2O_3/SiC nanocomposites", Journal of the European ceramic society, Vol. 22, 2945-2956, 2002

[18]   E. Kannisto, E. Cura, E. Levänen, S-P Hannula, "Mechanical properties of alumina nanocomposites" Key engineering materials, Vol. 527, 101–106, 2013

[19]   H. Awaji, S-M. Choi, E. Yagi, "Mechanisms of toughening and strengthening in ceramic-based nanocomposites", Mechanics of materials, Vol. 34, 411-422, 2002

[20]   I.E. Reimanis, "A review of issues in the fracture of interfacial ceramics and ceramic composites, Materials Science and Engineering, Vol. A237, 159–167, 1997

[21]   S-M. Choi, H. Awaji, "Nanocomposites – a new material design concept", Science and technology of advanced materials, Vol. 6, 2-10, 2005

[22]   Y. Nishimura, K. Aikawa, S-M Choi, S. Hashimoto, Y. Iwamoto, "Relation between functional properties of alumina-based nanocomposites and dislocations of dispersed particles", Journal of the ceramic society of Japan, Vol. 117, No. 7, 836-841, 2009

[23]   A. Koller, "Structure and properties of ceramics", Materials science monographs 80, Elsevier science publishers, 1994

[24]   E. Calvié, L. Joly-Pottuz, C. Esnouf, P. Clément, V. Granier, J. Checalier, Y. Jorand, A. Malchére, T. Epicier, K. Masenelli-Varlot, "Real time TEM observation of alumina ceramic nano-particles during compression" Journal of European Ceramic Society, Vol. 32, 2067–2071, 2012

[25]   K. P. D. Lagerlöf, A. H. Heuer, J. Cataing, J. P. Riviére, T. E. Mitchell, "Slip and twinning in sapphire α-(Al_2O_3)", Journal of American ceramic society, Vol. 77, 385-397, 1994

[26]   H. Awaji, Y. Nishimura, S-M. Choi, Y. Takahashi, T. Goto and S. Hashimoto, "Toughnening mechanism and frontal process zone size of ceramics", Journal of ceramic society of Japan, Vol. 117, No. 5, 623-629, 2009

[27]   M. N. Rahaman, "Ceramic processing", Taylor & Francis Group, 2007

[28]   J. S. Reed, "Principles of ceramic processing", John Wiley & Sons inc., 1995

[29]   J. A. Lewis, "Colloidal processing of ceramics", Journal of American ceramic society, Vol. 83, 2341 – 2359, 2000

[30]   C. H. Schilling in "Colloid casting", Encyclopedia of materials: Science and technology, Elsevier, p. 1314-1319, 2001

[31]   A. U. Khan, B. J. Briscoe, P. F. Luckham, "Interaction of binders with dispersant stabilised alumina suspensions", Colloids and Surfaces A: Physicochemical and Engineering Aspects, Vol. 161, 243–257, 2000

[32]   M. Michálková , K. Ghillányová, D. Galusek, "The influence of solid loading in suspensions of a submicrometric alumina powder on green and sintered pressure filtrated samples", Ceramics International, Vol. 36, 385–390, 2010

[33]   J. Silvonen, "Keraamien lietevalu", Master's thesis, Tampereen teknillinen korkeakoulu, 1998

[34]   W. Zeng, L. Gao, L. Gui, J. Guo, "Sintering kinetics of $\alpha - Al_2O_3$ powder", Ceramics international, Vol. 25, 723-726, 1999

[35]   R. L. Coble, "Transparent alumina and method of preparation", U. S. Patent #3, 026, 210, 1962

[36]   C.S. Smith, "Grains, phases, and interphases: an interpretation of microstructure", Trans. AIME, Vol. 175, 15–51, 1948

[37]   F. Esteban-Betegón, S. Lopez-Esteban, J. Requena, C. Pecharromán and J. S. Moya, "Obtaining Ni nanoparticles on 3Y-TZP powder from nickel salts", Journal of American ceramic society, Vol. 89, 144–150, 2006

[38]   W. M. Keely, H. W. Maynor, "Thermal studies of nickel, cobalt, iron and copper oxides and nitrates", Journal of chemical and engineering data, Vol. 8, No. 3, 297–300, 1963

[39]   E. Mikuli, A. Migdal-Mikuli, R. Chyzy, B.Grad, R. Dziembaj, "Melting and thermal decomposition of $[Ni(H_2O)_6](NO_3)_2$", Thermochimica acta, Vol. 370, 65–71, 2001

[40]   K. Niihara; R. Morena; D.P.H. Hasselman In: R.C. Bradt; A.G. Evans; D.P.H. Hasselman; F. F. Lange (eds.), Fracture mechanics of ceramics, New York, Plenum: v. 5 (1983) pp. 97.

[41]   F. Sergejev, M. Antonov, "Comparative study on indentation fracture toughness measurements of cemented carbides", Proceedings of Estonian academy of sciences engineering, Vol. 12, No. 4, 388–398, 2006

[42]   T. Rodriguez-Suarez , J.F. Bartolomé , J.S. Moya, "Mechanical and tribological properties of ceramic/metal composites: A review of phenomena spanning from the nanometer to the micrometer length scale", Journal of the European Ceramic Society, Vol. 32, 3887–3898, 2012, http://dx.doi.org/10.1016/j.jeurceramsoc.2012.06.026

[43]   E. Kannisto, E. Levänen, "Geometrical Model to Evaluate the Lower Boundary of Nanoparticle Size in Ceramic/Metal Nanocomposites Produced By Thermolysis", Journal of the Georgian ceramists' association, Vol. 28, No. 2, 24-29, 2012

[44]   T. Isobe, K. Daimon, K. Ito, T. Matsubara, Y. Hikichi, T. Ota, "Preparation and properties of Al2O3/Ni composite from NiAl2O4 spinel by in situ reaction sintering method" Ceramics international, Vol. 33, 1211–1215, 2007

[45]   P. Miranzo and J. S. Moya, "Elastic/plastic indentation in ceramics: a fracture toughness determination method", Ceramics International, Vol. 10, No. 4, 147–152, 1984

[46]   M. Moraesa, C. Eliasa, J. Filhob, L. Oliveirab, "Mechanical Properties of Alumina-Zirconia Composites for Ceramic Abutments Materials Research, Vol. 7, No. 4, 643–649, 2004

Appendix

Publication I

E. Kannisto, E. Cura, E. Levänen and S-P Hannula

"Mechanical properties of alumina nanocomposites"
Key engineering materials Vol. 527, 101–106, 2013

Mechanical Properties of Alumina Based Nanocomposites

Erkka Kannisto[1,a], Erkin Cura[2,b], Erkki Levänen[1,c], Simo-Pekka Hannula[2,d]

[1]Department of Materials Science, Tampere University of Technology, P.O. Box 589, FI-33101 Tampere, Finland

[2]Department of Materials Science and Engineering, Aalto University, P.O. Box 16200, FI-00076 AALTO, Finland

[a]erkka.kannisto@tut.fi (corresponding author), [b]erkin.cura@aalto.fi, [c]erkki.levanen@tut.fi, [d]simo-pekka.hannula@aalto.fi

Keywords: Alumina, Al_2O_3, Nickel, Zirconia, ZrO_2, Nanocomposite, Slip casting, Pulsed electric current sintering, Grain size, Hardness, Fracture toughness

Abstract. To study the microstructure and mechanical properties of alumina nanocomposites, Al_2O_3/2.5 vol.% Ni and Al_2O_3/10 vol.% ZrO_2 nanocomposites were consolidated by pulsed electric current sintering (PECS). Fracture toughness was found to increase by 13 % and 16 % respectively compared to reference alumina. Hardness increased slightly in Al_2O_3/Ni because of a fraction of nickel particles under the critical size (<60 nm), but was lower in Al_2O_3/ZrO_2 following the rule of mixtures. By investigating the results, causes of improved mechanical properties were critically evaluated.

Introduction

Ceramic nanocomposites offer a unique approach on changing several material properties. With sufficiently small size of the second phase particles (1-100 nm), improved properties may arise by the size effect alone. Such an effect is for example Hall-Petch type of hardening [1].

Nanocomposite design in conventional engineering ceramics has been reported to give exceptional rise in wear resistance [2,3] and to introduce radical changes in wear mechanisms [3,4]. Studies also indicate small or moderate increase in hardness and fracture toughness [2-5] and also significant grain growth inhibition during sintering caused by the second phase particles at the matrix grain boundaries [2-5]. Connection between mechanical properties and wear resistance is unclear, partly because of the inability to characterize the inherent properties of the nanoparticles, since maintaining the nano-scale microstructure in the sintered bulk materials is very difficult. Therefore at the moment there are only indirect results on, for example nanocomposite structures, which help to retain the nanostructure. Mechanisms that cause the enhanced mechanical properties of ceramic nanocomposites were [6] and are still under a debate [7,8].

In this study we demonstrate slip casting of Al_2O_3/Ni nanocomposites without a separate infiltration step [9] and compare Al_2O_3/Ni and Al_2O_3/ZrO_2 nanocomposite materials consolidated with PECS, regarding to their mechanical properties. By investigating the results, hardening and toughening mechanisms of alumina nanocomposites were critically evaluated.

Experimental Procedure

Materials Processing. For the Al_2O_3/Ni nanocomposite, starting materials were α-Al_2O_3 powder (TM-DAR consisting of > 99.9 % α-Al_2O_3, d_{50} = 0.2 μm and BET specific surface area of 14.5 m^2/g, Taimei chemicals CO., Ltd, Japan) and Nickel (II) nitrate hexahydrate ($N_2NiO6·6H_2O$, assay min. >96 %, BDH Prolabo, VWR international). Powder synthesis was done according to work by Moya et al. [2]. First the Al_2O_3 powder was mixed with solution of alcohol and nickel (II) nitrate hexahydrate that was measured to yield 2.5 vol.% of nickel in the final Al_2O_3/Ni composite. Mixture was milled in planetary ball mill (Pulverizette 5, Fritsch GmbH.) for 5 h with Al_2O_3 balls with a speed of 140 rpm. Milled mixture was then dried in a convection oven at a temperature of 100–120 ˚C for 6 hours. Dried powder mixture was crushed in a mortar and then heat treated at 400

°C in air for 2 hours to thermally decompose the nickel nitrate salt into NiO. Oxidized mixture was then heat treated at 500 °C in Ar/H$_2$ 5 % atmosphere for 2 hours to reduce the nickel oxide into metallic Ni.

Al$_2$O$_3$/Ni nanocomposite samples were pre-compacted with slip casting using gypsum moulds. To prepare the slip, ion exchanged H$_2$O and 2.2 wt.% (by dry powder weight) of dispersing agent (Darvan C-N, R.T. Vandebilt Inc.) was mixed with a shear blade mixer. Nanocomposite powder was mixed with the solution and then milled at 140 rpm in a planetary ball mill (Pulverisette 5, Fritsch GmbH) for 60 min with Al$_2$O$_3$ balls. Slip was de-aired in vacuum after milling and poured into an open cylindrical mould with diameter of 11 cm. After filtration the compacted sample was released from the mould and dried at room temperature in a convection oven at 60 and 90 °C for 24 hours in each step. Cylindrical samples with a diameter of 20 mm and thickness of 5 mm were cut from the pre-compact.

Al$_2$O$_3$/ZrO$_2$ composite powders were prepared from α-alumina powder (AKP-53, Sumitomo Chem. Ltd. Co. Japan) and 3 mol% yttria stabilized zirconia powder (TZ-3Y-E, Tosoh Corp. Japan) having the average particle size of 290 nm and 27 nm, respectively. 10 vol.% (≈ 14 wt.%) of ZrO$_2$ was mixed with Al$_2$O$_3$ in planetary mill for 12 h. No pre-compaction was applied before the sintering.

Sintering. Pre-compacted Al$_2$O$_3$/Ni samples and Al$_2$O$_3$/ZrO$_2$ powders were consolidated using PECS equipment (FCT HP D 25-2). The pre-compacts and powders were located between two graphite punches and sintered in graphite moulds with inner diameter of 20.8 mm. The pressure and the electrical current were applied to the material through the upper punch. In order to enhance the contact area and protect the graphite parts, graphite foil with thickness of 0.4 mm was used between the material and the graphite surfaces. The temperature change during the sintering cycle was measured by a vertically placed pyrometer which measures the temperature through a hole in the upper punch, from a distance of 5 mm to the material. Direct current was applied in pulses (10:5 ms) and all the experiments were performed in a vacuum of 7 Pa.

Al$_2$O$_3$/Ni pre-compacts with a diameter of 20 mm and thickness of 5 mm were sintered at 1225 °C for 5 min. The temperature was increased step wise first from room temperature to 1100 °C then to 1200 °C and finally to 1225 °C with a heating rate of 200, 100 and 50 °C/min, respectively. In the final step the heating rate was decreased to 50 °C/min in order to prevent the over shooting in the temperature. After sintering phase, compacts were cooled down to ~ 60 °C in a natural manner with a cooling rate of about 200 °C/min. Pressure was initially 16 MPa between room temperature and 500 °C and was increased to 75 MPa with a ramp. Maximum uniaxial pressure of 75 MPa was applied at the sintering temperature as long as the dwell time. The final temperature and pressure were maintained for 5 min. Reference samples from pure alumina were sintered with the same parameters for comparison.

For Al$_2$O$_3$/ZrO$_2$ powders the applied sintering temperature, time and pressure were 1300 °C, 5 min and 50 MPa, respectively. The heating rate was 100 °C/min to 1275 °C and 50 °C/min to 1300 °C. The cooling was the same as for the Al$_2$O$_3$/Ni compacts.

Materials Characterization. Sintered densities of Al$_2$O$_3$/Ni, Al$_2$O$_3$/ZrO$_2$ and reference Al$_2$O$_3$ were measured by Archimedes method using deionised water as a penetrant. Composition of the materials was studied by X-ray diffraction (D-500, Siemens AG and PW 3830, Philips). Cross-sections and fractured surfaces of the materials were studied with scanning electron microscopes (ULTRAplus Ultra High Resolution FE-SEM, Zeiss and S-4700 Ultra High Resolution FE-SEM, Hitachi).

For SEM imaging and indentation tests, samples were polished down to 1 µm using a diamond abrasive. Cross sectioned Al$_2$O$_3$/ZrO$_2$ sample was thermally etched at 1200 °C for 30 min for SEM study. Hardness of the materials were measured using a Vickers microindentation device (MMT-X7, Matsuzawa or Duramin A300, Struers), applying a load of 1.96 N, 9.8 N or 98 N with 10 s dwell time. Vickers hardness for the sample materials were calculated with Eq. 1

$$H_v = 1.854 \; P/d^2, \tag{1}$$

where H_v is the Vickers hardness (N/mm^2, MPa), P is the applied load (N) and d is the mean of two diagonal lengths of the indentation (mm). Fracture toughness of the nanocomposites was determined with indentation fracture (IF) method using a microindentation device (Duramin A300, Struers). Testing load of 98 N with 10 s dwell time was used. Fracture toughness was calculated from the relationship of median crack length and diagonal half-length of the indentation using Niihara's equation [10] (Eq. 2)

$$K_{IC} = 0{,}129 \left(\frac{c}{a}\right)^{-3/2} \left(\frac{E\phi}{H}\right)^{2/5} \left(\frac{Ha^{1/2}}{\phi}\right) \text{ for } c/a \geq 2.5, \tag{2}$$

where K_{IC} is the fracture toughness (MPa m$^{1/2}$), c is the median crack length (m), a is the diagonal half-length of the indentation (m), E is the Young's modulus of the tested material (MPa), ϕ is a constant ≈ 3 and H is the hardness of the tested material (MPa). Young's modulus for different composites was evaluated using the rule of mixtures (E was 380 GPa for Al$_2$O$_3$, 200 GPa for Ni and 205 GPa for ZrO$_2$).

Results and Discussion

Physical Properties and Microstructure Analysis. Densities of all samples were found to be >99 % of the theoretical density. Compositions of the starting powders and sintered nanocomposites were studied using X-ray diffraction (Fig. 1). X-ray diffraction patterns confirmed the formation of metallic nickel in the reduction phase of the Al$_2$O$_3$/Ni powder synthesis and that no significant oxidation of Ni happened during sintering in vacuum conditions. In Al$_2$O$_3$/ZrO$_2$ powder, α-alumina and both monoclinic and tetragonal phases of zirconia were observed. After sintering the X-ray diffraction patterns indicate phase transformation of zirconia from monoclinic to tetragonal while alumina remains in alpha phase.
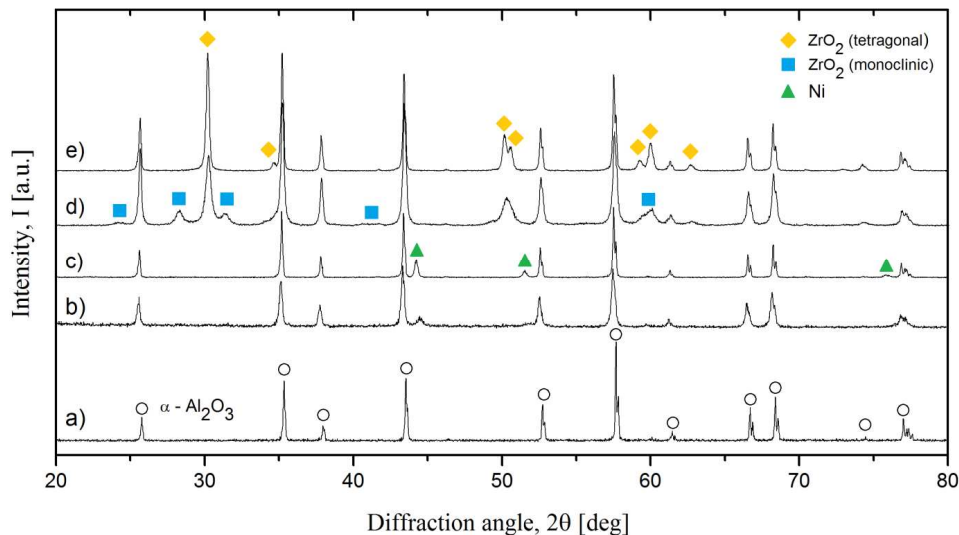

Figure 1. X-ray diffraction diagrams corresponding to (a) sintered reference Al$_2$O$_3$, (b) Al$_2$O$_3$/Ni 2.5 vol.% powder, (c) sintered Al$_2$O$_3$/Ni 2.5 vol.%, (d) Al$_2$O$_3$/ZrO$_2$ 10 vol.% powder and (e) sintered Al$_2$O$_3$/ZrO$_2$ 10 vol.%.

Fig. 2 presents the cross-sections of the nanocomposite materials. Brighter phase represents Ni in Fig. 2a and ZrO$_2$ in Fig. 2b and 2d. Nickel particles show even distribution in alumina matrix, but agglomeration of ZrO$_2$ particles was observed in sintered microstructure. Agglomeration happened due to dry milling of fine size particles. Fractured surfaces of Al$_2$O$_3$/Ni show evidence of nickel grain pullout and increased transgranular fracture through alumina grains compared to pure Al$_2$O$_3$. In Al$_2$O$_3$/ZrO$_2$ and pure Al$_2$O$_3$, fracture mode is mainly intergranular.
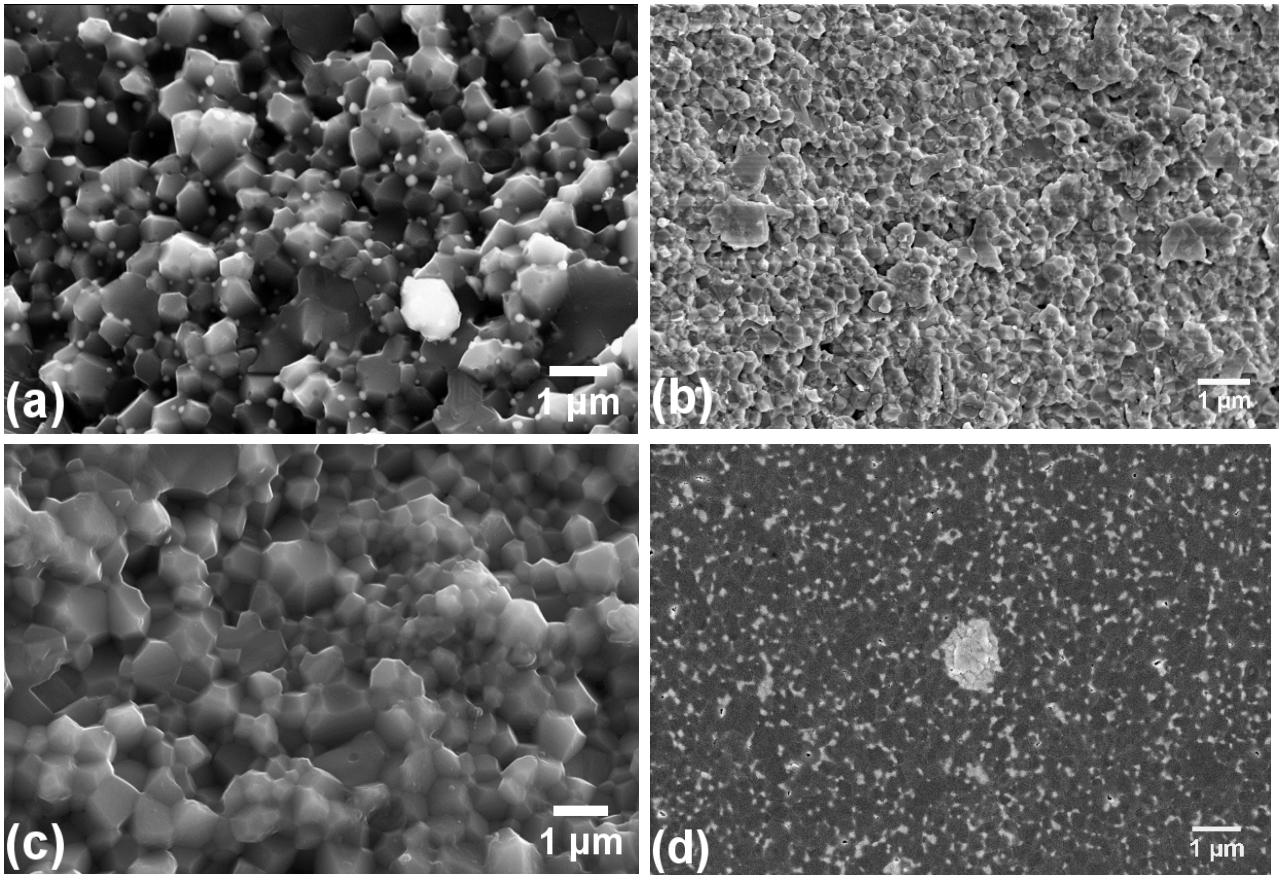
Figure 2. Fracture surface images of (a) Al$_2$O$_3$/Ni 2.5 vol.%, (b) Al$_2$O$_3$/ZrO$_2$ 10 vol.%, (c) pure Al$_2$O$_3$ reference and (d) a polished cross section image of Al$_2$O$_3$/ZrO$_2$ 10 vol.%

Grain size of different phases in nanocomposites was calculated by image analysis of cross-section samples. Minimum of 50 grains were counted for each material. Table 1 summarizes the grain sizes of different constituents in the nanocomposite samples. Alumina grain sizes in the sintered nanocomposites are lower compared to pure alumina due to second phase particles inhibiting grain boundary migration/necking between particles. In all materials, both matrix and second phase grains show similar grain size which is important to effectively compare results.

Table 1
Grain size of samples sintered with PECS.

Sample Material	Al$_2$O$_3$ / Ni	Al$_2$O$_3$ / ZrO$_2$	Pure Al$_2$O$_3$
Al$_2$O$_3$ grain size [μm]	0.66 ± 0.16	0.41 ± 0.02	0.72 ± 0.25
Ni grain size [nm]	110 ± 37	-	-
ZrO$_2$ grain size [nm]	-	105 ± 9	-

The increase of hardness in Al$_2$O$_3$/Ni nanocomposites has been attributed to a certain size range (<60 nm) of nickel particles [2]. Studying both polished and fractured microstructures we found that 1.3 % of nickel particles were in this particular size range. Table 2 shows the size distribution of nickel particles in Al$_2$O$_3$/Ni nanocomposite.

Table 2
Cumulative size distribution of nickel particles in Al_2O_3/Ni sample.

Ni grain size	% of Ni grains	Ni grain size	% of Ni grains
< 60 nm	1.3	< 80 nm	19.2
< 70 nm	7.7	> 80 nm	80.8

Hardness and Fracture Toughness. Mechanical properties and densities of the sintered materials are summarized in Table 3. Hardness of Al_2O_3/Ni has increased only slightly, which confirms the need of sufficiently small particles to harden the material, as suggested by earlier studies [2,3]. Hardness increase of Al_2O_3/Ni is inside error margins of pure Al_2O_3 which makes analyzing difficult, but hardness predicted by rule of mixtures is still substantially lower than measured values which indicate slight hardening. Results also indicate that hardening is independent of processing method and is related only to fineness of obtained microstructure. Hardness of Al_2O_3/ZrO_2 is lower compared to reference due to relatively soft ZrO_2 particles in the microstructure, and results follow values calculated by rule of mixtures. Several loading cases/penetration depths were carefully tested to be certain that the hardening is not a consequence of lapping and polishing, and therefore a mere surface property.

Table 3
Physical and mechanical properties of samples sintered with PECS.

Sample material	Al_2O_3 / Ni 2.5 vol.%	Al_2O_3 / ZrO_2 10 vol.%	pure Al_2O_3
Density [% T.D]	99.5	99.7	99.7
α [$10^{-6}(K^{-1})$]	8.6 / 13.3	8.6 / 8.9 - 10.6*	8.6
H_v [GPa]			
0.2 kg [1,96 N]	22.4 ± 0.6	21.0 ± 0.3	21.3 ± 1.2
1.0 kg [9,8 N]	22.5 ± 0.1	20.5 ± 0.5	22.0 ± 0.6
10 kg [98 N]	21.4 ± 0.6	19.9 ± 0.3	21.8 ± 0.8
K_{IC} [MPa m$^{1/2}$]	3.5 ± 0.2	3.6 ± 0.3	3.1 ± 0.1

*Dependant on the amount of stabilizing additives.

Both nanocomposites showed increased fracture toughness. Similar absolute toughness values were measured with a large difference in volume of second phase particles. All second phase particles in present work were located in matrix grain boundaries, therefore we bypass the toughening mechanism proposed for second phase particles located inside matrix grains [5]. Pullout of nickel particles could promote a "bridging effect" of nanoparticles behind the crack front. In the case of these nanocomposites this can have an effect on fracture toughness, but there is a lack of evidence in microstructure analysis that any plasticity remains in the small nickel particles as proposed earlier [3]. It is probable that residual stresses cause high dislocation concentration in nickel during cooling, therefore making further dislocation movement very hard. Local blunting of the crack front in contact of particles located in grain boundaries can dissipate the energy of the propagating crack, but it is questionable whether small particles alone ($\approx$ 100 nm) are able to cause significant path obstruction or energy dissipation to the crack front.

On the other hand, residual stresses in a material will have an effect on the crack growth, and subsequently to fracture toughness value. In Al_2O_3/Ni a large mismatch in linear thermal expansion leaves high residual stress in the sintered material [9,11]. In Al_2O_3/ZrO_2, the stress state is produced by thermal expansion mismatch, but also by well known phase transformation of tetragonal zirconia to monoclinic zirconia near the crack front [12]. We argue that the toughening is caused mainly by

the sum of residual stresses in the matrix. The residual stress state can also explain the enhanced wear properties of Al_2O_3/ZrO_2 nanocomposites [13] but also for Al_2O_3/Ni nanocomposites [2,3], because of similar elastic properties of zirconia and nickel. Partial change of fracture mode in Al_2O_3/Ni from intergranular to transgranular also indicate that internal stress state changes the weakest point in the microstructure through which crack can propagate.

Conclusion

In this study direct slip casting of Al_2O_3/Ni nanocomposite was demonstrated successfully and mechanical properties of Al_2O_3/Ni and Al_2O_3/ZrO_2 nanocomposites sintered with PECS were compared. Both nanocomposite structures had lower alumina matrix grain growth compared to monolithic alumina. Al_2O_3/Ni show slightly improved hardness compared to reference due to fraction of nickel particles under a critical size (<60 nm), whereas Al_2O_3/ZrO_2 had lower hardness following the rule of mixtures. Both nanocomposites showed increased fracture toughness (13 % and 16 %, for Ni and ZrO_2 respectively) compared to reference alumina. According to results, the increased fracture toughness was attributed to the stress state of material caused by mismatch of linear thermal expansion rates between matrix and second phase particles (for Ni and ZrO_2) and phase transformation caused by the second phase particles (for ZrO_2).

References

[1]   C. Pecharromán, F. Esteban-Betegon, J. F. Bartolomé, Gunther Richter and J. S. Moya, Theoretical model of hardening in Zirconia-Nickel Nanoparticle composites, Nano Let. 4 (2004) 747-751.

[2]   J.S. Moya, T. Rodriques-Suarez, S. Lopez-Esteban, C. Pecharromán, R. Torrecillas, L.A. Días and M. Nygren, Diamond-like hardening of alumina/Ni nanocomposites, Adv. Eng. Mater. 9 (2007) 898-901.

[3]   T. Rodrigues-Suarez, J.F. Bartolomé, A. Smirnov, S. Lopez-Esteban, R. Torrecillas, J.S. Moya, Sliding wear behaviour of alumina/nickel nanocomposites processed by a conventional sintering route, J. Eur. Ceram. Soc. 31 (2011) 1389-1395.

[4]   A. Smirnov, J.F. Bartolomé, J.S. Moya, F. Kern, R. Gadow, Dry reciprocating sliding wear behavior of alumina-silicon carbide nanocomposite fabricated by ceramic injection moulding, J. Eur. Ceram. Soc. 31 (2011) 469-474.

[5]   H. Awaji, Y. Nishimura, S-M. Choi, Y. Takahashi, T. Goto and S. Hashimoto, Toughening mechanism and frontal process zone size of ceramics, J. Ceram. Soc. Jap. 117 (2009) 623-629.

[6]   M. Sternitzke, Structural ceramic nanocomposites, J. Eur. Ceram. Soc. 17 (1997) 1061-1082.

[7]   S-M. Choi, H. Awaji, Nanocomposites – A new material design concept, Sci. Tech. Adv. Mater. 6 (2005) 2-10.

[8]   J.S. Moya, S. Lopez-Esteban, C. Pecharromán, The challenge of ceramic/metal micro and nanocomposites, Prog. Mater. Sci. 52 (2007) 1017-1090.

[9]   M. Lieberthal, W.D. Kaplan, Processing and properties of Al_2O_3 nanocomposites reinforced with sub-micron Ni and $NiAl_2O_4$, Mater. Sci. Eng. A302 (2001) 83-91.

[10]   K. Niihara; R. Morena; D.P.H. Hasselman In: R.C. Bradt; A.G. Evans; D.P.H. Hasselman; F. F. Lange (eds.), Fracture mechanics of ceramics, New York, Plenum: v. 5 (1983) pp. 97.

[11]   O. Aharon, S. Bar-Ziv, D. Gorni, T. Cohen-Hyams, W.D. Kaplan, Residual stresses and magnetic properties of alumina-nickel nanocomposites, Scripta Materialia 50 (2004) 1209-1213.

[12]   J.F. Bartolomé, G. Bruno, A.H. DeAza, Neutron diffraction residual stress analysis of zirconia toughened alumina (ZTA) composites, J. Eur. Ceram. Soc. 28 (2008) 1809-1814.

[13]   S.Novak, M. Kalin, P. Lukas, G. Anne, J. Vleugels, O. Van Der Biest, The effect of residual stresses in functionally graded alumina-ZTA composites on their wear and friction behavior, J. Eur. Ceram. Soc. 27 (2007) 151-156.

Publication II

E. Kannisto and E. Levänen

"Geometrical Model to Evaluate the Lower Boundary of Nanoparticle Size in Ceramic/Metal Nanocomposites Produced By Thermolysis"
Journal of the Georgian ceramists' association Vol. 28, No. 2, 24-29, 2012

MANUSCRIPTS

Symposium 1

1. Nanomaterials and nanotechnologies;

2. Experimental high technologies;

3. Bioceramics, microbiology and biomolecular chemistry;

4. Innovations in functional and construction materials and technologies;

5. Contemporary problems of studying and expansion of mineral material bases.

GEOMETRICAL MODEL TO EVALUATE THE LOWER BOUNDARY OF NANOPARTICLE SIZE IN CERAMIC/METAL NANOCOMPOSITES PRODUCED BY THERMOLYSIS

Erkka J. Kannisto, Erkki Levänen

Department of Materials Science, Tampere University of Technology, Finland

E-mail: erkka.kannisto@tut.fi, erkki.levanen@tut.fi

Resume: Ceramic/metal nanocomposite data reveals patterns which suggest that geometry plays an important role when sintering nanocomposites and gives information about the obtainable particle size of the second phase nanoparticles regardless of sintering method. Data suggests that matrix particle size plays the key role governing the lower boundary of obtainable second phase nanoparticles. Literature data of inter-type Al_2O_3/Ni nanocomposites were evaluated based on the model and results were found to be consistent. Data available is limited and in the future more information on different material combinations is needed to confirm the geometrical hypothesis. If proven successful, the model will broaden the tools available to study the processing of ceramic/metal nanocomposites.

Key words: Ceramic; Metal; Nanocomposite; Al_2O_3; Alumina; Ni; Nickel; Thermolysis; Nanoparticle; Particle size; Geometrical; Model; Modeling.

1. INTRODUCTION

Al_2O_3/Ni nanocomposites show great promise in enhancing mechanical properties of the traditional structural alumina ceramics. Increases in hardness [1-3] fracture toughness [2, 3] and abrasive wear resistance have been reported [1, 2]. Ceramic nanocomposite in general can be thought to consist of technical ceramic matrix (Al_2O_3, ZrO_2, SiC, Si_3N_4 etc.) and second phase nanoparticle inclusions (1-100 nm) which can be ceramic or metallic [4].

In present study we evaluate nanocomposites synthesized by thermolysis. In this method, metal salts are decomposed in moderate temperature to produce metal oxide nanoparticles on the surface of ceramic matrix particles and due to chemical reaction, the nanoparticles bond to the matrix particles [1, 5]. Afterwards the oxide nanoparticles can be reduced to metallic nanoparticles, producing a ceramic/metal nanocomposite powders. At the moment there is no comprehensive tool to evaluate or predict the size of the obtained nanoparticles in the powder or their size after sintering the powder, therefore process optimization is difficult. Optimization is important because certain features, such as hardening in ceramic nanocomposites, have been seen to arise from the size effect alone [6]. A geometrical model concerning Al_2O_3/Ni has been proposed earlier by Rodriguez-Suarez et al. [7]. Purpose of this paper is to expand their qualitative model into quantitative model which can be utilized in future research.

This paper presents a geometric tool to predict the lower boundary of obtained nanoparticle size in ceramic/metal nanocomposites. Model proposes geometrical boundary conditions to predict the size of nanoparticles

after sintering and is evaluated against Al_2O_3/Ni 2.5 vol. % nanocomposite data. We suggest, based on results and literature data, that the second phase nanoparticle formation and growth during sintering is controlled by the matrix particle size. As a result we see a linear relationship between matrix particle size and the size of synthesized nanoparticles in sintered samples. Grain growth of matrix particles during sintering is eminent but the second phase will also follow this growth by aggregating into larger particles. Geometry plays important role because available surface energy determines the material flow below melting temperatures. By controlling nanocomposite geometry we can retain the nanostructure and tailor ceramic/metal nanocomposites in the best possible way.

2. THE BODY OF THE ARTICLE

Geometrical model for nanoparticle growth during sintering

At the beginning we would like to point out that some basic principles are the same as used for ceramic crystal structures. Novelty is in the way those principles seem to apply in microstuctural level during sintering. As a starting point we have chosen an ideal particle model which consists of two distinct particle types from which the first represents ceramic matrix particles and the second phase metallic nanoparticles. We give the particle model initial boundary conditions which are:

1. Particles are perfect circles or spheres
2. Second phase metallic particles are evenly distributed in the matrix
3. Matrix particles are initially monosized and form by close packing
4. Concentration of second phase metal particles is near percolation threshold

In this hypothetic situation, particles form close packed clusters where centrally located metallic nanoparticle can have coordination number 3, 4, 6 or 8 based on the number of matrix particles surrounding it (Figure 1).
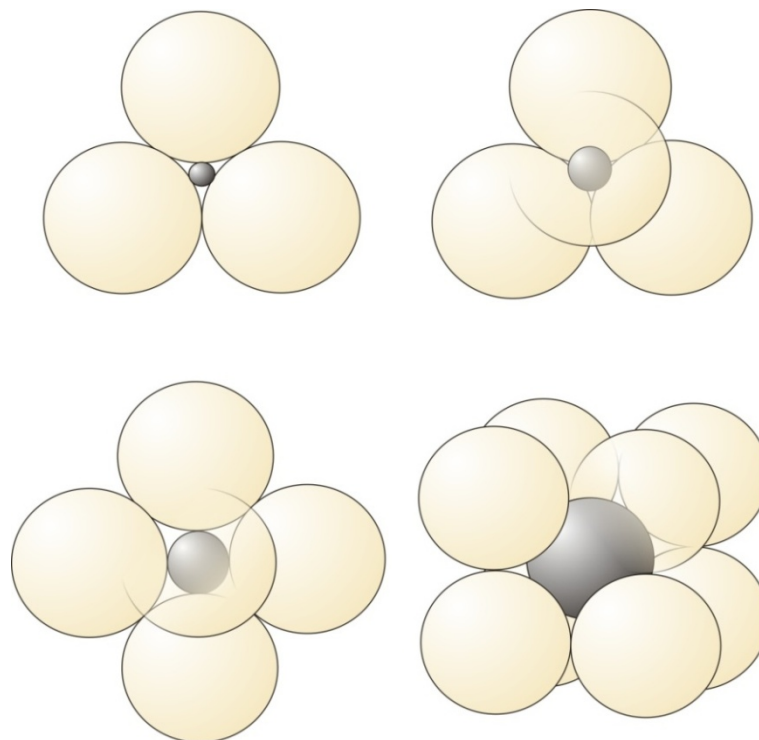
Figure 1. Ceramic/metal particle systems with different coordination numbers

Most simple version of the model is a two dimensional one with metal nanoparticle having the coordination number 3 schematically presented in figure 1a. Two dimensional model generates geometrical boundary conditions which can be schematically presented as shown in Figure 2.
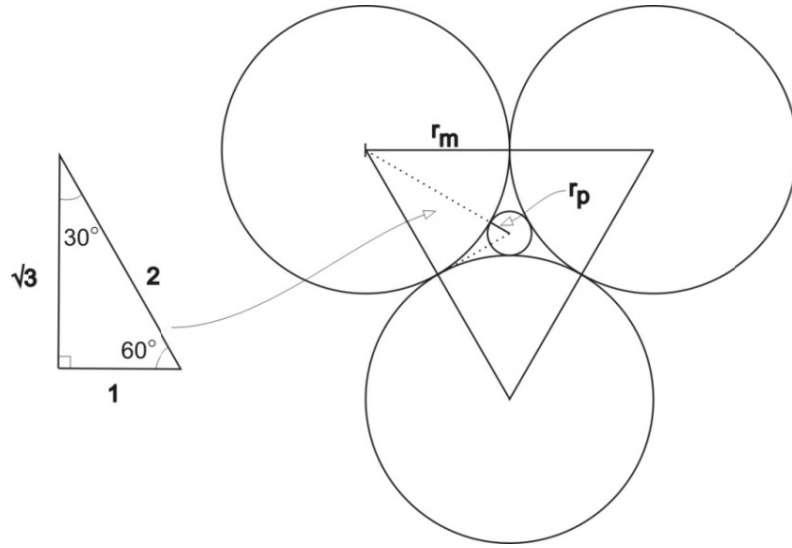
**Figure 2. Geometrical boundary conditions for 2-dimensional particle model
with nanoparticle coordination number 3**

Using these boundary conditions we know that $r_m + r_p = 2$ and that $r_m = \sqrt{3}$. Using these terms we can calculate ratio r_p/r_m, which yields

$$r_p = r_m(2 - \sqrt{3})(1/\sqrt{3}) , \qquad (1)$$

where r_p is the second phase particle radius, and r_m is the matrix particle radius. Presuming that the radius of matrix particle (r_m) is known, radius of the second phase particle can be calculated with the equation (1), or with an approximation

$$r_p \approx 0.155\, r_m . \qquad (2)$$

With coordination number 2, the size of the second particles would theoretically be < 0,155 r_m [8], although it is very unlikely that these are found in real micros-tructures, due to interaction forces between particles.

Second phase particles residing in triple junctions (tetrahedral sites) will correlate to geometrical model with coordination number 4. Geometrical boundary conditions for this model can be schematically presented as
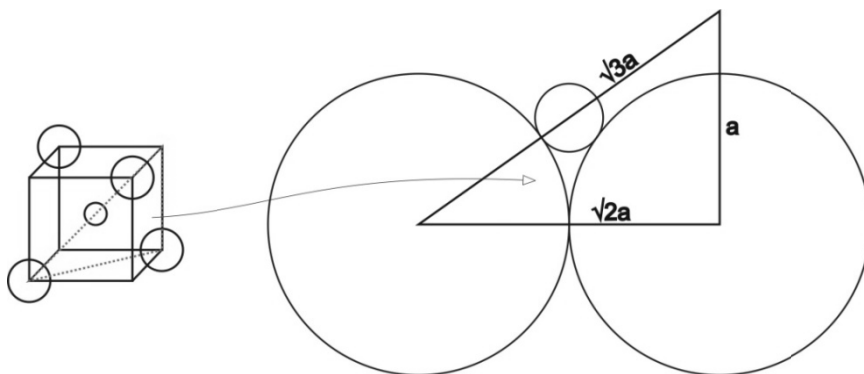
**Figure 3. Geometrical boundary conditions for 3-dimensional particle model
with nanoparticle coordination number 4**

Using these boundary conditions (Figure 3), we can write $a = 2r_m/\sqrt{2}$, by which the body diagonal $b = \sqrt{3}a = \sqrt{6}r_m$. When we also know that body diagonal $b = 2(r_m + r_p)$, we can make a proportion

$$\sqrt{6}r_m = 2(r_m + r_p), \qquad (3)$$

which yields

$$r_p = r_m\left[(\sqrt{6} - 2)/2\right], \qquad (4)$$

when the matrix particle radius is known, second phase particle size can be calculated using equation (4) or by using an approximation

$$r_p = 0.225\,r_m. \qquad (5)$$

Coordination numbers 6 and 8 are also possible but again, with given initial boundary conditions, more infrequent than second phase particles with coordination number 3 and 4. When analysing these models against real microstructures, we have to understand that although the geometrical boundaries for coordination number 3 is presented in two dimensions, in real situation the nanoparticles with coordination number 3 can exist because the geometrical boundary conditions are not valid anymore in their entirety. Also this model gives us only the lower boundary of the obtainable particle size. Size can be increased by deficiencies in the matrix particle packing and matrix particle shapes etc. With current initial boundary conditions this would suggest slightly lower predicted size compared to obtained size.

Experimental Procedure

Particle size information was obtained from Al_2O_3/Ni 2.5 vol. % samples that were synthesized by thermolysis, slip casted and sintered using pulsed electric current sintering (PECS) method [3]. Additionally model was tested with data of Al_2O_3/Ni 2.5 vol. % nanocomposites available from literature [1, 2]. For detailed information about the synthesis and processing, see the marked references.

Data was analysed by comparing the measured matrix and second phase particle sizes to size values predicted by the presented quantitative geometrical model.

Evaluating the quantitative geometrical model

Table 1 summarizes the particle sizes of the sintered Al_2O_3/Ni nanocomposite samples, literature data and nickel grain size predicted by the geometrical model.

Table 1

Matrix particle sizes and nickel nanoparticle sizes of sintered Al_2O_3/Ni nanocomposite samples prepared using thermolysis of nitrate salts with nickel concentration near percolation threshold (~2.5 vol. % [1]). Particle sizes are compared to values predicted by the geometrical model with different coordination numbers (CN)

Reference	Processing method	Sintering method	Al_2O_3 (matrix)	Ni (measured)	Ni (CN 3 – CN 4)
Moya et al. [1]	-	PECS	300 ± 50 nm	< 60 nm	47 – 67 nm
Rodrigues-Suarez et al. [2]	Isostatic pressing	CS	800 ± 200 nm	110 ± 36 nm	123 – 180 nm
Rodrigues-Suarez et al.[2]	-	PECS	250 ± 100 nm	50 ± 18 nm	39 – 56 nm
Kannisto et al. [3]	Slip casting	PECS	660 ± 160 nm	110 ± 37 nm	102 – 149 nm

Coordination number 3 or 4 gives the most accurate prediction for the particle size near the percolation threshold but the lower boundary can be found also with radius ratio $r_p/r_m < 0,155$. All the above samples were synthesized with similar method and by using the same α-alumina powder which has narrow size distribution and homogeneous round morphology that correlates well to the initial boundary conditions of our model.

Thermodynamics of the particle system is the key to understand why the r_p/r_m is predetermined. Thermo-

dynamically the surface energy of the nanoparticles attempt to minimize which is the basic principle for coarsening happening during sintering. Nanocomposite system can have two stages of sintering. First the primary sintering phase which leads to a equilibrium state and grain coarsening slows down or stops because matrix particles need additional energy to swallow the second phase particles and all the second phase particles diffuse approximately at the same rate. Second sintering phase comes when energy is sufficient to overcome the surface energy, in which case the matrix coarsening continues. It is possible that the metal will melt due to the energy needed to initiate the second sintering phase which complicates predicting the outcome in that case. This gives consideration also for the initial matrix particle size which determines the final sintering temperature.

Geometrical model presented here will apply in first sintering phase. This is backed by the microstructures of Al_2O_3/Ni [1-3], ZrO_2/Ni [6] and Al_2O_3/W [9] nanocomposites which show metal nanoparticles located primarily on the grain boundaries and not inside matrix grains in fully dense compacts. This implicates that metal particle coarsening/coalescence is a cause of matrix particle coarsening which is in turn hindered by the second phase particle inclusions. Microstructure analysis also shows that the most probable location for the second phase particle is in triple junctions (tetrahedral sites) with coordination number 4 [1, 3, 9].

Based on studies by Esteban-Betegón et al. [5], in thermolytic synthesis of ceramic/metal nanocomposite powders, the size of the metal salt anion will determine the size of the obtained metal oxide nanoparticles. Also the used salt will affect the clustering of the metal oxide nanoparticles, which will increase the metal nanoparticle coarsening significantly during sintering. In terms, the used salt will give the first lower boundary of metal nanoparticle size during powder synthesis phase. Best dispersion and smallest particle size was obtained by using nitrate salts. As seen in the results of Esteban-Betegón et al., the particles size of nickel after sintering is hugely affected by the clustering behaviour of nanoparticles during synthesis. Model presented here assumes that the nanoparticles are evenly distributed in the matrix and such initial stage was portrait by Rodriguez-Suarez et al. [7] in their qualitative geometrical model for nanocomposite sintering.

Another mechanism that is related to coarsening of nanoparticles is percolation [4, 6]. The percolation theory predicts that beyond certain concentration of metal nanoparticles, they form networks and start to coalescence into larger aggregates during sintering, therefore losing properties they may have had regarding to their original size [6]. Percolation is closely tied to the geometry of the microstructure and it is likely that they are linked together also mathematically. As seen in the qualitative geometrical model of Rodriguez-Suarez et al., the initial concentration of second phase particles will have a great impact on their size after sintering [7]. The connection with our model and percolation can be seen for example in the prediction that the percolation threshold concentration of nickel nanoparticles will be lower when the initial matrix particle size grows larger, which leads to smaller obtainable increase in properties that are related to size of the second phase nanoparticles (e.g. hardness [6]).

To understand what role the coordination numbers play and which of them gives the best estimation of the particle size in different cases, we have to understand the relation between matrix particle size and size distribution, matrix and second phase material and concentration of the second phase particles. Also the roles of sintering kinetics, initial second phase nanoparticle concentration and nanoparticle diffusion rates have to be taken into account.

3. CONCLUSION

Presented quantitative geometrical model consistently predicts final particle size of second phase metallic particles of synthesized Al_2O_3/Ni nanocomposites and data found in literature. A good estimation of the obtained nickel nanoparticle size could be calculated using the model with coordination number 3 or 4, which refers to r_p/r_m ratio of $0.155 - 0.225$. Data that fits in the model indicates that geometry has significant impact on the sintering results and can be used to predict sintering outcome. In future, different material combinations should be tested to confirm the geometrical hypothesis. To make the model more useful, it should take into account the matrix particle size distribution, sintering kinetics and initial concentration and diffusion rates of metal nanoparticles.

References

1. J.S. Moya, T. Rodriques-Suarez, S. Lopez-Esteban, C. Pecharromán, R. Torrecillas, L.A. Días and M. Nygren, Diamond-like hardening of alumina/Ni nanocomposites, Adv. Eng. Mater. 9 (2007) 898-901.

2. T. Rodrigues-Suarez, J.F. Bartolomé, A. Smirnov, S. Lopez-Esteban, R. Torrecillas, J.S. Moya, Sliding wear behaviour of alumina/nickel nanocomposites processed by a conventional sintering route, J. Eur. Ceram. Soc. 31 (2011) 1389-1395.

3. E. Kannisto, E. Cura, E. Levänen, S-P Hannula, Mechanical properties of alumina based nanocomposites, Key engineering materials, Key Engineering Materials 527 (2013) 101-106.

4. J. S. Moya, S. Lopez-Esteban, C. Pecharromán, The challenge of ceramic/metal microcomposites and nanocomposites, Progress in materials science 52, (2007) 1017-1090.

5. F. Esteban-Betegón, S. Lopez-Esteban, J. Requena, C. Pecharromán, J. S. Moya, J. C. Conesa, Obtaining Ni nanoparticles on 3Y-TZP powder from nickel salts, J. Am. Ceram. Soc. 89 (2006) 133-150.

6. C. Pecharromán, F. Esteban-Betegon, J. F. Bartolomé, Gunther Richter and J. S. Moya, Theoretical model of hardening in Zirconia-Nickel Nanoparticle composites, Nano Let. 4 (2004) 747-751.

7. T. Rodriguez-Suarez, J. F. Bartolomé, J. S. Moya, Mechanical and tribological properties of ceramic/metal composites: A review of phenomena spanning from the nanometer to the micrometer length scale, J. Eur. Ceram. Soc. (2012) http://dx.doi.org/10.1016/j.jeurceramsoc.2012.06.026.

8. W.D. Kingery, H.K. Bowen, D.R. Uhlmann, Introduction to ceramics, 2nd edition, Wiley-Interscience, 1976.

9. T. Rodriguez-Suarez, L. A. Díaz, R. Torrecillas, S. Lopez-Esteban, W-H. Tuan, M. Nygren, J. S. Moya, Alumina/tungsten nanocomposites obtained by spark plasma sintering, Composites Science and Technology 69 (2009) 2467-2473.
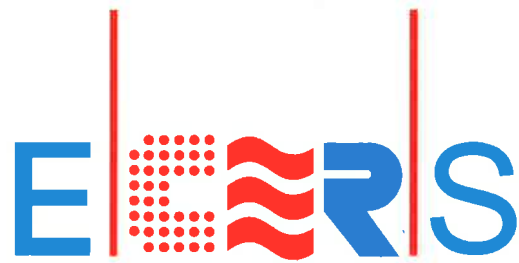
GEORGIA, SVANETHI

Awards

JECS Trust Diploma
2nd prize for best lecture award

European Ceramic Society's 2nd ICSYS conference held on October 2012 in Tbilisi, Georgia.

E|≈R|S

JECS TRUST

DIPLOMA

II

Organizing Committee of

2nd International Conference for Students and Young

Scientists on Materials Processing Science

Tbilisi, Georgia, 10-13 October 2012,

Georgian Technical University

awards

Erkka Kannisto the Second Degree Diploma for the Best Lecture

Geometrical model to evaluate the lower boundary of

nanoparticle size in ceramic/metal nanocomposites produced

by thermolysis

Conference Chairman _____ Z. Kovziridze